

HIGH RESOLUTION IMAGING OF ANISOTROPIC CONDUCTIVITY WITH
MAGNETIC RESONANCE ELECTRICAL IMPEDANCE TOMOGRAPHY
(MR-EIT)

A THESIS SUBMITTED TO
THE GRADUATE SCHOOL OF NATURAL AND APPLIED SCIENCES
OF
MIDDLE EAST TECHNICAL UNIVERSITY

BY

EVREN DEĞİRMENÇİ

IN PARTIAL FULFILLMENT OF THE REQUIREMENTS
FOR
THE DEGREE OF DOCTOR OF PHILOSOPHY
IN
THE DEPARTMENT OF ELECTRICAL AND ELECTRONICS ENGINEERING

APRIL 2010

Approval of the thesis:

**HIGH RESOLUTION IMAGING OF ANISOTROPIC CONDUCTIVITY
WITH MAGNETIC RESONANCE ELECTRICAL IMPEDANCE
TOMOGRAPHY (MR-EIT)**

submitted by **EVREN DEĞİRMENCİ** in partial fulfillment of the requirements for
the degree of **Doctor of Philosophy in Electrical and Electronics Engineering**
Department, Middle East Technical University by,

Prof. Dr. Canan Özgen _____
Dean, Graduate School of **Natural and Applied Sciences**

Prof. Dr. İsmet Erkmen _____
Head of Department, **Electrical and Electronics Engineering Dept.**

Prof. Dr. Murat Eyübođlu _____
Supervisor, **Electrical and Electronics Engineering Dept., METU**

Examining Committee Members:

Prof. Dr. Nevzat G. Gençer _____
Electrical and Electronics Engineering Dept., METU

Prof. Dr. Murat Eyübođlu _____
Electrical and Electronics Engineering Dept., METU

Prof. Dr. Adnan Köksal _____
Elec. and Electro. Engineering Dept., Hacettepe Univ.

Prof. Dr. Mustafa Kuzuođlu _____
Electrical and Electronics Engineering Dept., METU

Assist. Prof. Dr. Yeşim S. Doğrusöz _____
Electrical and Electronics Engineering Dept., METU

Date:

16.04.2010

I hereby declare that all information in this document has been obtained and presented in accordance with academic rules and ethical conduct. I also declare that, as required by these rules and conduct, I have fully cited and referenced all material and results that are not original to this work.

Name, Last name : Evren DEĞİRMENÇİ

Signature :

ABSTRACT

HIGH RESOLUTION CONDUCTIVITY IMAGING OF ANISOTROPIC CONDUCTIVITY WITH MAGNETIC RESONANCE ELECTRICAL IMPEDANCE TOMOGRAPHY (MR-EIT)

Değirmenci, Evren

Ph.D., Department of Electrical and Electronics Engineering

Supervisor : Prof. Dr. Murat Eyüboğlu

April 2010, 152 pages

Electrical conductivity of biological tissues is a distinctive property which differs among tissues. It also varies according to the physiological and pathological state of tissues. Furthermore, in order to solve the bioelectric field problems accurately, electrical conductivity information is essential. Magnetic Resonance Electrical Impedance Tomography (MREIT) technique is proposed to image this information with high spatial resolution. However, almost all MREIT algorithms proposed to date assumes isotropic conductivity in order to simplify the underlying mathematics. But it is known that most of the tissues in human body have anisotropic conductivity values. The aim of this study is to reconstruct anisotropic conductivity images with MREIT. In the study, five novel anisotropic conductivity reconstruction algorithms are developed and implemented. Proposed algorithms are grouped into two: current density based reconstruction algorithms (*Type-I*) and magnetic flux density based algorithms (*Type-II*). Performances of the algorithms

are evaluated in several aspects and compared with each other. The technique is experimentally realized using 0.15T METU – EE MRI System and anisotropic conductivity images of test phantoms are reconstructed using all proposed algorithms.

Keywords: Magnetic resonance, electrical impedance, tomography, anisotropic conductivity, reconstruction, imaging.

ÖZ

MANYETİK REZONANS ELEKTRİKSEL EMPEDANS TOMOGRAFİSİ İLE YÖN BAĞIMLI İLETKENLİĞİN YÜKSEK ÇÖZÜNÜRLÜKLÜ OLARAK GÖRÜNTÜLENMESİ

Değirmenci, Evren

Doktora, Elektrik ve Elektronik Mühendisliği Bölümü

Tez Yöneticisi : Prof. Dr. Murat Eyübođlu

Nisan 2010, 152 sayfa

Dokuların elektriksel iletkenliđi dokular arasında farklılık gösteren ayırıcı bir özelliktir. Bu özellik dokunun fizyolojik ve patolojik durumuna göre de deđişiklik göstermektedir. Ayrıca biyoelektrik alan problemlerinin dođru olarak çözülebilmesi için elektriksel iletkenlik bilgisine ihtiyaç duyulmaktadır. Bu bilgiyi yüksek çözünürlüklü olarak elde edebilmek için Manyetik Rezonans Elektriksel Empedans Tomografisi (MREET) önerilmiştir. Ancak şimdiye kadar önerilen MREET algoritmalarının hemen hepsinde iletkenlik, matematiksel problemi basitleştirmek için yön bağımsız kabul edilmiştir. Fakat insan vücudundaki pek çok dokunun yön bağımlı iletkenliğe sahip olduđu bilinmektedir. Bu çalışmanın amacı MREET tekniđi ile yön bağımlı iletkenlik görüntüleri oluşturmaktır. Çalışmada MREET için beş ayrı yön bağımlı iletkenlik görüntüleme algoritması geliştirilmiş ve uygulanmıştır. Geliştirilen görüntü oluşturma algoritmaları iki grupta toplanmıştır: akım yoğunluğu kullanan algoritmalar (*Tip-I*) ve manyetik akı yoğunluğu kullanan

algoritmalar (*Tip-II*). Geliştirilen algoritmaların performansları pek çok yönden sınanmış ve başarımları karşılaştırılmıştır. Ayrıca teknik 0.15T ODTÜ – EE MRI Sisteminde gerçekleşmiş ve test cisimleri için önerilen tüm algoritmalarla görüntü oluşturulmuştur.

Anahtar Kelimeler: Manyetik rezonans, elektriksel empedans, tomografi, yön bağımlı iletkenlik, geriçatım, görüntüleme.

To My Parents

and

To Filiz

ACKNOWLEDGEMENTS

Firstly, I would like to thank to my family for their continuous support, understanding and patience. They became the endless power of me during all this study.

I wish to express my gratitude to my supervisor Prof. Dr. Murat Eyübođlu for his guidance, advice, criticism, encouragements and insight throughout the research.

I am grateful to my thesis committee members Prof. Dr. Adnan Köksal and Prof. Dr. Mustafa Kuzuođlu for their valuable criticism and suggestions.

I would like to thank to my dear friends Emre Arpinar, Ali Ersöz, Tankut Topal, Ümit Aydın, Alireza Mazloumi, Ceren Bora, Kerim Kara, Soner İlhan Keçeli, Gökhan Eker, Rasim Boyacıođlu, and Murat Önal for their valuable advice and “geyik” chats. I want to specially thank to Emre and Ali for their contributions to this work during endless nights in the MRI laboratory. I collected my experimental data while they were collecting “dota”. I could not finish that process without them. I also wish to thank to Ayhan, Hüseyin, Dario, Murat Özsüt, Mehmet Bayraktar, Feza, Balkar, Berna, Reyhan, Azadeh and Evrim for their support and friendship.

This study is supported by METU Research Grant BAP-08-11-DPT2002K120510 and Turkish Scientific and Technological Research Council (TUBITAK) Research grant 107E141.

Finally, I wish to express my deepest gratitude to my love Filiz for their support and patience during the final which is also most difficult phase of my thesis study. I also would like to thank to Öztürk family for their sincere encouragements.

TABLE OF CONTENTS

ABSTRACT	iv
ÖZ	vi
ACKNOWLEDGEMENTS	ix
TABLE OF CONTENTS	x
CHAPTER	
1. INTRODUCTION.....	1
1.1 Conductivity Imaging.....	1
1.2 Development of MREIT	2
1.3 Objectives of the Thesis	12
1.4 Outline of the Thesis	13
2. THEORY.....	14
2.1 Introduction	14
2.2 The Forward Problem of Anisotropic MR-EIT	14
2.3 Numerical Implementation of the Forward Problem	16
2.3.1 Discretization of Biot-Savart Law	18
2.4 Extraction of Magnetic Flux Density from MR Images	21
2.5 Phase Unwrapping	27
3. EXPERIMENTAL SETUP.....	30
3.1 Introduction	30
3.2 Current Source	30
3.3 Phantom.....	34
4. CURRENT DENSITY BASED RECONSTRUCTION ALGORITHMS...41	
4.1 Introduction	41
4.2 Equipotential Projection Based Anisotropic Conductivity Reconstruction Algorithm	42
4.2.1 Introduction	42
4.2.2 Algorithm	42

4.3 Anisotropic J-Substitution and Anisotropic Hybrid J-Substitution Conductivity Reconstruction Algorithm.....	50
4.3.1 Introduction.....	50
4.3.2 Anisotropic J-Substitution Algorithm.....	51
4.3.3 Anisotropic Hybrid J-Substitution Algorithm.....	55
5. MAGNETIC FLUX DENSITY BASED RECONSTRUCTION ALGORITHMS.....	56
5.1 Introduction.....	56
5.2 Anisotropic Harmonic B_z Conductivity Reconstruction Algorithm	56
5.2.1 Introduction.....	56
5.2.2 Algorithm.....	57
5.3 Anisotropic Sensitivity Conductivity Reconstruction Algorithm.....	60
5.3.1 Introduction.....	60
5.3.2 Algorithm.....	61
6. RESULTS AND COMPARISONS	63
6.1 Introduction.....	63
6.2 Conductivity Models.....	63
6.2.1 Computer Model 1	65
6.2.2 Computer Model 2	66
6.2.3 Computer Model 3	67
6.2.4 Computer Model 4	68
6.3 Error Calculation.....	69
6.4 Simulation of Measurement Noise.....	70
6.5 Results of the Proposed Algorithms.....	71
6.5.1 Results for Computer Model 1	71
6.5.2 Results for Computer Model 2.....	88
6.5.3 Results for Computer Model 3.....	94
6.5.4 Results for Computer Model 4.....	100
6.5.5 Results for Experimental Models.....	108
6.6 Final Comparisons	122
7. DISCUSSIONS AND CONCLUSIONS	124
7.1 Summary of the Thesis Work	124

7.2 Conclusions	125
REFERENCES.....	128
APPENDIX	
A. EXTENSION OF THE TECHNIQUE PROPOSED BY IDER <i>ET AL</i> FOR THE RECONSTRUCTION OF ANISOTROPIC CONDUCTIVITY	132
A.1 Algorithm	132
A.1.1 Derivation Using Sobel Operator.....	138
A.1.2 Derivation Using FFT Algorithm Based Differentiation	140
A.1.3 Derivation Using Forward Difference Based Differentiation....	142
A.1.4 Derivation Using Forward Difference Based Differentiation with Up-sampling	144
VITA	150

CHAPTER 1

INTRODUCTION

1.1 Conductivity Imaging

Electrical conductivity is one of the distinctive features of biological tissues and this makes the imaging of tissue conductivity values possible [1]. Furthermore this value varies with physiological activity of the tissue and imaging tissue conductivity gives information about physiological activities and pathologies [2]. Accurate solution of bioelectric field problems also requires correct knowledge of tissue conductivity values [3], [4]. Electrical Impedance Tomography (EIT) has been proposed to reconstruct electrical conductivity distribution inside a volume conductor non-invasively. The technique is based on generating a current distribution inside the conductor either by injecting or by inducing current and performing electrical or magnetic measurements that reflect the internal conductivity distribution [1]. According to the current excitation strategy, the technique can be classified as injected EIT or induced EIT. In injected EIT systems, current is applied via the electrodes placed on the boundary, and potential generated by this current is recorded using again the surface electrodes [5], while in induced EIT, current distribution is induced via an excitation coil using time varying fields [6]. Induced current will generate a magnetic field reflecting the internal conductivity distribution. This magnetic field is measured via sensors to solve the inverse problem of finding conductivity. This methodology is also proposed for sub-surface imaging.

The main limitations on conventional EIT systems are the resolution and the sensitivity. The sensitivity of peripheral measurements to conductivity perturbations in different regions is different. Specifically, conductivity perturbations in the inner parts of the imaging regions do not alter the boundary voltage measurements as much as the perturbations close to the boundary. Moreover, the spatial resolution of resistivity image is primarily determined by the number of electrodes used in the EIT system. Since the number of electrodes that can be placed on the boundary is limited and the sensitivity of surface electrodes to inner regions is small, reconstructed conductivity images have low and space dependent spatial resolution.

In order to eliminate the problem of non-uniform sensitivity, the data set must include measurements that are equally dependent on conductivity changes in different regions of the imaging region. If the data set includes measurements made directly from the inner regions, uniform sensitivity distribution can be achieved. Voltage measurements cannot be obtained from inner regions non-invasively. However, it is possible to measure magnetic flux density distribution throughout the imaging region generated by the externally applied current using Magnetic resonance Imaging (MRI) techniques [7], [8]. Using these magnetic flux density measurements, calculation of current density distribution in the imaging region is also possible and this technique is named as Magnetic Resonance Current Density Imaging (MR-CDI) [7]. Current density measurements using MR-CDI technique or magnetic flux density measurements can be combined with peripheral voltage measurements of EIT to reconstruct absolute conductivity images with uniform sensitivity and high resolution. This technique is called as Magnetic Resonance Electrical Impedance Tomography (MR-EIT).

1.2 Development of MREIT

The main milestone in the development of MR-EIT is the emergence of MR-CDI technique. Therefore explaining briefly the important aspects of this technique and giving the development of it will be helpful to understand the basics of MR-EIT.

At the beginning of 1990's, a new imaging modality proposed to reconstruct images of current density generated by injected or induced currents using magnetic flux density measurements [7]. This technique is briefly named as current density imaging (CDI). CDI can be classified in 3 main categories as DC-CDI, RF-CDI and AC-CDI with respect to frequency of the injected current.

First CDI images were reported by Scott *et al* in 1991 [7]. In this study, current was applied to a conductor object in synchrony with the pulse sequence used for imaging and distribution of this current inside the object was imaged. Although, injected current was not exactly a DC current, since the frequency of it was low with respect to the other injected currents, this technique is named as DC-CDI. In order to obtain the current density distribution in DC-CDI, it is necessary to rotate the object in the magnet. This is because, for the calculation of current density distribution, the components of magnetic flux density in all three dimensions are needed but only the component in the same direction with the main magnetic field can be measured. In a later study, the same group proposed to reconstruct RF-CDI images in homogeneous medium using RF currents [8]. In this study, they stated that interleaved multi-slice pulse sequence can not be used in RF-CDI. In RF-CDI, it is not necessary to rotate the object. Radio frequency needed to use in this technique is equal to the Larmor frequency of the MR system used. Although, RF-CDI is advantageous when compared with the DC-CDI since it does not require rotation of the object, it would be difficult to realize circuits needed to use at radio frequency. Electromagnetic considerations for RF-CDI and the usage of RF-CDI in heterogeneous media were investigated in [9].

Measurement of magnetic fields generated by non-uniform AC current density using magnetic resonance was proposed by Ider and Müftüler [10], [11]. In this study, currents having AC frequencies at 100-200 kHz were passed through the wires placed outside the object and AC magnetic fields inside the object generated by these currents were measured. Measurement of only one component of magnetic flux density is sufficient also in this technique.

Misplacement of current carrying wires during CDI experiments causes distortion in the reconstructed image. This topic was examined by Gamba and Depty [12] and they concluded that, in order to decrease the distortion, current carrying wires must be placed carefully that they do not produce magnetic field component in the direction of the main magnetic field. There are also publications about possible clinical applications of CDI in the literature [13], [14], [15]. In [13], Sersa *et al* investigated the current density imaging of mouse tumor. This work helped to determine the effects of electrode geometry on the electro-chemotherapy. The success of electro-chemotherapy depends substantially on the amplitude and spatial distribution of the current density that passes through inside and around the tumor. Therefore, imaging of this current density distribution affects the success of chemotherapy directly. Beravs *et al* used CDI for obtaining the spatial distribution of DC electric current in the bone [14]. They made experiments on osteoporosis patients which have very low calcium content in their bones, compared the conductivity of their bones with the healthy ones and showed that CDI can be used in the diagnosis of osteoporosis. In 1999, Joy *et al* made a study on determining the current density and current pathways on a rabbit brain during trans-cranial electro stimulation [15].

Bodurka *et al* carried out experiments on a 3T MRI system for current induced magnetic resonance phase imaging [16]. In contrast to previous studies, no external current is applied and magnetic field changes due to neuronal activity are measured. It is reported that magnetic field changes of $1.7 \pm 0.3 \text{ nT}$ were detectable due to electric current as small as $10 \mu\text{A}$.

In 2001, an alternative method for measuring AC flux density and current density is proposed by Mikac *et al* [17]. In his study 1kHz AC currents as low as 350 A/m^2 are imaged using a 2.35T system.

The idea of using current density distribution measurements of CDI and boundary voltage measurements of EIT in order to obtain the conductivity map inside an object was first proposed by Zhang [18]. In this technique, potential difference

between surface points ($\Delta\phi$), current density (J) and unknown conductivity (σ) are related by the following integral equation:

$$\Delta\phi = \int_l \vec{E} \cdot d\vec{l} = \int_l \left(\frac{1}{\sigma}\right) \vec{J} \cdot d\vec{l} \quad (1.1)$$

where l is any integral path in the tomographic plane which connects two surface measurement points having a potential difference of $\Delta\phi$. If the imaging region is divided into M pixels, all having constant conductivity, and the above equation is reduced to an equation system for N measurement, the following matrix equation is obtained:

$$\Delta\phi = \mathbf{G}\rho + \mathbf{n} \quad (1.2)$$

where $\Delta\phi$ and \mathbf{n} are $N \times 1$ measurement and noise vectors, respectively, ρ is $M \times 1$ vector of unknown pixel conductivity values and \mathbf{G} is $N \times M$ projection matrix which depends on inside current density information and chosen integral path. Unknown conductivity values can be found from this matrix equation.

In 1994, Woo *et al* proposed a new technique which constitutes electrical conductivity image using current density distribution obtained from CDI technique [19]. In this study, the difference between the current density distribution measured from a real object and the calculated current density distribution using finite element method for a computer simulation model was minimized. But the technique has low spatial resolution and poor convergence characteristics since, it can not use inside current density information effectively. Also in the reconstructed images, it was seen that error is high especially at the regions where current density changes rapidly.

In 1995, Birgül and Ider proposed a new technique to find conductivity [20]. In this technique, it is stated that when the conductivity inside an object changes, current density will change and there will be a change in the magnetic field. Therefore, if

this change in the magnetic field could be measured, then the inverse problem that finds the conductivity distribution will be formed and solved. Also, since the change in the magnetic field can be measured with equal sensitivity in the imaging region, conductivity map will be obtained with a uniform spatial distribution. The same group published a paper including a two dimensional version of this technique [21]. In [21], it is stated that currents in a two dimensional object will produce three dimensional magnetic fields but, these magnetic fields will have only normal component on the boundary of the object. A linear relation between the conductivity change and change in the normal component (taken as z direction in the study) of magnetic field could be constituted with the following equation:

$$\Delta \mathbf{b} = \mathbf{S} \Delta \sigma \quad (1.3)$$

Here, $\Delta \mathbf{b}$ is the change in the magnetic flux density, $\Delta \sigma$ is the change around the first assumed conductivity value and \mathbf{S} is the sensitivity matrix. Behavior of the sensitivity matrix is analyzed using singular value decomposition in the study. Sensitivity matrix is just calculated for the first conductivity distribution. After obtaining the sensitivity matrix, since $\Delta \mathbf{b}$ is known, required conductivity change values can be calculated from

$$\Delta \sigma = \mathbf{S}^{-1} \Delta \mathbf{b} \quad (1.4)$$

Here, \mathbf{S} matrix doesn't have to be square and is generally singular, so its inverse can not be taken directly. In the study, generalized matrix inverse was used. In this technique, only the component of magnetic flux density in the direction of MR system's main magnetic field was used. Therefore, the need for rotating the object as in the techniques which use current density distribution is eliminated. In the study, experimental magnetic field measurements were also used. Conductivity image was obtained with high resolution. But the important point here is, using only the magnetic flux density measurements, a unique conductivity distribution couldn't be reconstructed using only the magnetic flux density measurements. But in 2003, Birgül *et al* was proposed a technique which uses magnetic flux density and surface

potential measurements together to obtain the true conductivity distribution [22]. In this technique, magnetic flux density measurements were used first to obtain a detailed conductivity map and then this conductivity map was scaled to satisfy the potential measurements.

Eyüboğlu *et al* proposed another algorithm which uses current density distribution and surface potential measurements to image the conductivity and patented this technique [23]. Technique is based on the fact that current lines and equipotential lines are perpendicular to each other. Using this fact, surface potentials are projected inside the object through the lines which are perpendicular to the current lines. Therefore, every pixel in the object is assigned a potential value and inside potential distribution and potential gradient is obtained. Then, since the current density in measured conductivity distribution is calculated from the following formula:

$$\sigma(x, y) = \frac{|J(x, y)|}{|\nabla\phi(x, y)|} \quad (x, y) \in S \quad (1.5)$$

Here, J is the current density, $\nabla\phi$ is the gradient of the potential field and S is the imaging region [23], [24]. Simulation and experimental results obtained using this technique is given in [25]. This technique can reconstruct true conductivity images with high and position independent spatial resolution. Also, one current injection pattern is enough for reconstruction of the conductivity map. Kwon *et al* developed a similar technique that uses equipotential lines [26] showed that conductivity image, reconstructed with a measurement which satisfies Dirichlet boundary conditions, is unique. But only the simulation results were given in this study.

In 2002, Kwon *et al* proposed an alternative absolute conductivity reconstruction algorithm named J-substitution algorithm [27] and gave the simulation results. In the proposed iterative algorithm, Kwon *et al* minimized the following function:

$$\Phi(\rho) := \int_{\Omega_s} \left| J(r) - \frac{1}{\rho(r)} E_\rho \right|^2 dr \quad (1.6)$$

Here, J is magnitude of the current density, E_ρ is magnitude of the electric field strength calculated from Poisson equation which is solved for a given conductivity distribution ρ with Neumann boundary conditions. This minimization was resulted with an update equation:

$$\rho^{k+1} = \frac{E^k}{J} \quad (1.7)$$

Finite element method is used for the solution of the boundary value problem in the study. Since ρ and $\alpha\rho$ would satisfy the same current density distribution, true resistivity value is calculated updating the resistivity using the potential measurements as given in the following equation:

$$\rho^{k+1} = \frac{E^k V}{J V^k} \quad (1.8)$$

In this study, it is stated also that, if at least two current injection pattern satisfying $|\mathbf{J}^1 \times \mathbf{J}^2| \neq 0$ equality is used with one potential measurement, then absolute conductivity can be reconstructed. In a later study, this technique is examined experimentally using a homogeneous phantom and a phantom having an insulator object by Khang [28]. But in this study, although there was no error definition, various numerical error values were given. A similar experimental study using J-substitution algorithm was made by Lee *et al* [29]. In this study, a sausage was placed in the phantom and current density is not zero anywhere was satisfied. Also, with imaging the grid phantom with a spatial distribution of 256×256 instead of 128×128 and using a more effective phase unwrapping algorithm, they obtained more accurate results than [26]. In a recent study, Boyacıoğlu and Eyüboğlu combined the J-substitution algorithm and equipotential projection algorithm in [31]

and proposed a new reconstruction algorithm [30]. This technique reconstructs conductivity using equipotential line method first, and then this conductivity is given to the J-substitution algorithm as an initial distribution. Reconstruction accuracy is higher than both techniques. This technique contains the positive parts of the both techniques.

Another technique, which obtains conductivity image by using just the component of magnetic flux density in the direction of main magnetic field without requiring the rotation of the object, was proposed by Seo *et al* [31]. Although, this technique does not require the rotation of the object which is impractical, it is based on the calculation of $\nabla^2 B_z$. This means the differentiation of noisy B_z measurements twice. Furthermore, proposed image reconstruction algorithm finds conductivity σ from its spatial gradient $\nabla\sigma$ using line integrals and both line integrals and numerical derivation tend to increase the error. Therefore, in the study, only the results obtained from simulations with small additive error added were published. Later, this study was improved by Oh *et al* using various techniques [32] and named as Harmonic B_z algorithm. In this study, firstly, in order to suppress the measurement noise in B_z better, current injection process was repeated N times. Also, current injected from recessed electrodes in order to prevent distortions especially near the current injection electrodes. Only the simulations results were given in this study, too. Phantom experiments about these studies were given in [33]. The last technique related with these studies was proposed by Park *et al* [34]. The new technique in this study takes the derivative of B_z once different from the Harmonic B_z algorithm. Therefore, it has slightly improved the noise tolerance. Realistic errors added simulation results were given in the study. In 2005, Oh *et al* published the reconstruction results of biological tissue phantoms using Harmonic B_z algorithm in MREIT [35]. Bovine tongue and liver, porcine muscle and chicken breast were used as biological tissues and conductive agar gelatin as background medium in the study. Conductivity values were reconstructed with errors of %5 - %25. Although the same group reported increased noise tolerances in [38] and [39], their usage of Harmonic B_z algorithm in this study was quite interesting.

In 2003, Ider *et al* developed three new reconstruction algorithms for MR-EIT [36]. All the algorithms in this study were derived from $\nabla \times \rho J = 0$ equality which is valid in the object. The problem of reconstruction is treated as a hyperbolic system of first order differential equations and three numerical methods named “method of characteristics”, “reconstruction by integration along Cartesian grid lines” and “reconstruction formulated as a linear set of equations using finite differences” are used. In the study, firstly, “if only current density measurements were used, what will be reconstructed?” problem was investigated and it is found that, under definite conditions current density measurements can reconstruct true conductivity image except a scaling. Then it was shown that, for applications where absolute conductivity values are needed, only one potential measurement is enough for the completeness of the image. All three methods proposed in this study is three dimensional and they can easily be adapted to the two dimensional imaging. Also, methods are not iterative and it was proven that reconstructed images are unique. Later, the same group proposed another algorithm which reconstructs conductivity using the component of magnetic flux density in the direction of the main magnetic field [37]. In this new method, the imaging problem is formulated as the solution of a non-linear matrix equation and it is solved iteratively to reconstruct resistivity. Only the numerical simulations were used to test the algorithm but both noise free and noisy simulations used in the study.

Lee *et al* proposed a study that demonstrates a basic setup for breast conductivity imaging [38]. In this study, they introduced the basic imaging setup of the breast MREIT technique with an investigation of four different imaging configurations of current injection electrode positions and pathways using computer simulation studies. Also they performed an experimental study with a breast phantom on a 3.0T MREIT system. Harmonic B_z algorithm was used to reconstruct conductivity images. 15 mA current was applied to ensure the sufficient SNR but it was also pointed out that this current level is beyond the human safety limit. In a similar study, Sadlier *et al* reconstructed biological tissue conductivities with MREIT at 11T MR System in order to decrease current level [39]. They gave the experimental

results and also described technical difficulties encountered in using high field MREIT systems and possible solutions.

In 2007, Kim *et al* reconstructed the conductivity image of a postmortem canine brain [40]. They used 40 mA applied current and Harmonic B_z algorithm for reconstruction. Obtained results showed a clear contrast between gray and white matter. Also in this study, authors proposed a new description as ‘equivalent isotropic conductivity’. They used this term to interpret anisotropic conductivity value of white matter since it is known that white matter has anisotropic conductivity distribution but reconstruction algorithm used is for isotropic conductivity reconstruction. Later, again Kim *et al* reconstructed the conductivity image of canine brain but in this case *in-vivo* [41]. They applied 5 mA current to the living canines first and then they repeated the experiment with the same but postmortem animals with 40 mA applied current. They reported the differences between living and postmortem brain conductivities.

All reconstruction algorithms explained up to here assume conductivity as isotropic and formulates the underlying mathematics according to this assumption. But it is known that most biological tissues have anisotropic conductivity values [42]. Therefore it is clear that this assumption will decrease the accuracy of the reconstruction and application area of the technique. The first algorithm which does not assume isotropic conductivity is proposed by Seo *et al* at 2004 [43]. In the study, $\overline{\sigma}$ conductivity tensor was used to show the anisotropic conductivity. This tensor was selected as a 3×3, positive definite matrix to have a physical meaning. Therefore, this means that, instead of trying with one unknown as in the isotropic case, it is necessary to deal with 6 unknowns of $\overline{\sigma}$. After defining the problem with this tensor, conductivity is updated iteratively starting from the isotropic value found using the Harmonic B_z algorithm for the same boundary conditions. All 6 unknowns of $\overline{\sigma}$ are found in every iteration. Update continues until a stopping criterion is satisfied. The proposed technique was examined with two dimensional simulations, 100 mA applied current and for noisy cases, SNR levels of 300, 200

and 150. It is shown that anisotropic conductivity tensor can be reconstructed if enough current is applied. But since the current has to be kept under a definite value for human and animal experiments, it is concluded that more studies on the reduction of applied currents must be done. Later in 2007, Değirmenci and Eyüboğlu proposed the second technique for anisotropic conductivity reconstruction [44]. This technique depends up on the construction of equipotential lines. Equipotential lines and current lines are perpendicular to each other when the conductivity is isotropic but it is not the case when the conductivity is anisotropic. Therefore, there is a nonlinear relation between anisotropic conductivity distribution and current lines. Technique solves this nonlinear problem iteratively. Numerical simulations for a two dimensional simulation phantom, 20 mA applied current and for noisy cases, SNR levels of 30, 20 and 13 were used to test the proposed algorithm. Later, the same group proposed two more algorithms for anisotropic conductivity reconstruction called anisotropic J-substitution and anisotropic hybrid J-substitution algorithms [45]. These techniques are also iterative and tested with simulation models. Details of these techniques ([49], [50]) will be given in this thesis.

1.3 Objectives of the Thesis

The importance of imaging conductivity distribution in the human body is stated in the previous sections. Therefore, reconstruction of conductivity distribution is one of the most important study areas of biomedical engineering. Several techniques exist for this purpose. MREIT is one of them.

Reconstruction algorithms developed for MREIT technique were given in the previous section. Most of these algorithms are formulated for the reconstruction of isotropic conductivity. But it is known that most of the biological tissues in the human body contain anisotropic conductivity values [42]. Therefore, developing reconstruction algorithms for anisotropic conductivity distribution is a very important study in this field. The main research topic of this thesis is selected according to this and the following objectives were defined:

- To develop and implement different novel reconstruction algorithms for MREIT for the anisotropic conductivity distribution,
- To explore the theoretical limits, contrast and spatial resolution properties of the proposed algorithms,
- To compare all of the novel algorithms using standard data sets,
- To obtain magnetic flux density data using 0.15T METU-EE MRI System,
- To reconstruct conductivity images using this experimental data.

1.4 Outline of the Thesis

In Chapter 2, the forward problem definition of anisotropic MREIT technique is given first. Method for extraction of magnetic flux density data from MRI phase images, phase unwrapping algorithm for the correction of MR phase images and calculation of current density distribution from magnetic flux density data are also explained. Chapter 3 explains experimental studies realized during this thesis study. In Chapter 4, current density based anisotropic conductivity reconstruction algorithms, namely equipotential projection based anisotropic conductivity reconstruction algorithm, anisotropic J-substitution and anisotropic hybrid algorithms are explained. Chapter 4 covers the magnetic flux density based anisotropic conductivity reconstruction algorithms. These algorithms are anisotropic Harmonic B_z and Sensitivity algorithms. Chapter 6 explains the computer models used in simulations and simulation test results of the algorithms. Experimental results are also given in that chapter. Chapter 7 concludes the thesis with a summary, final conclusions and future work.

CHAPTER 2

THEORY

2.1 Introduction

In this chapter, forward problem of anisotropic MR-EIT is formulated first (Section 2.2). Once the potential distribution is calculated with the solution of the forward problem, the magnetic flux density distribution can be calculated using Biot-Savart law. Section 2.3 explains the numerical implementation of the forward problem and discretization of the Biot-Savart law for the calculation of magnetic flux density from injected currents. In practice, the magnetic flux density distribution induced by injected currents is the only thing that can be measured using an MRI system. In Section 2.4, the procedure to extract it from MRI data is explained. Also, the concept of phase unwrapping and the phase unwrapping algorithm used in this study are defined in the final section.

2.2 The Forward Problem of Anisotropic MR-EIT

The forward problem for anisotropic MREIT imaging modality is defined as the calculation of magnetic flux density distribution and peripheral surface potential values for a known anisotropic conductivity distribution and boundary conditions. Forward problem solution is used mainly for the generation of the simulation data. It is also used in the formulation of some reconstruction algorithms. The nonlinear relation between potential field and anisotropic conductivity is defined by Poisson's equation as:

$$\nabla \cdot (\overline{\sigma} \nabla \phi)(x, y) = 0 \quad (x, y) \in S. \quad (2.1)$$

where $\overline{\sigma}(x, y)$ is the anisotropic electrical conductivity which is defined as

$$\overline{\sigma} = \begin{bmatrix} \sigma_{xx} & \sigma_{xy} \\ \sigma_{yx} & \sigma_{yy} \end{bmatrix} \text{ for two dimensional case, } \phi \text{ is the electrical potential and } S \text{ is the}$$

imaging slice. Here $\overline{\sigma}$ is defined as $\begin{bmatrix} \sigma_{xx} & \sigma_{xy} & \sigma_{xz} \\ \sigma_{yx} & \sigma_{yy} & \sigma_{yz} \\ \sigma_{zx} & \sigma_{zy} & \sigma_{zz} \end{bmatrix}$ for three dimensional case

and it is a positive definite symmetric matrix. Equation (2.1) is combined with the following Neumann boundary condition to form a boundary value problem (BVP) of MREIT.

$$-\overline{\sigma} \frac{\partial \phi}{\partial n} = \begin{cases} \overline{J} & \text{on positive current electrode} \\ -\overline{J} & \text{on negative current electrode.} \\ 0 & \text{elsewhere} \end{cases} \quad (2.2)$$

Once the potential field distribution is obtained, the electric field distribution is calculated as:

$$\overline{E} = -\nabla \phi \quad (2.3)$$

and the corresponding current density distribution is calculated via Ohm's law as:

$$\overline{J} = \overline{\sigma} \overline{E} = - \begin{bmatrix} \sigma_{xx} & \sigma_{xy} \\ \sigma_{yx} & \sigma_{yy} \end{bmatrix} \cdot \begin{bmatrix} \nabla \phi_x \\ \nabla \phi_y \end{bmatrix}. \quad (2.4)$$

Magnetic flux density distribution both on imaging plane and at some off-slice points may be required for some reconstruction algorithms. Magnetic flux density generated by the current density distribution found in equation (2.4) is given by Biot-Savart relation as:

$$\vec{B}(x, y, z) = \frac{\mu_0}{4\pi} \int \frac{\vec{J}(x, y) dS \times \hat{a}_R}{R^2}. \quad (2.5)$$

where μ_0 is the permeability of the free space, \vec{R} is the vector from source point (x', y', z') to the field point (x, y, z) and \hat{a}_R is the unit vector in that direction.

2.3 Numerical Implementation of the Forward Problem

For complex conductivity distributions, analytical solutions to the *BVP* expressed in equations (2.1) and (2.2) do not exist in general. Therefore, numerical methods are utilized to solve this kind of *BVP*'s. There are several numerical methods in literature such as finite element method (FEM), finite difference method (FDM), etc. In this study, FEM is used to solve potential field distribution for a given conductivity distribution and boundary conditions. In this technique, instead of finding the analytical expression for the potential field at all points, the value of the potential field at discrete points is calculated. These discrete points are named as nodes. The imaging region is then divided into smaller regions by connecting the nodes in a systematic manner to form the finite elements. Finite elements can be triangular or tetrahedral. The obtained mesh from node and element structure is called as the finite element mesh. In this study, triangular elements are used the finite element mesh and the nodes are at the vertices of the elements. Since the simulation models and the experimental phantom are square, the mesh structure is prepared for a square imaging regions. It contains 3281 nodes and 6400 elements. Employed mesh is given in Figure 2.1.

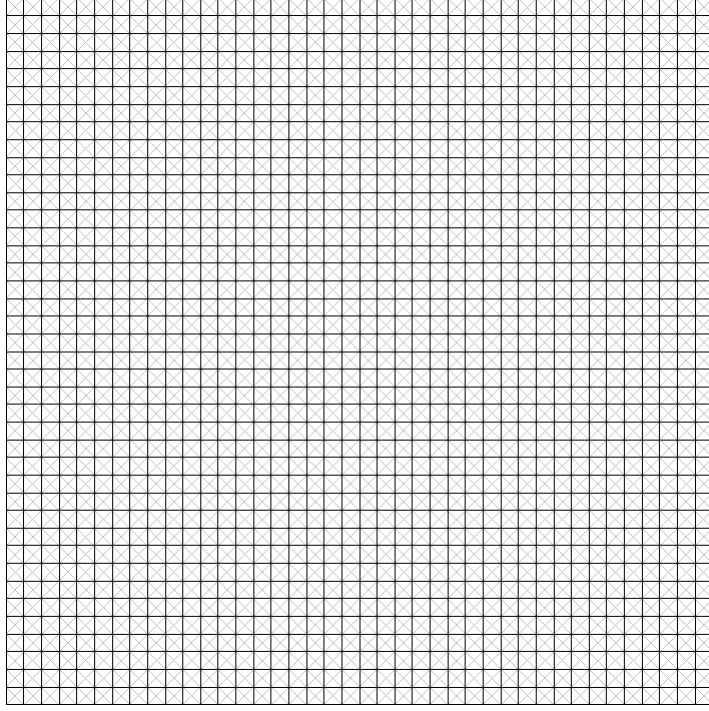


Figure 2.1: Finite element mesh used in the thesis study with 3281 nodes and 6400 elements.

The conductivity is assumed to be constant and the potential field is assumed linearly varying in each finite element. The potential field inside each element is expressed in terms of node potential values and spatial coordinates to form a linear equation. Combining the linear equations for each element, the boundary value problem is converted to a matrix equation of the form

$$\mathbf{A}\phi = \mathbf{b} \quad (2.6)$$

where, \mathbf{A} is the coefficient matrix which depends on the mesh structure and anisotropic conductivity, ϕ is the vector of unknown node potentials and \mathbf{b} is the boundary condition vector. The node potentials are then calculated by matrix inversion and multiplication as

$$\phi = \mathbf{A}^{-1}\mathbf{b}. \quad (2.7)$$

It is important to note that, the square \mathbf{A} must be nonsingular to be invertible. Since only current values at some nodes or elements are specified for a Neumann type *BVP*, there might be more than one field solution to Equation (2.1) which satisfies the boundary condition in Equation (2.2). In this case, the resulting \mathbf{A} matrix is singular. In order to solve this singularity problem and find a field solution, a potential reference must be specified. Numerically it is implemented by selecting a node for reference point and forcing this reference node potential to zero in the matrix equation. This operation guaranties the invertibility of the coefficient matrix.

After calculating the node potentials, electric field and current density in each element are calculated using Equation (2.3) and Equation (2.4), respectively. Next step is the calculation of the magnetic flux density distribution via Biot-Savart relation using calculated currents. Discretization of Biot-Savart relation is explained in the following part.

2.3.1 Discretization of Biot-Savart Law

Since the relation between current density and magnetic flux density is linear, a discretization will be sufficient [46]. In this section, a matrix relation between current and magnetic flux density is derived.

Biot-Savart relation can be rewritten as

$$d\vec{B} = \frac{\mu_0 I}{4\pi} \left(\frac{d\vec{l}' \times \vec{R}}{R^3} \right) \quad (2.8)$$

for a differential current element $I d\vec{l}'$ where I is the current in one finite element and $d\vec{l}'$ is the direction of the current. In this formulation, primed variables are used to indicate the source related variables. The current density vector calculated in the previous part is placed at the center of each element and weighted with the area of the corresponding element. The differential current element can be written as

$$Id\vec{l}' = A(\hat{a}_x J_x + \hat{a}_y J_y + \hat{a}_z J_z). \quad (2.9)$$

Although the equation (2.9) can be reduced for two dimensional case, matrix equations is derived for the general case and simplified when necessary. The vector between the source and the field points, which is \vec{R} , can be written as

$$\vec{R} = (x - x')\hat{a}_x + (y - y')\hat{a}_y + (z - z')\hat{a}_z. \quad (2.10)$$

Evaluating the cross product in equation (2.8), the orthogonal components of magnetic flux density can be written as

$$dB_x = \frac{\mu_0 A}{4\pi} \frac{(z - z')}{[(x - x') + (y - y') + (z - z')]^{3/2}} J_y - \frac{\mu_0 A}{4\pi} \frac{(y - y')}{[(x - x') + (y - y') + (z - z')]^{3/2}} J_z, \quad (2.11)$$

$$dB_y = \frac{\mu_0 A}{4\pi} \frac{(x - x')}{[(x - x') + (y - y') + (z - z')]^{3/2}} J_z - \frac{\mu_0 A}{4\pi} \frac{(z - z')}{[(x - x') + (y - y') + (z - z')]^{3/2}} J_x, \quad (2.12)$$

$$dB_z = \frac{\mu_0 A}{4\pi} \frac{(y - y')}{[(x - x') + (y - y') + (z - z')]^{3/2}} J_x - \frac{\mu_0 A}{4\pi} \frac{(x - x')}{[(x - x') + (y - y') + (z - z')]^{3/2}} J_y. \quad (2.13)$$

Here, it is important to note that, effect of each current element on itself is neglected in order to handle singularity in evaluation of the above integral. To explain more clearly, consider a circular region on x - y plane and assume that uniform current flows in x - y direction. For this configuration, the magnetic flux density at the center of the circle will be zero. For our case, effect of each element on itself is neglected although triangular elements are used.

Equations (2.11), (2.12) and (2.13) are written for n source points and k field points, therefore $3k$ linear equations are formed. These $3k$ equations can be written in matrix form as

$$\begin{bmatrix} b_{x1} \\ \vdots \\ b_{xk} \\ b_{y1} \\ \vdots \\ b_{yk} \\ b_{z1} \\ \vdots \\ b_{zk} \end{bmatrix}_{3k \times 1} = \begin{bmatrix} d_{1,1} & \cdots & d_{1,3n} \\ \vdots & \ddots & \vdots \\ d_{3k,1} & \cdots & a_{3k,3n} \end{bmatrix}_{3k \times 3n} \cdot \begin{bmatrix} j_{x1} \\ \vdots \\ j_{xn} \\ j_{y1} \\ \vdots \\ j_{yn} \\ j_{z1} \\ \vdots \\ j_{zn} \end{bmatrix}_{3n \times 1} \quad (2.14)$$

where the coefficient matrix depends only on the source and field coordinates and therefore constant for a given mesh structure. The coefficient matrix can be divided into parts as

$$\begin{bmatrix} b_x \\ b_y \\ b_z \end{bmatrix} = \begin{bmatrix} 0 & D_z & -D_y \\ -D_z & 0 & D_x \\ D_y & -D_x & 0 \end{bmatrix} \cdot \begin{bmatrix} j_x \\ j_y \\ j_z \end{bmatrix}. \quad (2.15)$$

Here D_x, D_y and D_z are the matrices which depend on the magnitude of the \bar{R} vector and the difference between x, y and z components of field and source points, respectively. Since these matrices are constant for a mesh structure, they can be calculated once and stored. This increases the solution speed of the field problem significantly.

For two dimensional case, j_z is equal to zero and the matrix equation reduces to

$$\begin{bmatrix} \mathbf{b}_x \\ \mathbf{b}_y \\ \mathbf{b}_z \end{bmatrix} = \begin{bmatrix} 0 & \mathbf{D}_z \\ -\mathbf{D}_z & 0 \\ \mathbf{D}_y & -\mathbf{D}_x \end{bmatrix} \cdot \begin{bmatrix} \mathbf{j}_x \\ \mathbf{j}_y \end{bmatrix}. \quad (2.16)$$

2.4 Extraction of Magnetic Flux Density from MR Images

The magnetic flux density distribution generated by the currents inside a conductive object can be measured magnetic resonance imaging techniques. In obtaining these distributions, MR images are taken using appropriate pulse sequences and magnetic flux density distributions are extracted from these measurements. However, only the component of the magnetic flux density in the direction of the main magnetic field of the MR system can be measured using MRI technique. Therefore, the object must be rotated and the experiment must be repeated for three different orientations if the magnetic flux densities in three dimensions are required. Placements of the object in the magnet at these three orientations are given in Figure 2.2. In this figure, (x,y,z) is the coordinate system for the object and (x',y',z') is the coordinate system for the MR system. The main magnetic field of the MR system is in the direction of z' . Figure 2.2(a) shows the orientation of the object inside the magnet for the measurement of B_z , similarly Figure 2.2 (b) and (c) shows the orientations for B_x and B_y measurements, respectively.

When a noise free MRI data without spin relaxation is assumed and the geometric distortions are neglected, the acquired MRI signal using a spin echo pulse sequence shown in Figure 2.3 (without current pulse) can be expressed as

$$S(k_x, k_y, t) = \int \int_{x y} M(x, y) e^{\{j[\gamma B(x, y)t + \theta_c + k_x x + k_y y]\}} dx dy. \quad (2.17)$$

Here, $M(x, y)$ is the continuous real transverse magnetization, $B(x, y)$ is the inhomogeneity component of the magnetic field and θ_c is a constant phase due to instrumentation and receiver circuits. k_x is equal to $\gamma G_x t$ and k_y is equal to $\gamma G_y t$,

where G_x and G_y are frequency encoding and phase encoding gradient strengths, respectively. γ is the gyromagnetic ratio, t_y is the duration of the G_y gradient pulse and t is the data acquisition time. The integrations are performed over the data acquisition window. Magnetization density can be obtained by Fourier transforming $S(k_x, k_y, t)$ with respect to k_x and k_y as:

$$M_r(x, y) = \int \int_{k_x, k_y} S(k_x, k_y, t) e^{-j(k_x x + k_y y)} dk_x dk_y . \quad (2.18)$$

The resulting complex MR image is expressed as:

$$M_r(x, y) = M(x, y) e^{j[\gamma B(x, y)t + \theta_c]} . \quad (2.19)$$

When a current is applied to a conductor object in synchronization with MRI pulse sequence as seen in Figure 2.3, then the component of the magnetic flux density (due to the current flow) parallel to the main magnetic field accumulates a phase in the acquired signal. This is formulated as:

$$S(k_x, k_y, t) = \int \int_{x, y} M(x, y) e^{j[\gamma B(x, y)t + \theta_c + \gamma B_{J, z}(x, y)T_c + k_x x + k_y y]} dx dy . \quad (2.20)$$

where, $B_{J, z}(x, y)$ is the component of the magnetic field in the direction of the main magnetic field induced by the applied current. T_c is the total current injection duration.

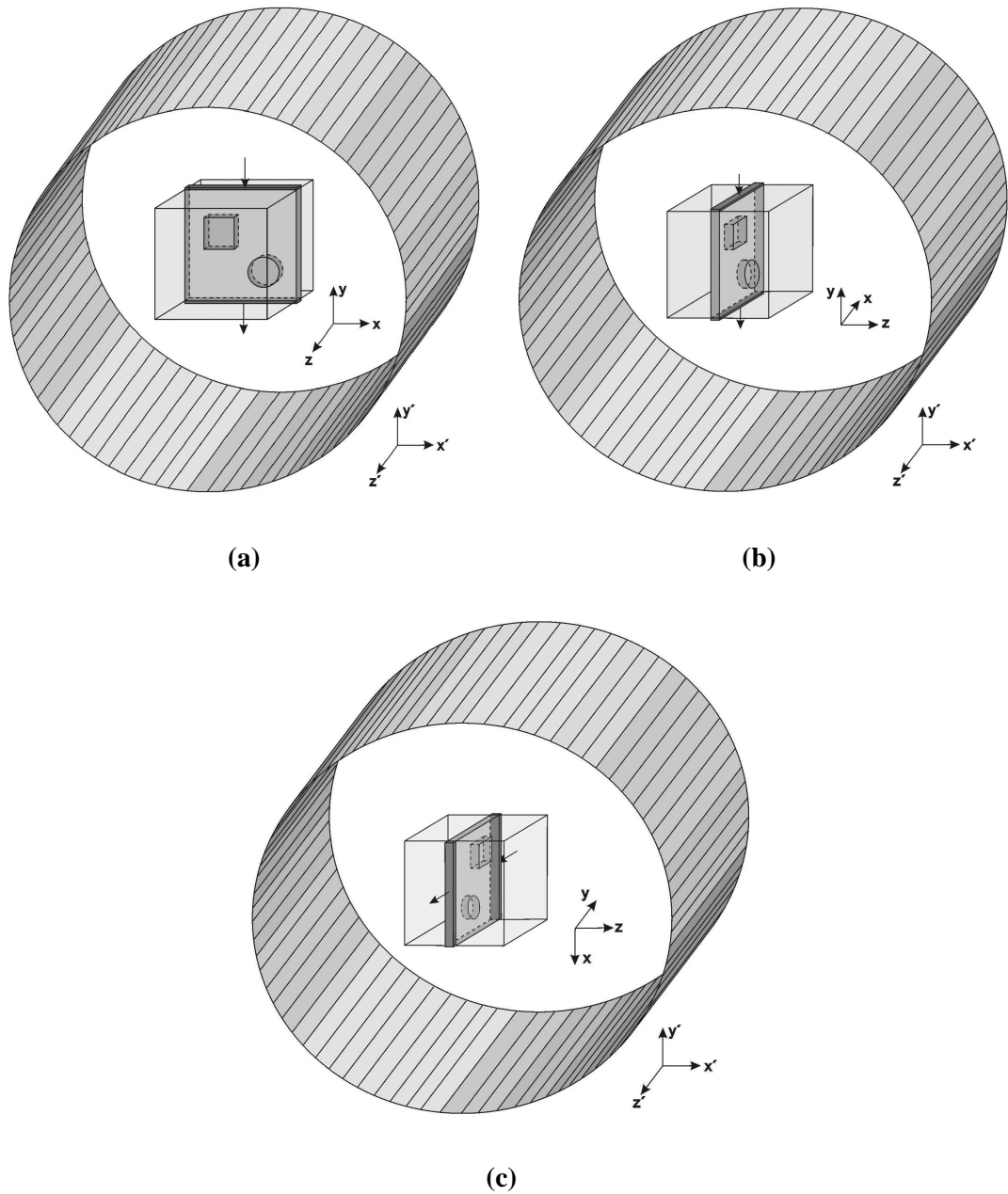


Figure 2.2: Orientation of an object inside the MRI system for measuring three components of the induced magnetic flux density. The electrodes and current injections are shown for each case. Object placement, (a) to measure B_z , (b) to measure B_x , (c) for to measure B_y .

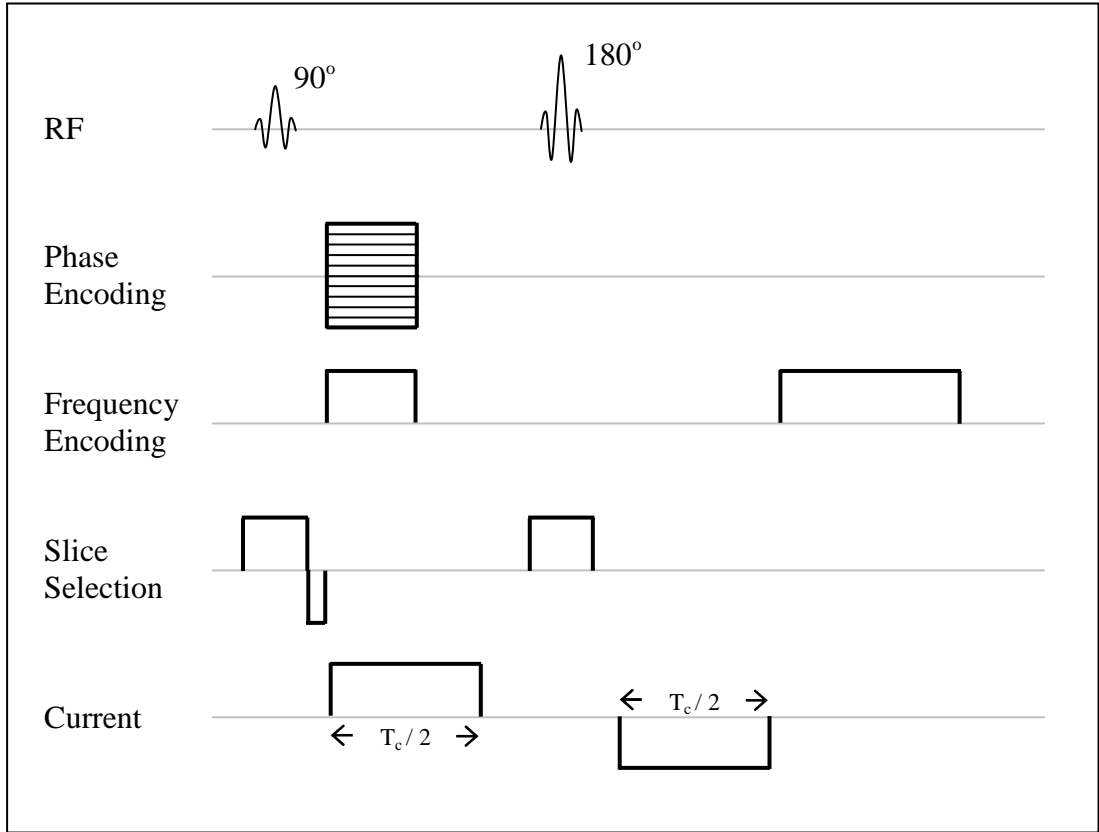


Figure 2.3: MR-CDI pulse sequence.

Fourier transforming the Equation (2.20) with respect to k_x and k_y yields the complex MR image as:

$$M_{r,j}(x, y) = M(x, y)e^{\left\{j\gamma\left[B(x,y)t+B_{j,z}(x,y)T_c\right]+j\theta_c\right\}}. \quad (2.21)$$

where, $B_{j,z}(x, y)$ is the component of the magnetic field in the direction of the main magnetic field induced by the applied current. T_c is the total current injection duration.

As seen from Equations (2.19) and (2.21), expressions are the same except an exponential term caused by the applied current. Therefore dividing the complex

image with current flow to the complex image without current flow eliminates the effects of the phase inhomogeneities and other image artifacts and following equation is obtained:

$$\frac{M_{r,J}(x, y)}{M_r(x, y)} = \frac{M(x, y)e^{\{j\gamma[B(x,y)t+B_{J,z}(x,y)T_c]+j\theta\}}}{M(x, y)e^{j[\gamma B(x,y)t+\theta]}} = e^{j\gamma B_{J,z}(x,y)T_c}. \quad (2.22)$$

Note that, resultant phase is the difference of two phase images. In practice, the ratio in Equation (2.22) is not calculated but instead, phase of Equation (2.21) is subtracted from phase of Equation (2.19). Finally, $B_{J,z}(x, y)$ is extracted from the phase in equation (2.22) as:

$$B_{J,z}(x, y) = \frac{\theta_{JN}(x, y)}{\gamma T_c}. \quad (2.23)$$

where, θ_{JN} is the difference of the phases of $M_{r,J}$ and M_r , which is also called the *normalized* phase image [7], [47]. The resolution of the magnetic flux density image in z-direction is equal to the resolution of the MR image. As explained earlier, experiments must be repeated for the measurement of other components of the magnetic flux density by rotating the object to align the desired component with the main magnetic field.

In some image reconstruction algorithms, magnetic flux density measurements are directly used [31], [37], while some uses the current density distribution calculated from magnetic flux density measurements [25], [27]. The relation between current density and magnetic flux density is given by the curl operator as:

$$\vec{J} = \frac{\nabla \times \vec{B}}{\mu_0}. \quad (2.24)$$

If this equation is written in open form, following relation between current density and magnetic flux density is obtained:

$$\vec{J} = \frac{1}{\mu_0} \left(\frac{\partial B_z}{\partial y} - \frac{\partial B_y}{\partial z} \right) \hat{a}_x + \frac{1}{\mu_0} \left(\frac{\partial B_x}{\partial z} - \frac{\partial B_z}{\partial x} \right) \hat{a}_y + \frac{1}{\mu_0} \left(\frac{\partial B_y}{\partial x} - \frac{\partial B_x}{\partial y} \right) \hat{a}_z. \quad (2.25)$$

As seen from Equation (2.25), the magnetic flux density generated by the current flow in x - y plane has only z component on that plane. In other words, $B_x = B_y = 0$ for $z = z_0$ plane and it is sufficient to measure B_z on that plane. Although x and y components are zero on that plane, their derivatives with respect to z are not necessarily zero. Therefore, in order to calculate $\frac{\partial B_x}{\partial z}$ and $\frac{\partial B_y}{\partial z}$, B_x and B_y must be measured on some near planes of z_0 . If B_x and B_y are measured on $z_0 + \Delta z$ and $z_0 - \Delta z$ planes, their derivatives are calculated as:

$$\left. \frac{\partial B_x}{\partial z} \right|_{z=z_0} = \frac{B_x|_{z=z_0+\Delta z} - B_x|_{z=z_0-\Delta z}}{2\Delta z}, \quad (2.26)$$

and

$$\left. \frac{\partial B_y}{\partial z} \right|_{z=z_0} = \frac{B_y|_{z=z_0+\Delta z} - B_y|_{z=z_0-\Delta z}}{2\Delta z}. \quad (2.27)$$

In experimental study, it is possible to measure the magnetic flux density at two neighboring slices of the imaging plane and the gradient in z direction can be calculated using these formulas.

2.5 Phase Unwrapping

In general, it is not trivial to obtain the phase term $\theta_{JN}(x, y)$ for a complex image distribution. $\theta_{JN}(x, y)$ is defined only in the principal value range of $[-\pi, \pi]$ and any phase value outside this range is wrapped to this interval yielding the wrapped phase image. Hereafter $\theta(x, y)$ will be used to denote the desired phase image and $\hat{\theta}(x, y)$ will be used to represent the wrapped phase image. The relation between $\theta(x, y)$ and $\hat{\theta}(x, y)$ is:

$$\theta(x, y) = \hat{\theta}(x, y) \pm l(x, y) \cdot 2\pi \quad (2.28)$$

where $l(x, y)$ is an integer valued function [48]. Since the magnetic flux density is directly proportional to the actual phase image, $\theta(x, y)$, a phase unwrapping algorithm that reconstructs actual phase from the wrapped phase is needed.

In this study, phase unwrapping algorithm proposed by Liang [48] and implemented by Birgül [46] is used. In this method, the unwrapped phase function is represented as the sum of a truncated Taylor series and a residual function and the unwrapping problem is converted to a parameter estimation problem. The key point behind the algorithm is that, the derivatives of the actual and wrapped phase images are equal to each other except at the points where a phase wrap occurs. The idea is to compute the phase derivatives and use them for unwrapping. In Liang's approach, the MRI phase image is represented by a polynomial and $\theta(x, y)$ is expressed as:

$$\theta(x, y) = P(x, y) + r(x, y) \quad (2.29)$$

where $P(x, y)$ is truncated Taylor series which is an N^{th} order polynomial defined by:

$$P(x, y) = \sum_{n=0}^N \sum_{m=0}^n C_n(m) x^{n-m} y^m \quad (2.30)$$

and $r(x, y)$ is the corresponding residual function. Therefore, the problem is now to determine the coefficients and the residual function. The algorithm has three main steps:

1. *Calculation of the phase derivatives*

Desired derivatives, $\frac{\partial \theta(x, y)}{\partial x}$ and $\frac{\partial \theta(x, y)}{\partial y}$, are calculated using fast Fourier transform (FFT) algorithm.

2. *Calculation of the polynomial coefficients*

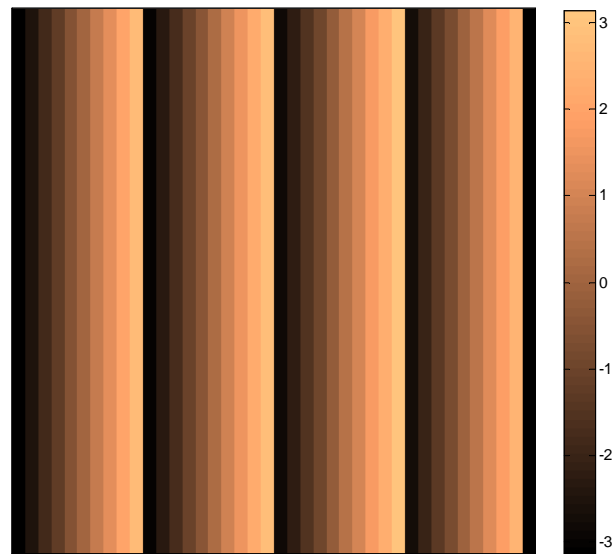
The polynomial coefficients, $C_n(m)$ for $0 \leq n \leq N, m \leq n$ are calculated by fitting $\frac{\partial P(x, y)}{\partial x}$ and $\frac{\partial P(x, y)}{\partial y}$ to $\frac{\partial \theta(x, y)}{\partial x}$ and $\frac{\partial \theta(x, y)}{\partial y}$ either separately or jointly. It is stated in [48] that joint fitting method is better, so it is preferred here. The coefficients are calculated by solving the weighted least squares problems defined as minimization of the weighted sum of squares of the difference between derivative of the wrapped phase images and the polynomial functions. The weighting factor is one when the magnitude of the MR image is above some threshold and zero otherwise.

3. *Calculation of the residual function*

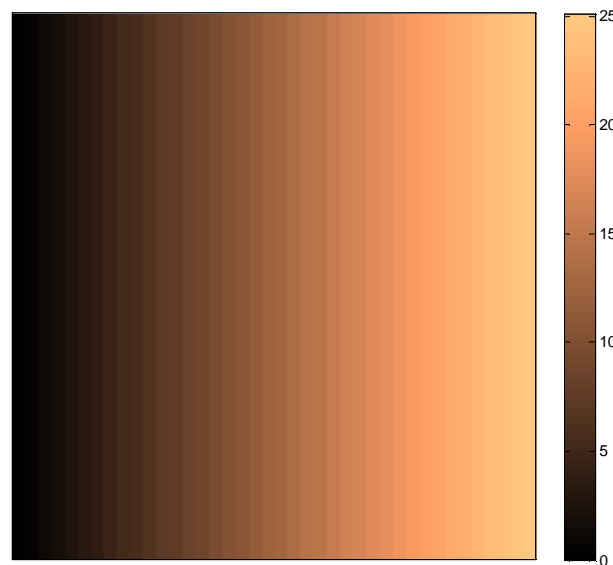
Once the coefficients ($C_n(m)$'s) are found, the polynomial function $P(x, y)$ can be wrapped to obtain $\hat{P}(x, y)$. The difference between wrapped polynomial, $\hat{P}(x, y)$, and the measured wrapped phase, $\hat{\theta}(x, y)$, is calculated and set as the residual function $r(x, y)$.

The effect of phase unwrapping is shown on Figure 2.4. In Figure 2.4(a), the colorbar axis is in radians, and it is seen that the wrapped image only takes values in

the $[-\pi, \pi]$ range and sudden jumps, in another words phase wraps, occur in this image. In the unwrapped image (Figure 2.4(b)), the phase wraps are removed. It is important to note that, MR images have random phases for points in the field of view without NMR active nuclei. Therefore, phase images should be masked using a mask based on the amplitude image before applying the phase unwrapping algorithm.



(a)



(b)

Figure 2.4: Demonstration of unwrapping: (a) Phase image before unwrapping, and (b) after unwrapping.

CHAPTER 3

EXPERIMENTAL SETUP

3.1 Introduction

Magnetic Resonance Electrical Impedance Tomography utilizes a spin echo pulse sequence together with a bipolar DC current source. This current source does not exist in conventional MR systems. Therefore, a current source which is controlled by the pulse sequence generation software of the MRI system to ensure the synchronization is required to generate the required bipolar DC current pulse. In Section 3.2, the synchronized DC current source is explained in detail. Furthermore, in order to realize MREIT experiments, a phantom which has a closed volume and current injection electrodes on the surface is designed and manufactured. A detailed explanation of this phantom is given in Section 3.3.

3.2 Current Source

As explained in the previous chapter, in order to measure the magnetic flux density generated by the internal distribution of injected currents, applied current must be in synchronization with the spin echo pulse. During this thesis study, a synchronized voltage controlled DC current source is implemented. Block diagram of the current source is given in Figure 3.1. In order to avoid RF interference, main part of the current source is placed in the Faraday cage and this part is connected to the system control unit using fiber optic cables. Likewise, in order to prevent 50 Hz noise of the electrical network and switching noise of the AC/DC converter to go into Faraday cage, main part of the current source is supplied by batteries.

Fiber optic transmitter part of the current source converts the control signal of the current pulse sequence to the optical signal. Positive and negative currents in the pulse sequence are first produced as two 5 V signals by the National Instrument (NI) digital to analog converter board's two separate channels. These signals are then converted to the optical signal in the fiber optic transmitter unit and carried with two separate fiber optic cable. Fiber optic transmitter circuit is shown in Figure 3.2. Required power for the operation of the transmitters is supplied by a 5V adapter. Transmitter and receiver circuits are designed according to the length of the fiber optic cable used between them. Fiber optic cables are fed into the Faraday cage and connected to the fiber optic receiver unit.

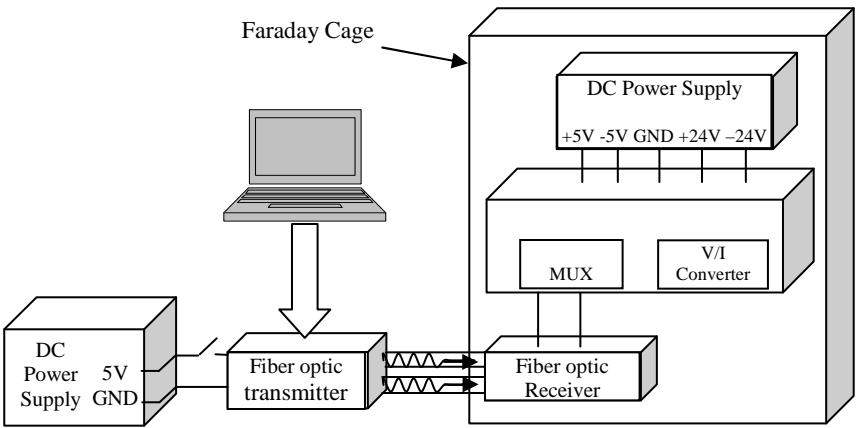


Figure 3.1: Block diagram of the current source.

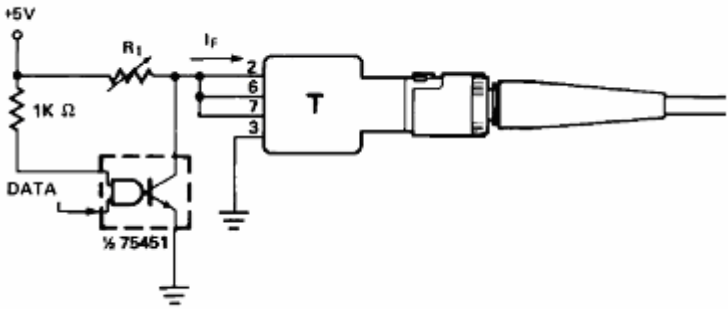


Figure 3.2: Fiber optic transmitter circuit (Agilent HFBR 2412)

Optical signals on the fiber optic cables are then converted to the 5 V electrical signals in the fiber optic receiver unit. This unit is shown in Figure 3.3. Outputs of two channel fiber optic receivers are connected to the multiplexer.

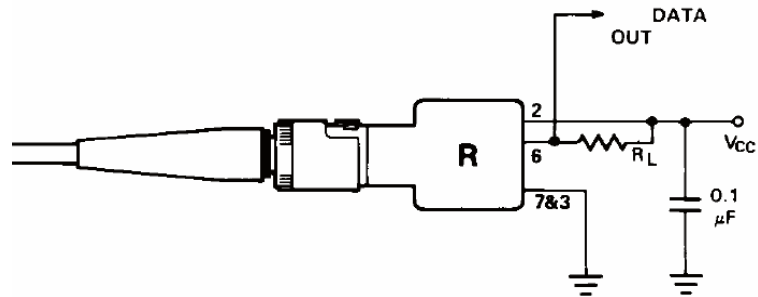


Figure 3.3: Fiber optic receiver circuit (Agilent HFBR 2412)

CD 4051 integrated circuit is used as analog multiplexer in the current source circuit. Connection diagram can be seen in Figure 3.4. S0 and S1 digital inputs are connected to the outputs of fiber optic receivers as mentioned previously. 0 V, +5 V and -5 V voltages are connected to the A0, A1 and A2 analog inputs of the multiplexer, respectively. Other inputs are not used.

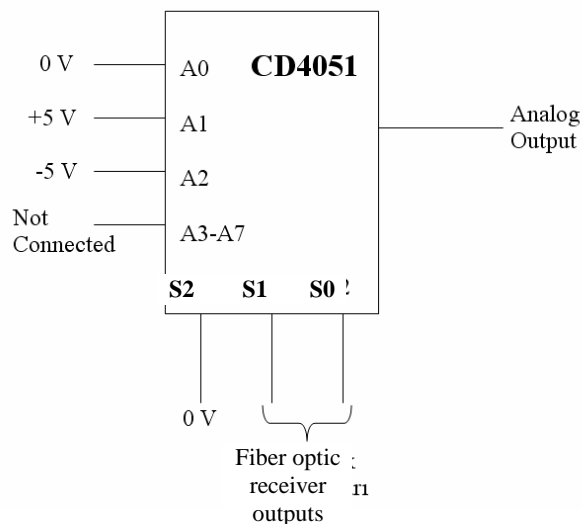


Figure 3.4: CD4051 Analog multiplexer connection diagram

The truth table for the multiplexer is given in Table 3.1. If 0 V is applied to both inputs, output becomes 0 V. If one of these signals is +5 V or -5 V, then this signal appears at the output of the multiplexer.

Table 3.1: CD4051 truth table.

S2	S1	S0	ON
0	0	0	A0
0	0	1	A1
0	1	0	A2
The rest are not used.			X

The last part of the current source is the voltage to current converter unit. In this unit 3 OPA452T operational amplifiers are used. Supply voltages of the op-amps are provided by batteries. Analog output of the multiplexer is connected to the V_I input of the voltage to current converter as seen in Figure 3.5. In this figure, Z_L shows the load impedance and I_L shows the constant current applied to the load. Load voltage V_L is sensed through a voltage buffer by the second op-amp. The third op-amp takes the difference of V_I and V_{O2} . By doing so, the difference between V_{O3} and V_L therefore, the difference between I_L and I_2 are kept constant. If the overall circuit is analyzed, following equation is obtained:

$$I_L = I_2 = -V_I / R_2 \quad (3.1)$$

As seen from equation (3.1), load current is independent from load impedance. Amplitude of the load current can be changed by only changing V_I and R_2 values. When the input voltage becomes -5 V, 0 V or 5 V, I_L current can be adjusted in the 0 – 100 mA interval independent of load impedance using the variable resistance R_2 (Upper limit of the current is defined also by the supply voltage).

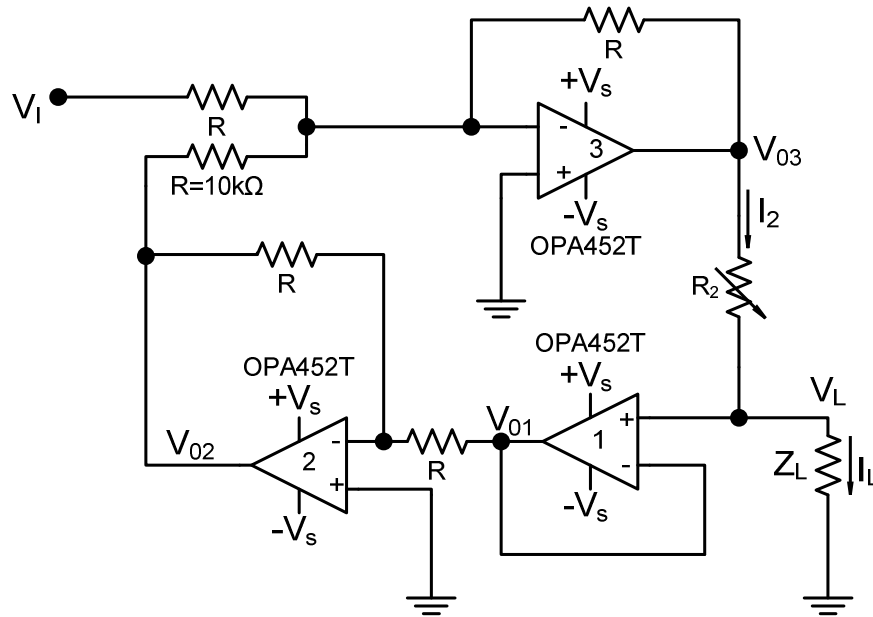


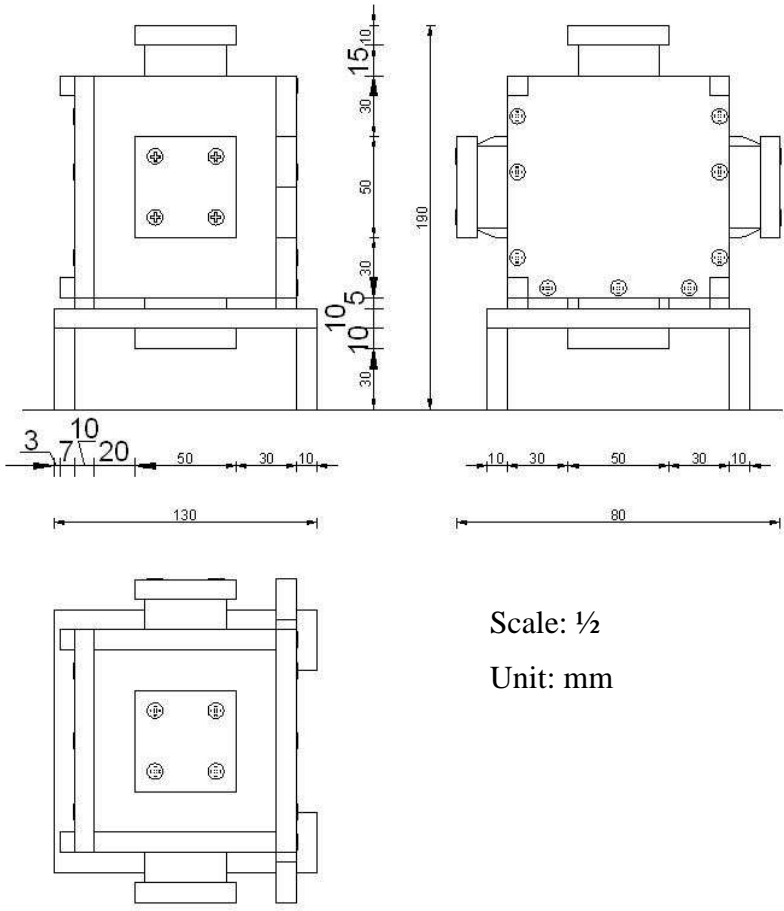
Figure 3.5: Voltage to current converter circuit

3.3 Phantom

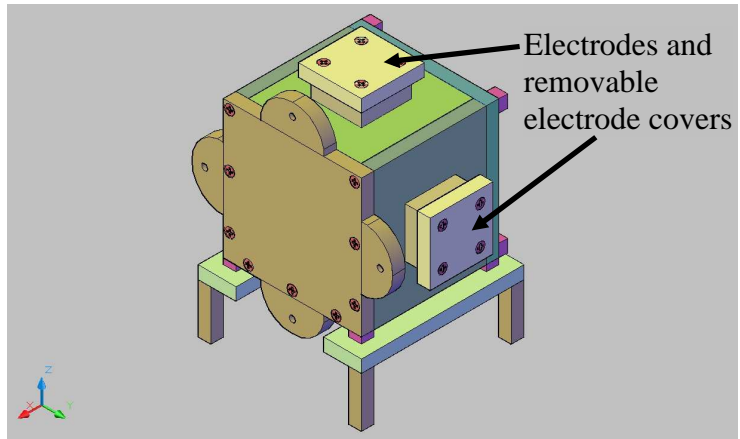
In order to test the proposed algorithms under real experimental conditions, the easiest way is to design and manufacture a phantom in which magnetic field measurements will be made while applying current. For this purpose an experimental phantom is designed and manufactured in this study. Some important aspects are taken into account during the design process of the phantom, which are;

- Since this phantom is placed inside the RF coil, its dimension is designed to fit and to be rotated in three directions inside the RF coil.
- One side of the phantom is designed as cover, to easy filling and emptying of the phantom with experimental material.
- Recessed electrodes are used to avoid signal loss due to the high current density under electrodes.
- Electrodes are designed to allow change of electrode materials when needed.
- In order to define the position of the slice during an experiment, a position marker is built on one side of the phantom.

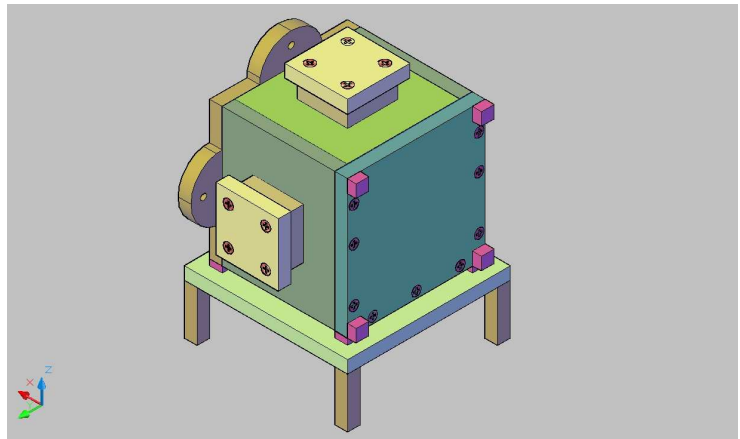
Technical drawing of the phantom is given in Figure 3.6. Since, this phantom will be used in the MR system, manufacturing material of the phantom is required to be selected as non MR active material. For this purpose, Plexiglas material was chosen.



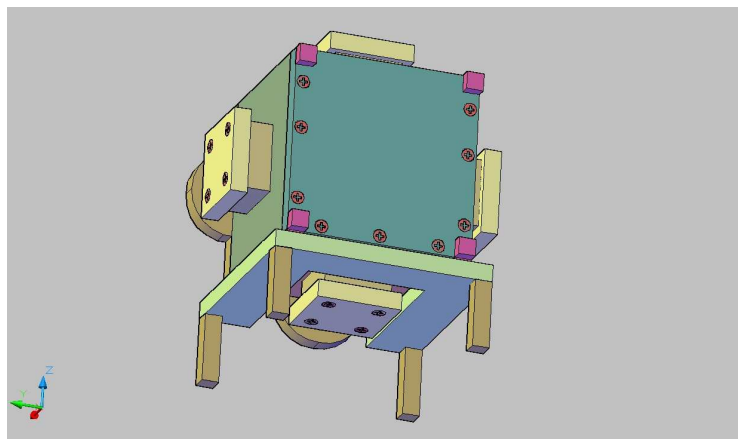
(a)



(b)



(c)



(d)

Figure 3.6: Designed phantom; (a) Technical drawing, (b) (c) (d) Views from several directions.

As seen from Figure 3.6, four electrodes are placed on four edges of the phantom. These electrodes are used for both current injection and potential measurements. Six different current injection profiles were provided using opposite and adjacent pairs of electrodes separately. 20 mA current was applied in each profile. Potential measurements were also made from the same electrodes used for current injection with a floating multimeter. Photographs of the manufactured phantom are given in Figure 3.7.

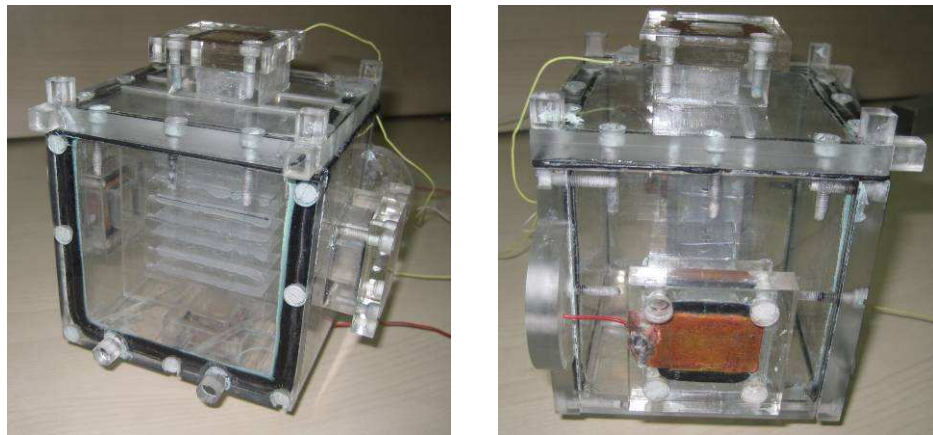


Figure 3.7: Photographs of the manufactured phantom.

After the production of the phantom and definition of the current injection profiles, the new subject was the internal material which will be placed inside the phantom. For this purpose, two different experimental phantoms was designed, simulated on the computer and produced physically. Three dimensional and cross sectional images of these two phantoms are given in Figure 3.8.

In the first phantom, shown in Figure 3.8 (a) and (b), in order to prevent flow of current in one direction in the middle section of the imaging slice two 3 cm insulator layers were placed. By doing so, an anisotropic conductivity is obtained in the vicinity of the layers. A 3 by 3 cm square object with 2 S/m conductivity value was prepared outside and placed between the layers. For this object, 1.75 gr Salt, 0.1 gr CuSO_4 , 1 gr Agar **Error! Reference source not found.** and 1 gr TX151

Error! Reference source not found. are mixed in 100 ml pure water while heating the mixture. After boiling, the mixture is poured in a 3 by 3 cm square mold and waited about 2 hours. After this time, solidified material is removed from the mold and placed between the layers. For the background material, a similar material with 0.2 S/m was prepared. In this case, 0.1 gr CuSo₄, 0.2 gr TX150 **Error! Reference source not found.**, 2 gr TX151 were mixed in 100 ml pure water but heating did not opened in this time. After the mixing about 10 minutes, a liquid material was obtained and poured remaining inner parts of the phantom.

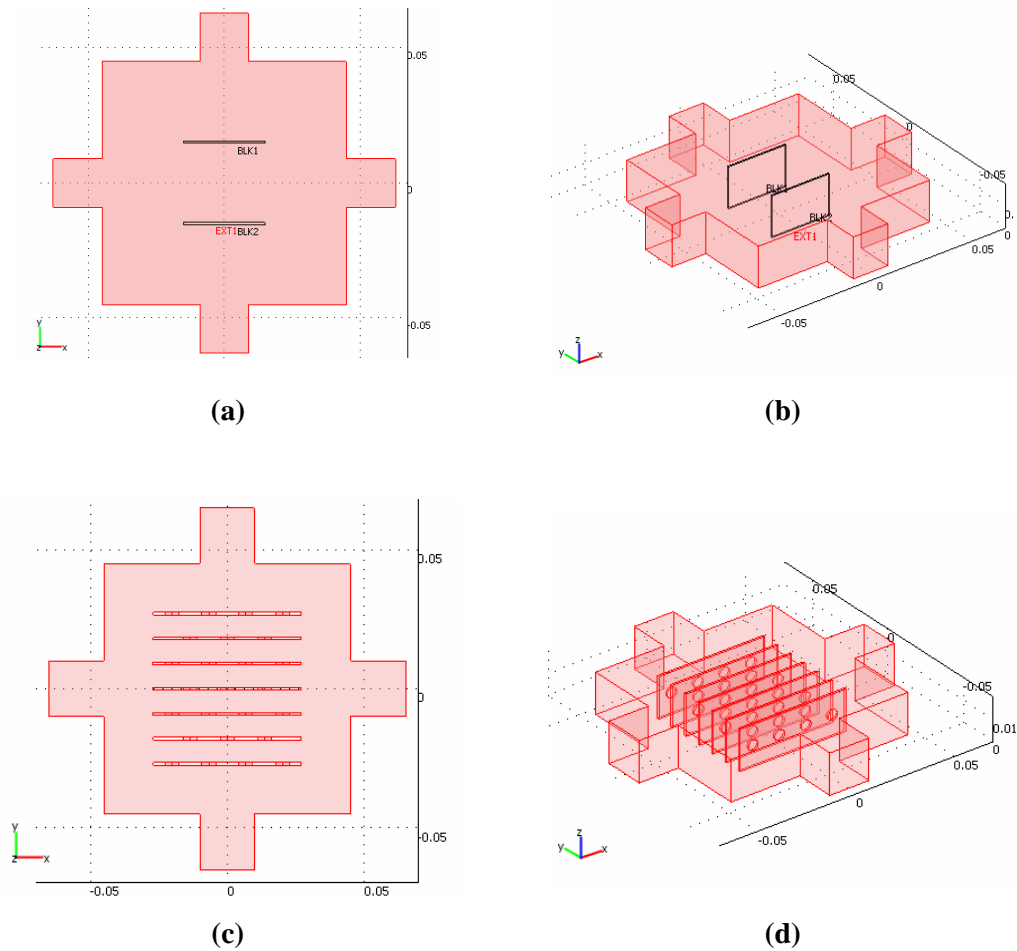


Figure 3.8: Designed two experimental phantoms: ((a) and (c)) Cross sectional, ((b) and (d)) Three dimensional images.

Since the layers placed inside the first phantom are completely insulator, anisotropy ratio could not be controlled according to the position. Because of this, second test phantom was designed and holes are opened on the layers in order to change the anisotropy controllably. There are 7 layers in the phantom as seen on the Figure 3.8 (b) and (c). First, third, fifth and seventh layers have four holes while the other layers have three holes. Remaining part of the phantom are filled with mixture of 0.1 gr CuSO_4 and 0.145 gr NaCl in 100 ml pure water which has a conductivity of 2 S/m. Because of hollow insulator layers, current can only flow inside of these holes. Using different numbers of holes in each layer, flow of current in different paths was ensured. Therefore, when the current is applied between different electrode pairs, different current paths occur and anisotropic conductivity is obtained.

Overall MREIT setup is given in Figure 3.9. Using this setup, data acquisition process was completed for both of the phantoms and magnetic field distributions were calculated as explained in the previous chapter.

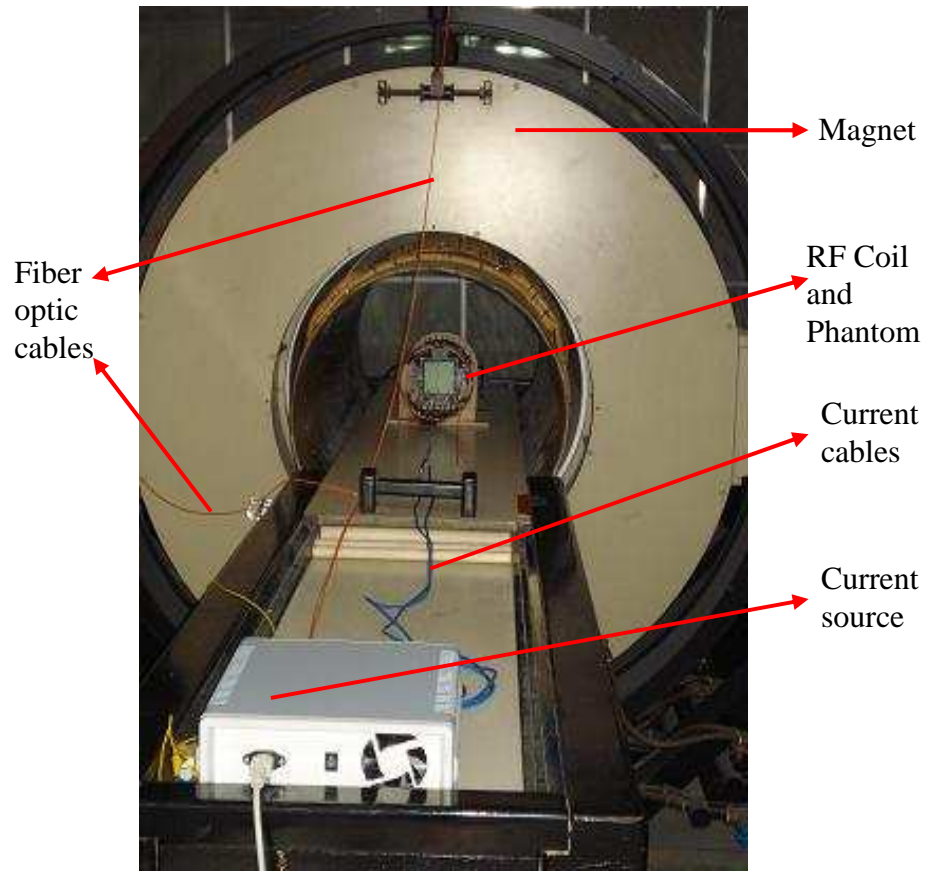


Figure 3.9: METU EEE MRI System and MREIT experiment setup.

CHAPTER 4

CURRENT DENSITY BASED RECONSTRUCTION ALGORITHMS

4.1 Introduction

In anisotropic MREIT technique, the aim is to find the anisotropic conductivity distribution inside a conductor object from measured magnetic flux density and peripheral voltage measurements. This procedure is called as the image reconstruction or the inverse problem of anisotropic MREIT. For the solution of the inverse problem, two different types of image reconstruction algorithms are proposed. The first type uses current density distribution calculated from magnetic flux density measurements (*Type-I*). This type of reconstruction requires magnetic flux density measurements in three directions. In the second type, magnetic flux density is used directly in image reconstruction and it is possible to reconstruct conductivity images using magnetic flux density measurement in one direction (*Type-II*). In this chapter three anisotropic conductivity reconstruction algorithms which are classified as *Type-I* are presented. In section 4.2, the first algorithm namely Equipotential Projection Based anisotropic conductivity reconstruction algorithm is given. Anisotropic J-substitution and anisotropic Hybrid J-substitution conductivity reconstruction algorithms are explained in detail in section 4.3.

4.2 Equipotential Projection Based Anisotropic Conductivity Reconstruction Algorithm

4.2.1 Introduction

In this part of the study, a novel MREIT reconstruction algorithm is proposed for the solution of the inverse problem. The algorithm uses the current density distribution calculated from magnetic flux density measurements. This calculation is given in chapter 2. In this algorithm, the difference between calculated and measured current density distributions is minimized iteratively. Algorithm start from an initial conductivity distribution and the procedure is iterated by assigning calculated conductivity as initial conductivity. The detailed explanation of the algorithm is given in the next section. Performance tests of the algorithm using computer and experimental models are given in results chapter.

4.2.2 Algorithm

The proposed algorithm, which is based on the construction of equipotential lines in the FOV at each iteration, reconstructs $\overline{\sigma}$ iteratively using only current density measurements. Since equation (2.4) uses potential gradient not the potential itself, the potential values assigned to these equipotential lines may be any value satisfying the correct potential gradient distribution. Therefore, reconstructed anisotropic conductivity distribution is a relative distribution. In order to find the true conductivity values, at least one potential or conductivity measurement is needed to scale the reconstructed conductivity values.

After the internal current density distribution is measured, the anisotropic conductivity reconstruction algorithm is realized for a rectangular object as follows. It can also be easily adapted for other geometries since the algorithm operates pixel-by-pixel instead of entire FOV.

(i) *Calculation of pseudo-surface potential values:*

Calculation of anisotropic conductivity values needs only the potential gradients in the FOV; therefore it is sufficient to obtain potential gradient values throughout boundary columns. For this purpose, equation (2.4) is rearranged and solved for $\nabla\phi_y$

$$\nabla\phi_y = \frac{J_y\sigma_{xx} - J_x\sigma_{yx}}{\sigma_{xy}\sigma_{yx} - \sigma_{xx}\sigma_{yy}}. \quad (4.1)$$

An equation for $\nabla\phi_x$ is also obtained similarly. Known conductivity values are assigned to the boundary pixels in order to calculate $\nabla\phi_y$ on the left and right most boundary layers and $\nabla\phi_x$ on the upper and lower most boundary layers. In practice, this structure can be achieved by wrapping a conductive belt with a known conductivity, around the object to be imaged. Then potential gradients along all boundary pixels are calculated. Based on these potential gradients, potential values of the boundary pixels are calculated by assigning a potential value to any pixel on the boundary. In this paper, these potentials are called as pseudo-potentials since they are not the true potential values but the values satisfying the calculated $\nabla\phi$ components. Potential values are assigned to the points at the centre of each boundary pixel. If an equipotential line starts from a point which is not the central point of a boundary pixel, then potential value of that equipotential line is estimated by linearly interpolating the nearest potential values, prior to constructing equipotential lines.

For object geometries other than the rectangular geometry, boundary layer potentials can be calculated using $\nabla\phi_x$ and $\nabla\phi_y$ values simultaneously. In such a case, nearest lines between centres of each neighbouring boundary layer pixels are determined then integral of

potential gradients are calculated along these lines starting, from an initial potential in order to find the boundary layer potentials.

- (ii) *Calculation of the angle between equipotential lines and current lines and construction of equipotential lines:*

Let $J(x,y)$ be an $n \times n$ matrix representing distribution of measured current density vectors (where $(x,y) \in S$). The angle between the equipotential lines and the current vectors are determined by the conductivity anisotropy at the crossing point. In order to find this angle, the ratio of $\nabla\phi_y$ and $\nabla\phi_x$ from equation (2.4) is obtained as:

$$\frac{\nabla\phi_y}{\nabla\phi_x} = \frac{J_y\sigma_{xx} - J_x\sigma_{yx}}{J_x\sigma_{yy} - J_y\sigma_{xy}}. \quad (4.2)$$

Here σ_{xx} , σ_{xy} , σ_{yx} and σ_{yy} are the anisotropic conductivity components, J_x and J_y are the measured current density components in x and y directions, respectively. Notice that, this ratio is nothing but the tangent of the $\nabla\phi$ line at a point (x,y) whose anisotropic conductivity values are σ_{xx} , σ_{xy} , σ_{yx} and σ_{yy} , and current density components are J_x and J_y . Then, angle of the $\nabla\phi$ line at this point can be expressed with the following equation:

$$\alpha_{\nabla\phi}|_{(x,y)} = \tan^{-1} \left(\frac{J_y\sigma_{xx} - J_x\sigma_{yx}}{J_x\sigma_{yy} - J_y\sigma_{xy}} \right) \Big|_{(x,y)}, \quad (x,y) \in S. \quad (4.3)$$

Since equipotential lines are perpendicular to $\nabla\phi$ lines, equation (4.3) is sufficient for the calculation of the angles of equipotential lines. Note that, at the first iteration it is impossible to perform the angle calculation, since no conductivity distribution data is available at this point. Because

of that, equipotential lines are assumed to be perpendicular to the current vectors at the first iteration.

After calculating the angles for the entire FOV, an equipotential line is initiated from the boundary of a left-most pixel and projected through each pixel, with strictly satisfying the angle condition of the corresponding pixel, to any other boundary of the FOV. This process is initiated at new points in all left most pixels except the pixels which are under the current electrodes. Since the angle between an equipotential line in a pixel and the current vector of that pixel is definite, all equipotential lines in a pixel starting from different points follow parallel but different paths and never cross each other. Therefore, infinitely many equipotential lines can be initiated. In our study, five equipotential lines are initiated for each boundary layer pixel. The same procedure is also repeated starting from the right-most, the top and the bottom pixels. After constructing the equipotential lines, the potential distribution inside the object can be obtained.

- (iii) *Determination of internal potential distribution and calculation of its gradient for the entire imaging region:*

This step is nothing more than projecting boundary potentials into the pixels through which equipotential lines pass. Since more than one equipotential line may pass through a pixel due to the finite size of the pixel, the potential value at these pixels are calculated as the weighted sum of these potentials as,

$$\varphi_n = \frac{\sum_{i=1}^N d_i \cdot e_i}{\sum_{i=1}^N d_i} \quad (4.4)$$

where, φ_n is the pixel's potential value, d_i is the length of the i^{th} equipotential line in the pixel, e_i is the potential value of the i^{th} equipotential line and N is the number of equipotential lines crossing the pixel. If no equipotential line passes through a pixel then potential value of this pixel is estimated by the weighted sum of eight neighboring pixels as

$$\varphi_m = \frac{1}{N} \sum_{i=1}^8 \varphi_i w_i \quad (4.5)$$

where, φ_m is the pixel's calculated potential value, φ_i is the potential value of the i^{th} neighboring pixel, w_i is the corresponding weighting factor and N is the number of the pixels whose value is not zero. The contribution of a neighboring pixel to the missing potential value of a pixel is taken as inversely proportional to the distance between these pixels. Two weights are used in this application; one is for diagonally neighboring pixels and the other for non-diagonally neighboring pixels.

The weights are $w_d = \frac{2}{\sqrt{2}+1}$ and $w_{nd} = \frac{2\sqrt{2}}{\sqrt{2}+1}$, respectively.

Note that, the calculated potential distribution is a relative distribution. One potential measurement is used to convert this distribution to the true distribution. A scale factor is calculated by dividing the measured potential value by the calculated pseudo-potential of the measurement pixel and then the relative distribution is scaled by this factor to obtain the true potential distribution. In case of the applications where true conductivity values are not necessary but only the contrast figure is sufficient, then reconstruction becomes possible without any potential measurement. Following the determination of the potential field ϕ , its directional gradients can be calculated by convolving $\varphi(x, y)$ with (3×3) Sobel operators. Mathematically, it can be expressed as

$$\nabla \varphi_x(x, y) = \frac{1}{8\Delta x} \begin{vmatrix} -1 & 0 & 1 \\ -2 & 0 & 2 \\ -1 & 0 & 1 \end{vmatrix} **\varphi(x, y)$$

(4.6)

$$\nabla \varphi_y(x, y) = \frac{1}{8\Delta y} \begin{vmatrix} 1 & 2 & 1 \\ 0 & 0 & 0 \\ -1 & -2 & -1 \end{vmatrix} **\varphi(x, y)$$

where, Δx and Δy are the pixel widths along the x and y directions, respectively. The size of the templates used in convolution affects the amount of smoothing. Employing a (3×3) template makes differentiation less sensitive to noise compared to a (2×2) template. However, using larger templates increases computational cost. Therefore, there is a trade off between noise sensitivity and computational cost.

(iv) A residual function is defined as

$$R = \int_S \left\| -\overline{\sigma} \cdot \nabla \varphi - \overline{J} \right\|^2 dS \quad (4.7)$$

where, $\| \cdot \|$ is an L_2 norm, J is measured current density distribution, $\nabla \varphi$ is the calculated potential gradient and S is the imaging plane. The surface integral is converted into summation over pixel elements as

$$R = \sum_j \int_{S_j} \left\| -\overline{\sigma}_j \cdot \nabla \varphi - \overline{J} \right\|^2 dS \quad (4.8)$$

where, j is the element index, $\overline{\sigma}_j$ is the anisotropic conductivity of the j^{th} element and S_j represents the surface of the j^{th} element. R is minimised with respect to each $\overline{\sigma}_j$ by setting

$$\frac{\partial R}{\partial \overline{\sigma}_j} = 0 \quad (4.9)$$

Since minimising a function with respect to a matrix means minimising it with respect to all matrix elements separately, following equation system is obtained for one current injection profile:

$$\begin{aligned} J_x^j &= \sigma_{xx}^j \nabla \phi_x^j + \sigma_{xy}^j \nabla \phi_y^j \\ J_y^j &= \sigma_{yx}^j \nabla \phi_x^j + \sigma_{yy}^j \nabla \phi_y^j \end{aligned} \quad (4.10)$$

where, σ_{xx}^j , σ_{xy}^j , σ_{yx}^j and σ_{yy}^j are the anisotropic conductivity components of the j^{th} element, J_x^j and J_y^j are the measured current density components of the j^{th} element in x and y directions, respectively and $\nabla \phi_x$ and $\nabla \phi_y$ are their potential gradients. In equation (4.10), there are four unknown anisotropic conductivity values with only two equations. In order to solve this equation system for these unknowns, at least two different current injection profiles are needed to obtain four independent equations. Since the J values are measured, if the $\nabla \phi$ values are calculated from the true potential distribution, solution of this equation system yields the unique solution. But if the $\nabla \phi$ values are calculated from a relative potential distribution, then the solution of this equation system gives a relative distribution which is not unique but the numerical values of the distribution will be directly dependent on the assigned potential value to one boundary layer pixel. For the whole

imaging system and for N different current injection profiles, equation (4.10) can be converted to the following equation system

$$\begin{aligned}
 J_x^1 &= \sigma_{xx} \nabla \phi_x^1 + \sigma_{xy} \nabla \phi_y^1 \\
 J_x^2 &= \sigma_{xx} \nabla \phi_x^2 + \sigma_{xy} \nabla \phi_y^2 \\
 &\cdot \quad \cdot \quad \quad \quad \cdot \\
 &\cdot \quad \cdot \quad \quad \quad \cdot \\
 J_x^N &= \sigma_{xx} \nabla \phi_x^N + \sigma_{xy} \nabla \phi_y^N
 \end{aligned} \tag{4.11}$$

$$\begin{aligned}
 J_y^1 &= \sigma_{yx} \nabla \phi_x^1 + \sigma_{yy} \nabla \phi_y^1 \\
 J_y^2 &= \sigma_{yx} \nabla \phi_x^2 + \sigma_{yy} \nabla \phi_y^2 \\
 &\cdot \quad \cdot \quad \quad \quad \cdot \\
 &\cdot \quad \cdot \quad \quad \quad \cdot \\
 J_y^N &= \sigma_{yx} \nabla \phi_x^N + \sigma_{yy} \nabla \phi_y^N
 \end{aligned}$$

These linear equations can be expressed in matrix-vector form as follows:

$$\underbrace{\begin{bmatrix} J_x^1 \\ J_x^2 \\ \cdot \\ \cdot \\ J_x^N \end{bmatrix}}_{\underline{J}_x} = \underbrace{\begin{bmatrix} \nabla \phi_x^1 & \nabla \phi_y^1 \\ \nabla \phi_x^2 & \nabla \phi_y^2 \\ \cdot & \cdot \\ \cdot & \cdot \\ \nabla \phi_x^N & \nabla \phi_y^N \end{bmatrix}}_{\underline{G}} \cdot \begin{bmatrix} \sigma_{xx} \\ \sigma_{xy} \end{bmatrix} \tag{4.12}$$

$$\underbrace{\begin{bmatrix} J_y^1 \\ J_y^2 \\ \cdot \\ \cdot \\ J_y^N \end{bmatrix}}_{\underline{J}_y} = \underbrace{\begin{bmatrix} \nabla \phi_x^1 & \nabla \phi_y^1 \\ \nabla \phi_x^2 & \nabla \phi_y^2 \\ \cdot & \cdot \\ \cdot & \cdot \\ \nabla \phi_x^N & \nabla \phi_y^N \end{bmatrix}}_{\underline{G}} \cdot \begin{bmatrix} \sigma_{yx} \\ \sigma_{yy} \end{bmatrix}$$

Now the new anisotropic conductivity distributions can be calculated as:

$$\begin{bmatrix} \sigma_{xx} \\ \sigma_{xy} \end{bmatrix} = \mathbf{G}^{-1} \cdot \mathbf{J}_x^{-1} \quad , \quad \begin{bmatrix} \sigma_{yx} \\ \sigma_{yy} \end{bmatrix} = \mathbf{G}^{-1} \cdot \mathbf{J}_y^{-1} \quad (4.13)$$

Since \mathbf{G} matrix is not square, direct inverse of \mathbf{G} can not be calculated. Inverse matrix is obtained by singular value decomposition (SVD). Note that, \mathbf{G} has only two Eigen values, and the inversion is made without truncation.

These four steps given above are repeated iteratively. If the difference between two consecutive conductivity images becomes less than a predefined value ε , then iterations are terminated.

Reconstruction results of the proposed technique using both simulated and experimental data are given in chapter 6.

4.3 Anisotropic J-Substitution and Anisotropic Hybrid J-Substitution Conductivity Reconstruction Algorithm

4.3.1 Introduction

Kwon *et al* [27] proposed a new isotropic conductivity reconstruction algorithm, called J-substitution algorithm, in 2002. In the study, they represented the image reconstruction as a constructive map $\{I, J, V\} \rightarrow \rho$ inside a region Ω within the subject where, I is the injected current, J is the magnitude of the current density and V is the peripheral voltage measurements. In this study, extension of that algorithm for the reconstruction of anisotropic conductivity is performed and a new anisotropic conductivity reconstruction algorithm, called anisotropic J-substitution algorithm, is proposed. Detailed explanation of the proposed algorithm is given in

Section 4.3.2. Simulation test results of the algorithm are given in the results chapter.

Furthermore in this study, a novel anisotropic conductivity reconstruction algorithm called anisotropic hybrid J-substitution algorithm is proposed. This algorithm combines the equipotential projection based anisotropic conductivity reconstruction algorithm explained in the previous chapter and anisotropic J-substitution algorithm explained in this chapter. Detailed definition of the algorithm is given in Section 4.3.3. Simulation and experimental results of these algorithms are given in the results chapter.

4.3.2 Anisotropic J-Substitution Algorithm

In this part of the study, previously proposed J-substitution algorithm which is for isotropic conductivity reconstruction is extended for the reconstruction of anisotropic conductivity. Before explaining the algorithm for anisotropic conductivity reconstruction, it will be helpful to give the underlying mathematics of the isotropic conductivity reconstruction algorithm. A general explanation about the isotropic algorithm is below.

For any given resistivity ρ of a volume Ω , the corresponding voltage V_ρ satisfies the following *BVP*:

$$\nabla \cdot \left(\frac{1}{\rho} \nabla V_\rho \right) = 0 \quad \text{in } \Omega \quad (4.14)$$

$$\frac{1}{\rho} \frac{\partial V_\rho}{\partial n} = j_l \quad \text{on } \partial\Omega \quad (4.15)$$

Related to the *BVP* in (4.14) and (4.15), following cost functional can be defined:

$$\Psi(\rho) := \int_{\Omega} \left| J^*(r) - \frac{1}{\rho(r)} E_{\rho}(r) \right|^2 dr \quad (4.16)$$

where, $J^*(r)$ is the magnitude of the measured interior current density and $E_{\rho}(r) := |\nabla V_{\rho}(r)|$ is the magnitude of the calculated electric field intensity obtained by solving (4.14) and (4.15) for a given ρ . After discretization of the model to N pixels with the same area for all Ω_k , we get the following squared residual sum R :

$$R(\sigma_0, \dots, \sigma_{N-1}) := \sum_{k=0}^{N-1} \int_{\Omega_k} \left| J^*(r) - \sigma_k E_{\rho}(r) \right|^2 dr \quad (4.17)$$

where, Ω_k is the k^{th} pixel element of the model, σ_k is the conductivity on Ω_k that is assumed to be constant at each element. To update the resistivity from the zero gradient argument for the minimization of the squared residual sum, we differentiate (4.17) with respect to σ_m for $m=0, \dots, N-1$ to get

$$\begin{aligned} 0 = \frac{\partial R}{\partial \sigma_m} &= 2 \int_{\Omega_m} E_{\rho}(r) (\sigma_m E_{\rho}(r) - J^*(r)) dr \\ &+ 2 \sum_{k=0}^{N-1} \int_{\Omega_k} \sigma_k \frac{\partial E_{\rho}(r)}{\partial \sigma_m} (\sigma_k E_{\rho}(r) - J^*(r)) dr \end{aligned} \quad (4.18)$$

This leads to the following approximate identity:

$$\begin{aligned} 0 &\approx E_{\rho}(r_m) (\sigma_m E_{\rho}(r_m) - J^*(r_m)) \\ &+ \sum_{k=0}^{N-1} \sigma_k \frac{\partial E_{\rho}(r_k)}{\partial \sigma_m} (\sigma_k E_{\rho}(r_k) - J^*(r_k)) \end{aligned} \quad (4.19)$$

for $m=0, \dots, N-1$, where r_k is the center point of the element Ω_k and we used the simplest quadrature rule. Hence, the following updating strategy to minimize the residual sum in (4.17) is obtained:

$$\frac{1}{\bar{\rho}_m} = \bar{\sigma}_m := \frac{J^*(r_m)}{E_\rho(r_m)} \quad \text{for } m = 0, \dots, N-1 \quad (4.20)$$

where, $\bar{\rho}_m$ is a new resistivity value on Ω_m and $E_\rho(r_m)$ is the calculated electric field intensity at the center point of Ω_m from an old resistivity distribution.

Explained algorithm up to here is for the reconstruction of the isotropic conductivity. Since, our aim is to reconstruct anisotropic conductivity distribution,

scalar σ (or ρ) is changed with 2×2 tensor distribution ($\bar{\sigma} = \begin{bmatrix} \sigma_{xx} & \sigma_{xy} \\ \sigma_{yx} & \sigma_{yy} \end{bmatrix}$) in the

above formulation. Very similar study had been performed in our previously proposed equipotential projection algorithm in section 4.2. In that study, interior potential distribution is found by construction of equipotential lines and projection of boundary potentials through these lines. The difference in this algorithm is that, interior potential distribution is obtained by solving the boundary value problem using finite element or finite difference methods. In our study, we preferred to use finite element method (FEM). Basics of the FEM can be found in Chapter 2. After obtaining the potential distribution inside, potential gradient, therefore electric field is calculated using 3×3 Sobel operators as in the equipotential projection algorithm. Here, it is important to note that, since there is no conductivity information at the beginning, an initial conductivity distribution is utilized for the construction of FEM structure. For the next iterations, previously found conductivity distribution is used. In order to find a updating equation, residual function defined in (4.17) is written for anisotropic conductivity. Differentiating this function and equating it for the minimization purpose, following equation system is obtained:

$$\begin{aligned} J_x^j &= \sigma_{xx}^j \nabla \phi_x^j + \sigma_{xy}^j \nabla \phi_y^j \\ J_y^j &= \sigma_{yx}^j \nabla \phi_x^j + \sigma_{yy}^j \nabla \phi_y^j \end{aligned} \quad (4.21)$$

where, σ_{xx}^j , σ_{xy}^j , σ_{yx}^j and σ_{yy}^j are the anisotropic conductivity components of the j^{th} element, J_x^j and J_y^j are the measured current density components of the j^{th} element in x and y directions, respectively and $\nabla\phi_x$ and $\nabla\phi_y$ are their potential gradients. In equation (4.21), there are four unknown anisotropic conductivity values with only two equations. In order to solve this equation system for these unknowns, at least two different current injection profiles are needed to obtain four independent equations. For the whole imaging system and for N different current injection profiles, equation (4.21) can be converted to the following equation system

$$\begin{aligned}
J_x^1 &= \sigma_{xx} \nabla\phi_x^1 + \sigma_{xy} \nabla\phi_y^1 & J_y^1 &= \sigma_{yx} \nabla\phi_x^1 + \sigma_{yy} \nabla\phi_y^1 \\
J_x^2 &= \sigma_{xx} \nabla\phi_x^2 + \sigma_{xy} \nabla\phi_y^2 & J_y^2 &= \sigma_{yx} \nabla\phi_x^2 + \sigma_{yy} \nabla\phi_y^2 \\
\cdot & \cdot & \cdot & \cdot \\
\cdot & \cdot & \cdot & \cdot \\
J_x^N &= \sigma_{xx} \nabla\phi_x^N + \sigma_{xy} \nabla\phi_y^N & J_y^N &= \sigma_{yx} \nabla\phi_x^N + \sigma_{yy} \nabla\phi_y^N
\end{aligned} \tag{4.22}$$

These linear system of equations can be expressed as follows:

$$\underbrace{\begin{bmatrix} J_x^1 \\ J_x^2 \\ \cdot \\ \cdot \\ J_x^N \end{bmatrix}}_{\underline{J}_x} = \underbrace{\begin{bmatrix} \nabla\phi_x^1 & \nabla\phi_y^1 \\ \nabla\phi_x^2 & \nabla\phi_y^2 \\ \cdot & \cdot \\ \cdot & \cdot \\ \nabla\phi_x^N & \nabla\phi_y^N \end{bmatrix}}_{\underline{G}} \cdot \begin{bmatrix} \sigma_{xx} \\ \sigma_{xy} \end{bmatrix}, \quad \underbrace{\begin{bmatrix} J_y^1 \\ J_y^2 \\ \cdot \\ \cdot \\ J_y^N \end{bmatrix}}_{\underline{J}_y} = \underbrace{\begin{bmatrix} \nabla\phi_x^1 & \nabla\phi_y^1 \\ \nabla\phi_x^2 & \nabla\phi_y^2 \\ \cdot & \cdot \\ \cdot & \cdot \\ \nabla\phi_x^N & \nabla\phi_y^N \end{bmatrix}}_{\underline{G}} \cdot \begin{bmatrix} \sigma_{yx} \\ \sigma_{yy} \end{bmatrix} \tag{4.23}$$

Now the new anisotropic conductivity distributions can be calculated as:

$$\begin{bmatrix} \sigma_{xx} \\ \sigma_{xy} \end{bmatrix} = \underline{G}^{-1} \cdot \underline{J}_x^{-1}, \quad \begin{bmatrix} \sigma_{yx} \\ \sigma_{yy} \end{bmatrix} = \underline{G}^{-1} \cdot \underline{J}_y^{-1} \tag{4.24}$$

Since \mathbf{G} matrix is not square, direct inverse of \mathbf{G} can not be calculated. Inverse matrix is obtained by singular value decomposition (SVD). Note that, \mathbf{G} has only two Eigen values, and the inversion is made without truncation. Above steps are repeated at each iteration. If the difference between two consecutive conductivity images becomes less than a predefined value ε , then iterations are terminated.

An important point here is that, under the same current pattern, two conductivity distributions σ and $\alpha\sigma$ will yield the same interior current density distribution. Therefore, using only current density distribution as input, not the true conductivity distribution but the relative distribution can be reconstructed. In order to find the true conductivity, a potential or a conductivity measurement is required as in the equipotential projection algorithm.

4.3.3 Anisotropic Hybrid J-Substitution Algorithm

As the name of this new algorithm implies, it combines two anisotropic conductivity reconstruction algorithms; one is anisotropic J-substitution algorithm explained in the previous section and the other is anisotropic equipotential projection explained in chapter 4.2. In the newly proposed hybrid technique, anisotropic conductivity is first reconstructed with anisotropic EPP algorithm and then this conductivity distribution is given to the J-substitution algorithm as the initial distribution. By doing so, it is expected to decrease the errors of anisotropic EPP algorithm and obtain a faster convergence.

Simulation and experimental test results for these two algorithms are given in the results chapter.

CHAPTER 5

MAGNETIC FLUX DENSITY BASED RECONSTRUCTION ALGORITHMS

5.1 Introduction

In the previous chapter, inverse problem of MREIT was defined and image reconstruction algorithms were classified as *Type-I* and *Type-II*. In this chapter, two anisotropic conductivity reconstruction algorithms, both are *Type-II*, are proposed. These algorithms use only the magnetic flux density measurement in one direction. Therefore, rotation of the object inside the MRI scanner is eliminated. In the following section, anisotropic Harmonic B_z conductivity reconstruction algorithm is given. Anisotropic Sensitivity conductivity reconstruction algorithm is explained in detail in section 5.3.

5.2 Anisotropic Harmonic B_z Conductivity Reconstruction Algorithm

5.2.1 Introduction

In 2003, Oh *et al* [32] proposed the Harmonic B_z algorithm for isotropic conductivity reconstruction. In that study, the relation between $\nabla^2 B_z$ and $\nabla \sigma$ was used to reconstruct conductivity distribution. Therefore, conductivity is reconstructed using only one component of magnetic field by removing the need for object rotation in the MR scanner. In this part of the thesis, extension of Harmonic

B_z for the reconstruction of anisotropic conductivity is realized and a new anisotropic conductivity reconstruction algorithm, namely anisotropic Harmonic B_z algorithm, is proposed. Detailed explanation of the proposed algorithm is given in Section 5.2.2. Simulation and experimental test results of the algorithm are given in the results chapter.

5.2.2 Algorithm

Fundamentals of the Harmonic B_z algorithm are described in [32]. Here, the proposed anisotropic conductivity reconstruction algorithm will be explained.

Algorithm starts with the following identity

$$\nabla \times \nabla \times \vec{H} = \nabla(\nabla \cdot \vec{H}) - \nabla^2 H \quad (5.1)$$

Here, since $\nabla \times \vec{H} = \vec{J}$ and $\nabla \cdot \vec{H} = 0$ hold inside a volume conductor with current flow, equation (5.2) is obtained from equation (5.1):

$$\nabla^2 H = -\nabla \times \vec{J} \quad (5.2)$$

For anisotropic conductivity distribution, current density can be written as, $\vec{J} = \overline{\overline{\sigma}} \nabla \phi$, where $\overline{\overline{\sigma}}$ is a 3 by 3 matrix. In this algorithm, $\overline{\overline{\sigma}}$ is defined as,

$$\overline{\overline{\sigma}} = \begin{bmatrix} \sigma_{xx} & 0 & 0 \\ 0 & \sigma_{yy} & 0 \\ 0 & 0 & \sigma_{zz} \end{bmatrix} \quad (5.3)$$

for simplification of the underlying mathematics. In this case, the following equation is written:

$$\vec{J} = -\vec{\sigma} \nabla \phi = - \begin{bmatrix} \sigma_{xx} & 0 & 0 \\ 0 & \sigma_{yy} & 0 \\ 0 & 0 & \sigma_{zz} \end{bmatrix} \cdot \begin{bmatrix} \nabla \phi_x \\ \nabla \phi_y \\ \nabla \phi_z \end{bmatrix} \quad (5.4)$$

Then;

$$\vec{J} = - \begin{bmatrix} \sigma_{xx} \nabla \phi_x \\ \sigma_{yy} \nabla \phi_y \\ \sigma_{zz} \nabla \phi_z \end{bmatrix}. \quad (5.5)$$

Combining equation (5.2) with equation (5.5) gives the following equation:

$$\nabla^2 \vec{H} = \nabla \times \left(\begin{bmatrix} \sigma_{xx} \nabla \phi_x \\ \sigma_{yy} \nabla \phi_y \\ \sigma_{zz} \nabla \phi_z \end{bmatrix} \right). \quad (5.6)$$

Only the z-component of this identity is written as follows:

$$\nabla^2 \vec{H}_z = \frac{\partial \sigma_{yy}}{\partial x} \cdot E_y + \frac{\partial E_y}{\partial x} \cdot \sigma_{yy} - \frac{\partial \sigma_{xx}}{\partial y} \cdot E_x - \frac{\partial E_x}{\partial y} \cdot \sigma_{xx}. \quad (5.7)$$

Taking the derivatives using forward difference method yields the following equation:

$$\begin{aligned} \nabla^2 H_z(x, y) = & \frac{\sigma_{yy}(x+1, y) - \sigma_{yy}(x, y)}{\Delta x} \cdot E_y(x, y) \\ & + \frac{E_y(x+1, y) - E_y(x, y)}{\Delta x} \cdot \sigma_{yy}(x, y) \\ & - \frac{\sigma_{xx}(x, y+1) - \sigma_{xx}(x, y)}{\Delta y} \cdot E_x(x, y) \\ & - \frac{E_x(x, y+1) - E_x(x, y)}{\Delta y} \cdot \sigma_{xx}(x, y) \end{aligned} \quad (5.8)$$

is obtained. Finally, rearranging the above equation, equation (5.9) is obtained:

$$\begin{aligned} \nabla^2 H_z(x, y) = & \sigma_{xx}(x, y) \left[\frac{2E_x(x, y) - E_x(x, y+1)}{\Delta y} \right] \\ & - \sigma_{yy}(x, y) \left[\frac{2E_y(x, y) - E_y(x+1, y)}{\Delta x} \right] \\ & + \sigma_{yy}(x+1, y) \cdot \frac{E_y(x, y)}{\Delta x} - \sigma_{xx}(x, y+1) \cdot \frac{E_x(x, y)}{\Delta y} \end{aligned} \quad (5.9)$$

As seen from equation (5.9), unknown conductivity components stay together with measured magnetic field intensity and unknown electric field data. In this algorithm, electric field is calculated using finite element method at each iteration. In order to remove the unknown conductivity values at $(x+1, y)$ and $(x, y+1)$ coordinate points while calculating the conductivity components at (x, y) point, the first row and the last column conductivity components are assumed to be known. Then equation (5.9) is rearranged as:

$$\begin{aligned} \nabla^2 H_z(x, y) - \sigma_{yy}(x+1, y) \cdot \frac{E_y(x, y)}{\Delta x} + \sigma_{xx}(x, y+1) \cdot \frac{E_x(x, y)}{\Delta y} = \\ \sigma_{xx}(x, y) \left[\frac{2E_x(x, y) - E_x(x, y+1)}{\Delta y} \right] - \sigma_{yy}(x, y) \left[\frac{2E_y(x, y) - E_y(x+1, y)}{\Delta x} \right] \end{aligned} \quad (5.10)$$

Then the unknown conductivity components at the second row and $n-1^{\text{th}}$ column can be calculated using the known conductivity values and the calculated electric field and the measured magnetic field data. This procedure continues with the third row and the $(n-1)^{\text{th}}$ column and all conductivity values in the FOV are calculated recursively. Calculation sequence is given in Figure 5.1

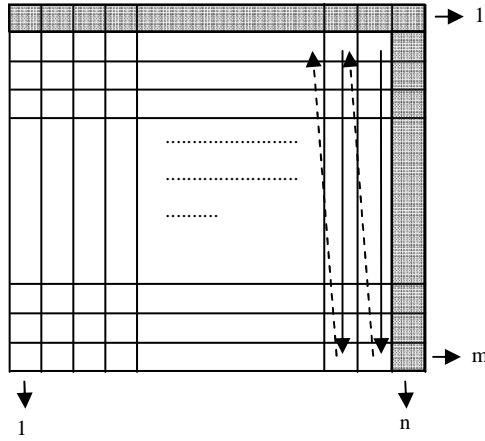


Figure 5.1: Conductivity calculation sequence for anisotropic Harmonic B_z algorithm.

Obtained results using this algorithm for both simulated and experimental data are given in chapter 6.

5.3 Anisotropic Sensitivity Conductivity Reconstruction Algorithm

5.3.1 Introduction

Birgöl and Ider proposed a new technique to find conductivity in 1995 [20]. In this technique, it is stated that when the conductivity inside an object changes, current density will change and there will be a change in the magnetic field. Therefore, if this change in the magnetic field could be measured then the inverse problem which finds the conductivity distribution can be formed and solved. Furthermore, since the change in the magnetic field can be measured with equal sensitivity in the imaging region, conductivity map will be obtained with a uniform spatial distribution. But, that study was for isotropic conductivity distribution. In this study, extension of that algorithm for anisotropic conductivity reconstruction is realized. Detailed explanation of the algorithm is given in the following section. Obtained results will be given in the next chapter.

5.3.2 Algorithm

For isotropic conductivity distribution, a linear relation between the conductivity change and change in the normal component (taken as z direction in the study) of magnetic field could be constituted with the following equation:

$$\Delta \mathbf{b} = \mathbf{S} \Delta \sigma \quad (5.11)$$

Here, $\Delta \mathbf{b}$ is the change in the magnetic flux density, $\Delta \sigma$ is the change around the first assumed conductivity value and \mathbf{S} is the sensitivity matrix. Once the sensitivity matrix is calculated, since $\Delta \mathbf{b}$ is known, required conductivity change values can be obtained from

$$\Delta \sigma = \mathbf{S}^{-1} \Delta \mathbf{b} \quad (5.12)$$

When the anisotropic conductivity distribution is employed, the sensitivity matrix must be calculated for conductivity changes of all anisotropic conductivity components. For a two dimensional distribution, equation 5.11 can be rewritten as:

$$\Delta \mathbf{b} = \mathbf{S} \begin{bmatrix} \overline{\Delta \sigma_{xx}} \\ \overline{\Delta \sigma_{xy}} \\ \overline{\Delta \sigma_{yy}} \end{bmatrix} \quad (5.13)$$

Here, $\overline{\Delta \sigma_{xx}}$ is the change in the x directed conductivity component around the initial conductivity. Similarly, $\overline{\Delta \sigma_{xy}}$ and $\overline{\Delta \sigma_{yy}}$ are the changes in off-diagonal and y directed conductivity components respectively. Again once the sensitivity matrix is calculated, required change of conductivity components can be obtained from equation (5.12).

Here, it is important to note that \mathbf{S} matrix does not have to be square and is generally singular. Therefore, its inverse can not be taken directly. In this study,

singular value decomposition based pseudo inverse was used. Also, \mathbf{S} matrix is calculated only one time for each geometry and current injection configuration and stored. This increases the speed of the algorithm significantly.

Another important aspect is that using only magnetic flux density measurements, a unique conductivity distribution could not be reconstructed. In this study, surface potential and magnetic flux density measurements are used together to reconstruct true conductivity distribution uniquely. Magnetic flux density measurements were used first, to obtain a detailed conductivity map and then, this conductivity map was scaled to satisfy the potential measurements.

Simulation and experimental results of this algorithm are given in the next chapter.

CHAPTER 6

RESULTS AND COMPARISONS

6.1 Introduction

This chapter will cover the performance test results of the reconstruction algorithms explained in the previous two chapters. Four different computer models constructed for performance evaluation of the algorithms with simulated measurements will be explained in section 6.2. In order to quantize the reconstruction accuracy, an error measure is defined. This definition is given in section 6.3. In section 6.4, simulation of the measurement noise for the test of the algorithms under noisy measurements is explained. Then simulation and experimental results of each algorithm using proposed models with and without noisy measurements will be given sequentially in section 6.5. Furthermore, final comparisons are given in section 6.6.

6.2 Conductivity Models

In this study, four different two dimensional computer models were reconstructed to investigate the performances of the reconstruction algorithms described in the previous chapters. Dimensions of all models were selected as $9\text{ cm} \times 9\text{ cm}$ in order to make the models similar to the experimental phantom used in METU EEE 0.15 T Magnetic Resonance System. 20 mA injected current was modeled in simulations again thinking the limits of the current source used in experimental studies. Four different current injection profiles were provided by the electrodes placed on the model boundaries. Electrode placements and the amount of the currents on each electrode are given in Figure 6.1 and Table 6.1, respectively.

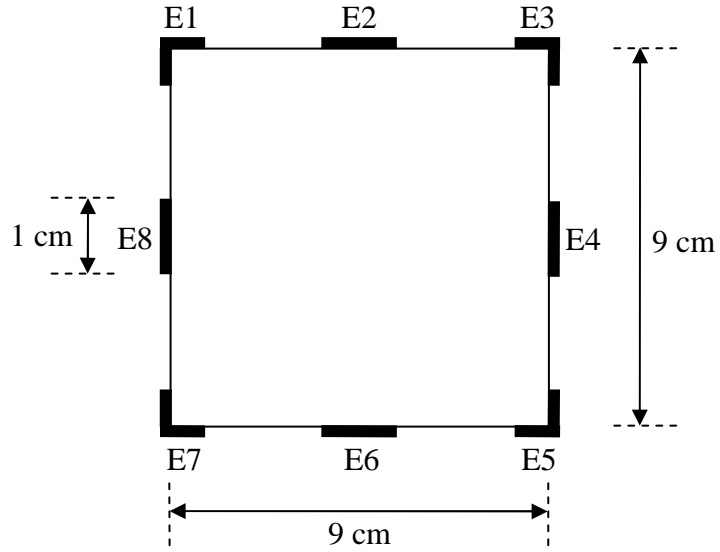


Figure 6.1: Dimensions and electrode placement of the computer model.

Table 6.1: Current amplitudes applied to the electrodes for current injection patterns I_1 , I_2 , I_3 and I_4 . Values are in mA.

	E1	E2	E3	E4	E5	E6	E7	E8
I_1	0	+20	0	0	0	-20	0	0
I_2	0	0	0	-20	0	0	0	+20
I_3	+20	0	0	0	-20	0	0	0
I_4	0	0	+20	0	0	0	-20	0

All computer models were discretized into 40×40 square elements. Therefore, two dimensional current density distribution components were generated as 40×40 matrices. Two potential measurement data were simulated for each current injection profile. These measurements were performed on the current injecting electrodes.

6.2.1 Computer Model 1

The first model constructed in this study consists of a quite difficult anisotropy with a circle shaped object in x-directed conductivity (σ_{xx}) and a square shaped object in y-directed conductivity (σ_{yy}) as seen in Figure 6.2. Radius of the circle and side length of the square was selected as 15.75 mm and 31.5 mm, respectively. The background conductivity was selected as 0.2 S/m in order to simulate the blood conductivity. Conductivity values of the anisotropic object are given in Table 6.2.

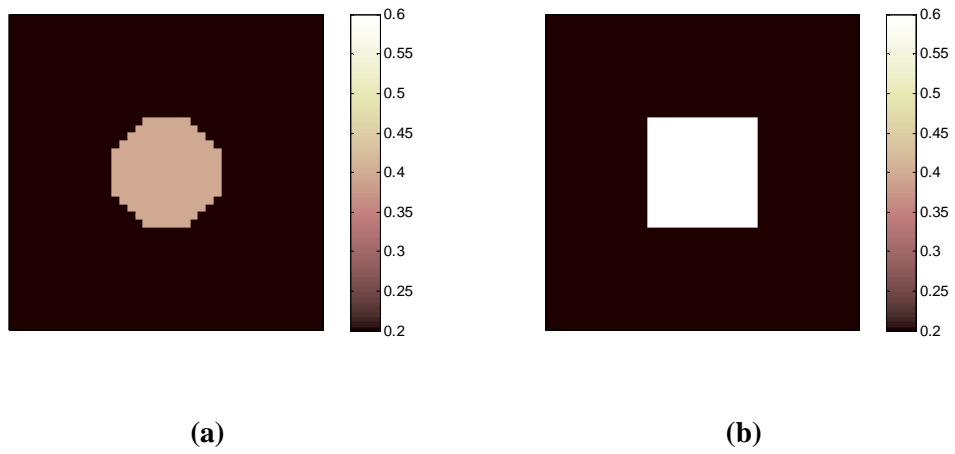


Figure 6.2: Conductivity values of Model 1: (a) x-directed conductivity (σ_{xx}), (b) y-directed conductivity (σ_{yy}).

Table 6.2: Conductivity values of Model 1. Values are in S/m.

	σ_{xx}	$\sigma_{xy} = \sigma_{yx}$	σ_{yy}
Object	0.4	0	0.6
Background	0.2	0	0.2

The reason of constructing this model is mainly to explore reconstruction accuracies of the proposed reconstruction algorithms. Furthermore, distinguishability

properties of the algorithms in case of complex anisotropic conductivity distributions will be investigated with this model.

6.2.2 Computer Model 2

Another computer model prepared in this study has two small square objects which have 2.25 mm side length. This dimension was selected to provide each square to cover a 1 pixel area in a 40×40 grid. Two squares were placed in ten different positions on a horizontal line passing through the middle of the model. Model geometry and the distances between two squares, d , are given in Figure 6.3 and Table 6.3, respectively.

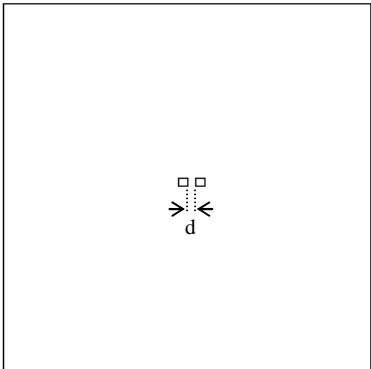


Figure 6.3: Geometry of Model 2.

Table 6.3: Distance between two squares of Model 2. Values are in mm.

Case:	1	2	3	4	5	6	7	8	9	10
d	2.25	6.75	11.25	15.75	20.25	24.75	33.75	42.75	51.75	60.75

Conductivity of the background was modeled as 0.2 S/m. Conductivity values of the squares were selected as anisotropic having a 2 S/m in x-direction and 0.02 S/m in y-direction.

The aim of this model is to define the spatial resolution properties of the proposed reconstruction algorithms. Since point spread function (PSF) contains complete information about the spatial resolution, two 1 pixel squares were modeled to obtain PSF. To express the spatial resolution by a single number, it is possible to ignore the shape of the PSF and simply measure its width. The most common way to specify this is calculating the Full Width at Half Maximum (FWHM) value. Therefore, FWHM values were computed for every d distances.

6.2.3 Computer Model 3

The third model developed in this study has again small square objects which have 2.25 mm side length but in this case they were placed on the main diagonal line of the model. 9 square elements were used having about 9.5 mm apart from each other. General model geometry can be seen in Figure 6.4. Conductivity values of the squares were selected as 2 S/m in x-direction and 0.02 S/m in y-direction whereas background conductivity was 0.2 S/m isotropic.

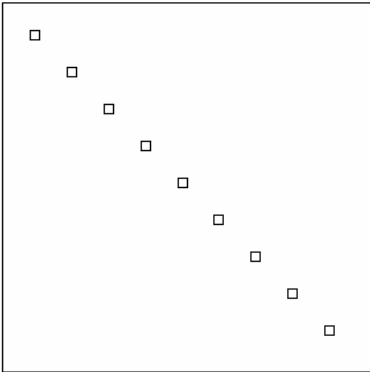


Figure 6.4: Geometry of Model 3.

The aim in constructing this model is to examine the position dependent accuracies and spatial resolutions of the algorithms.

6.2.4 Computer Model 4

The last model constructed in this study contains a square object with a 22.5 mm side length positioned at the middle of the model. Geometry of the model is given in Figure 6.5. Background conductivity is again assigned as 0.2 S/m. isotropic. Nineteen different anisotropic conductivity values were assigned to this square. Nine of these were for more conductive cases. These conductivity values are given in Table 6.4. The other nine simulations were for less conductive that is more resistive cases. These values are given in Table 6.5. Remaining one simulation was for the uniform case in which square object conductivity is assigned as 0.2 S/m in both directions.

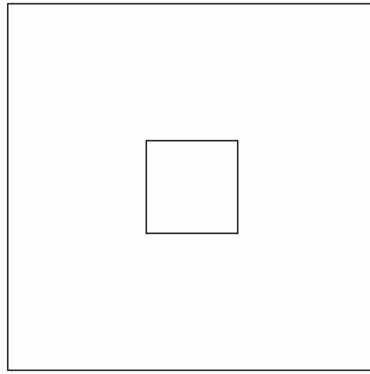


Figure 6.5: Geometry of Model 4.

Table 6.4: Conductivity values of inner square in model 4 for more conductive cases. Values are in S/m.

Experiment:	1	2	3	4	5	6	7	8	9
σ_{xx}	0.4	0.6	0.8	1	1.2	1.4	1.6	1.8	2
$\sigma_{xy} = \sigma_{yx}$	0	0	0	0	0	0	0	0	0
σ_{yy}	0.2	0.2	0.2	0.2	0.2	0.2	0.2	0.2	0.2

Table 6.5: Conductivity values of inner square in model 4 for less conductive cases. Values are in S/m.

Experiment:	1	2	3	4	5	6	7	8	9
σ_{xx}	0.1	0.067	0.05	0.04	0.033	0.028	0.025	0.022	0.02
$\sigma_{xx} = \sigma_{yy}$	0	0	0	0	0	0	0	0	0
σ_{yy}	0.2	0.2	0.2	0.2	0.2	0.2	0.2	0.2	0.2

These nineteen different cases were generated to investigate the reconstruction accuracy and linearity properties of the algorithms under changing conductivities.

6.3 Error Calculation

In order to evaluate the performance of the studied algorithms, the error in the reconstructed conductivity is calculated. In practice, the real conductivity is not known *a priori*, but in simulation studies, since the algorithms are fed with simulated data, the conductivity distribution is actually known.

For quantitative evaluation the performance of the proposed technique, the following error formula is used for reconstructed conductivity images in x and y directions.

$$\mathcal{E}_{\sigma_u} = \sqrt{\frac{1}{N} \sum_{j=1}^N \frac{(\sigma_{jt_u} - \sigma_{jr_u})^2}{\sigma_{jt_u}^2}} \times 100\% \quad (6.1)$$

where, u is anisotropic conductivity direction index which can be xx, xy, yx or yy, σ_{jt} and σ_{jr} are the true and the reconstructed conductivity values in any direction for the j^{th} element and N denotes the total number of pixels in the image. For isotropic regions, similar error calculation is also made. If xy and yx components of the anisotropic conductivity is modeled as zero, since the denominator of the equation in 6.1 will be zero, this equation will be meaningless. In this case, means of the reconstructed images for these components are added to the error tables.

6.4 Simulation of Measurement Noise

To evaluate the performance of the proposed algorithms in presence of noise, current density noise model of Scott *et al* [8] is employed as described by Birgöl *et al* [22]. In this model, Scott defined the signal-to-noise ratio (SNR_{MR}) as:

$$SNR_{MR} = \frac{A}{s_n} = \Psi_s \Delta x \Delta y \Delta z \sqrt{N \cdot T_s} M(x, y) \quad (6.2)$$

where A is the noise free pixel value magnitude of the corresponding MR image, s_n is the standard deviation of the complex image, Ψ_s is a system SNR, $\Delta x \Delta y \Delta z$ is the voxel volume, N is the total number of excitations, T_s is the total readout sampling time for one echo, and $M(x, y)$ is magnetization. Here, s_n is measured as the RMS noise in the magnitude image background. Scott gives the phase error probability density function in his study by

$$f_{\Theta}(\theta) = \frac{1}{2\pi} \exp(-a^2/2) + \frac{a \cos(\theta)}{2\sqrt{2\pi}} \exp(-a^2) \sin^2(\theta) / 2 \operatorname{erfc}(-a \cos(\theta) \sqrt{2}) \quad (6.3)$$

where, $a = \sqrt{2} SNR_{MR}$ and θ represents phase error. Here, it is important to note that in this noise model, the phase error and hence, the noise in \vec{B}_{MR} is independent of \vec{B}_{MR} . Therefore, the proportional noise in \vec{B}_{MR} and consequently in \vec{J}_{MR} is reduced for increased amount of current density.

In 1992, Scott *et al* reported an SNR measurement of 2T magnet as 30. A set of simulation study is achieved for SNR of 30 on the model 1 given in Figure 6.2. to test the proposed techniques under typical level. Also Birgöl *et al* reported an SNR level of 13 for 0.15 T METU EEE Magnetic Resonance System. Because of that SNR of 13 was also investigated on the same model.

6.5 Results of the Proposed Algorithms

In this part, reconstruction results of all algorithms explained in the previous chapters for the models given in part 6.2 will be given. The results are grouped under different computer models. For every model, results of five different reconstruction algorithms are given. Also, obtained results using experimental data is given in this part. Comments on the results will be given at the end of each model results.

6.5.1 Results for Computer Model 1

6.5.1.1 Reconstruction Using Anisotropic EPP Algorithm

In this part, reconstruction results for model 1 using anisotropic equipotential projection algorithm will be given. Figure 6.6 shows the results for noise free simulations at 35th iteration and Table 6.6 gives corresponding errors. Since the true values of x_y and y_x components of the conductivity is zero for the object, mean values of the reconstructed conductivities for these components are given in the table.

The same model was then reconstructed using noisy current density measurements having SNR values of 30 and 13. Results for SNR=30 and SNR=13 are given in Figure 6.7 and Figure 6.8, respectively. Corresponding errors for these reconstructions are also given Table 6.7 and 6.8, respectively.

In order to see the convergence behavior of the algorithm a convergence plot was generated. This plot is given in Figures 6.9.

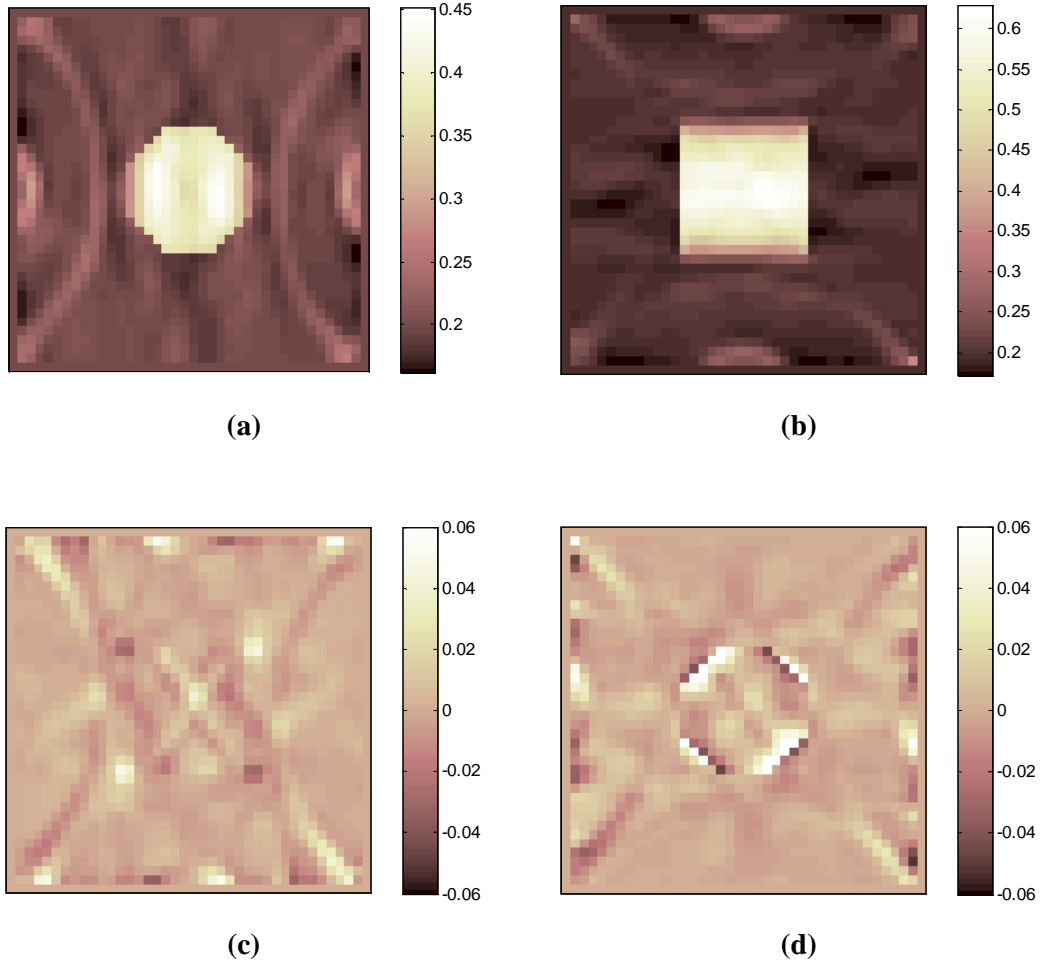


Figure 6.6: Reconstruction results for model 1 using anisotropic equipotential projection algorithm ($\text{SNR} = \infty$): (a) σ_{xx} , (b) σ_{yy} , (c) σ_{xy} and (d) σ_{yx} .

Table 6.6: Percentage errors of reconstructed images in Figure 6.6.

	$\varepsilon_{\sigma_{xx}}$ (%)	$\varepsilon_{\sigma_{yy}}$ (%)	σ_{xy} (Mean)	σ_{yx} (Mean)
Object	10.58	17.60	0.0013	0.0094
Background	8.65	8.51	-	-

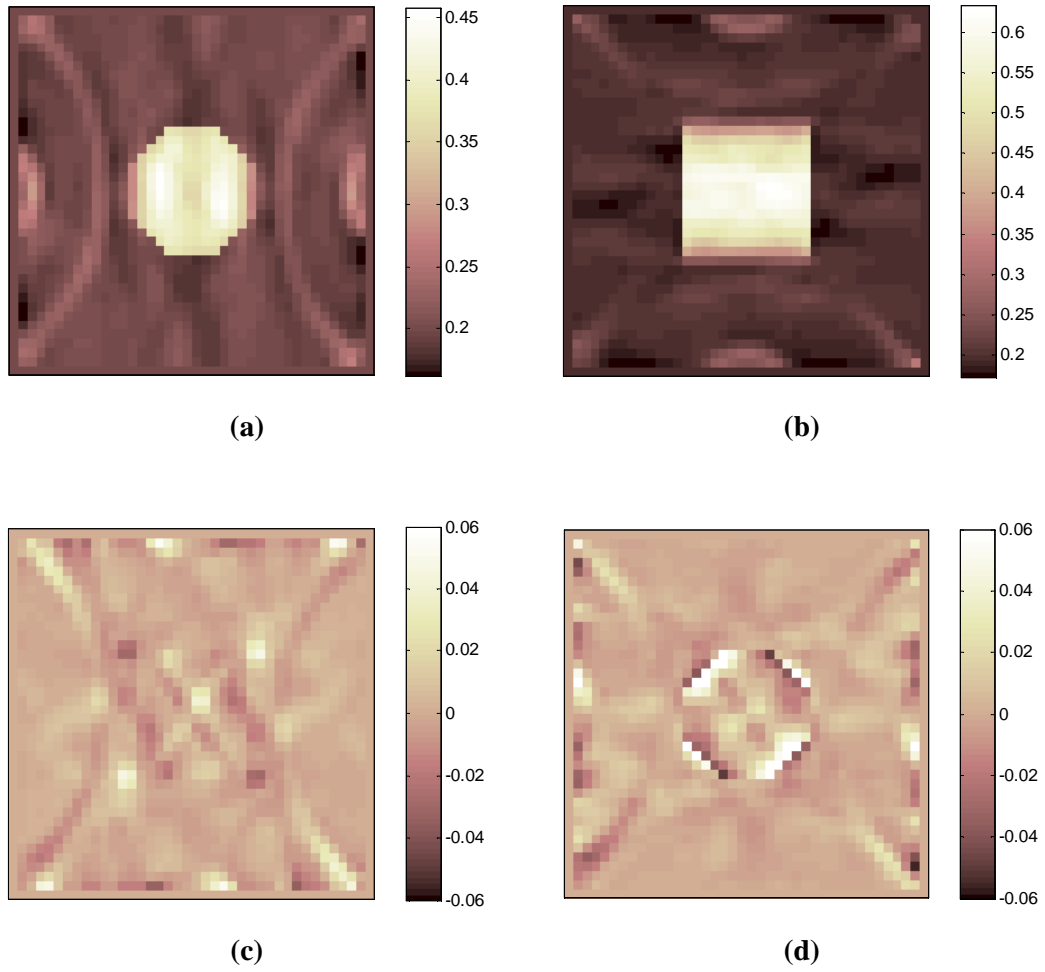


Figure 6.7: Reconstruction results for model 1 using anisotropic equipotential projection algorithm (SNR = 30): (a) σ_{xx} , (b) σ_{yy} , (c) σ_{xy} and (d) σ_{yy} .

Table 6.7: Percentage errors of reconstructed images in Figure 6.7.

	$\varepsilon_{\sigma_{xx}}$ (%)	$\varepsilon_{\sigma_{yy}}$ (%)	σ_{xy} (Mean)	σ_{yx} (Mean)
Object	10.68	18.02	0.0015	0.0062
Background	8.74	8.66	-	-

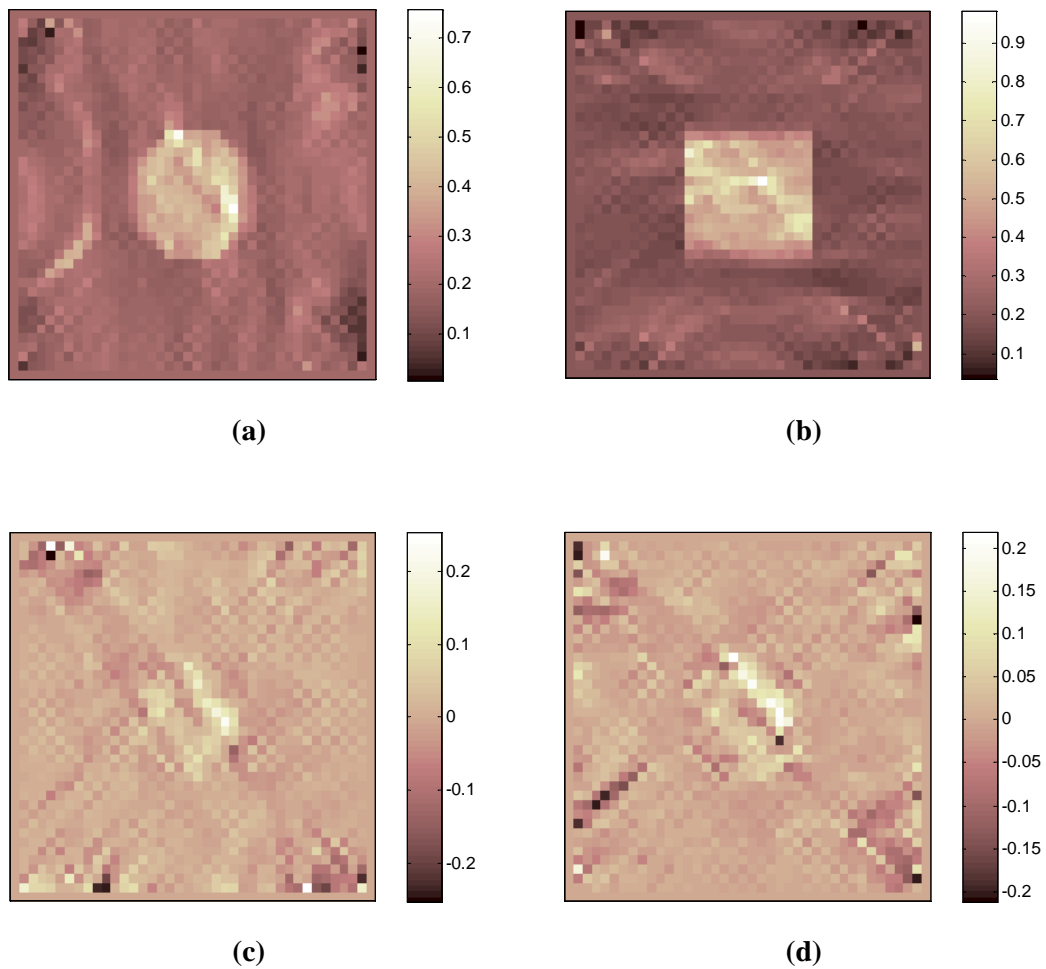


Figure 6.8: Reconstruction results for model 1 using anisotropic equipotential projection algorithm (SNR = 13): (a) σ_{xx} , (b) σ_{yy} , (c) σ_{xy} and (d) σ_{yx} .

Table 6.8: Percentage errors of reconstructed images in Figure 6.8.

	$\mathcal{E}_{\sigma_{xx}}$ (%)	$\mathcal{E}_{\sigma_{yy}}$ (%)	σ_{xy} (Mean)	σ_{yx} (Mean)
Object	19.83	23.89	0.066	0.087
Background	20.24	21.08	-	-

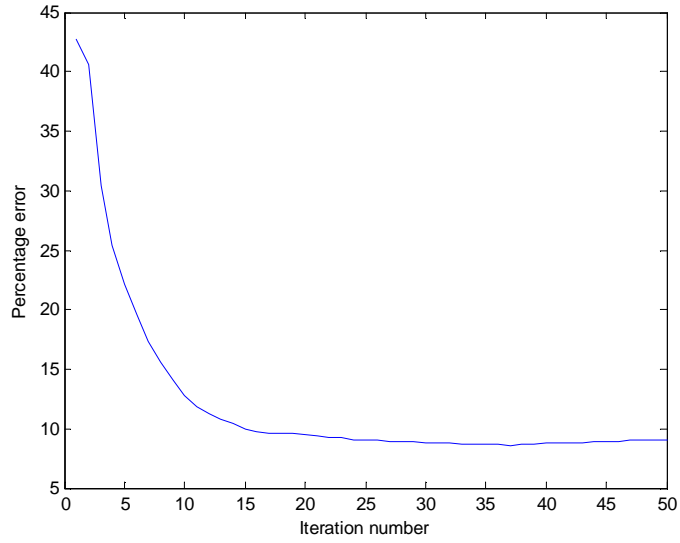


Figure 6.9: Convergence characteristic of the anisotropic EPP algorithm for noise free case.

6.5.1.2 Reconstruction Using Anisotropic J-Substitution Algorithm

In this part, reconstruction results of model 1 using anisotropic J-substitution algorithm will be given. Figure 6.10, 6.11 and 6.12 show the results for noise free, SNR=30 and SNR=13 cases, respectively and Table 6.9, 6.10 and 6.11 give corresponding errors.

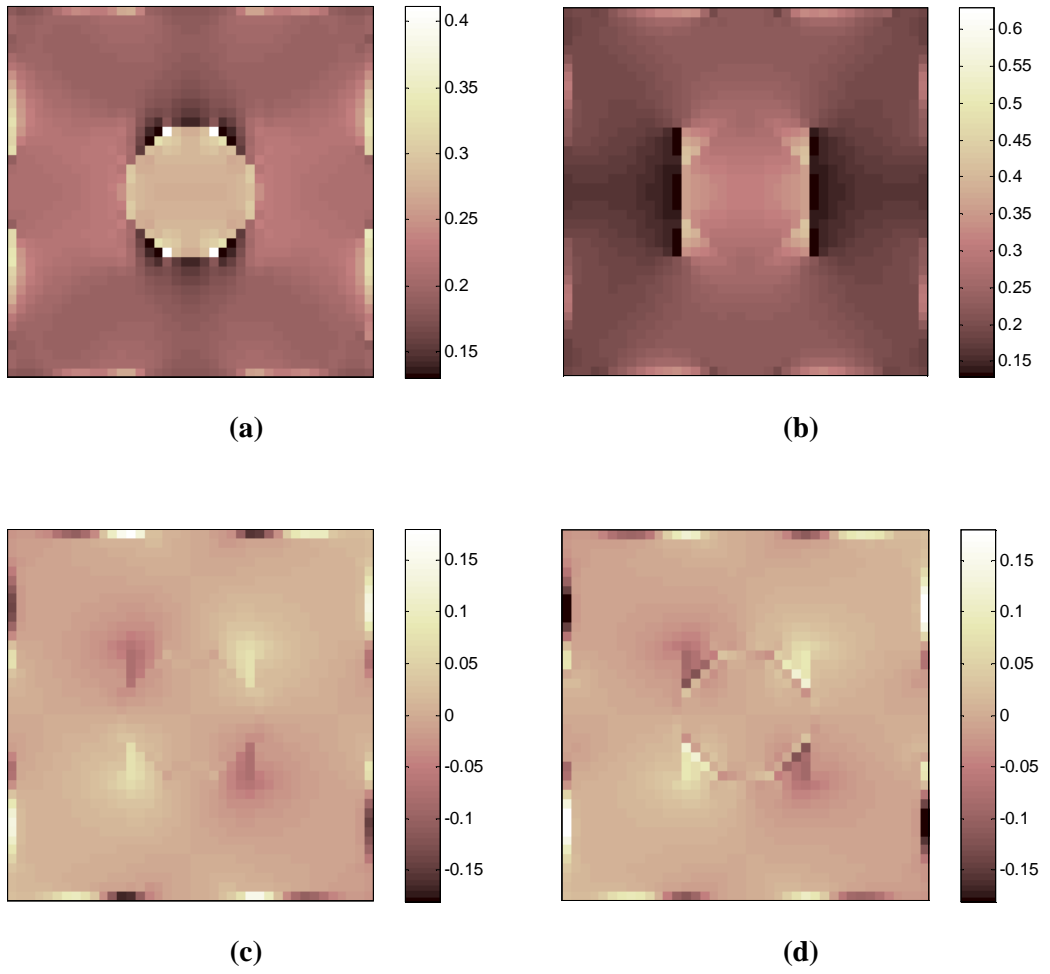


Figure 6.10: Reconstruction results for model 1 using anisotropic J-substitution algorithm ($\text{SNR} = \infty$): (a) σ_{xx} , (b) σ_{yy} , (c) σ_{xy} and (d) σ_{yx} .

Table 6.9: Percentage errors of reconstructed images in Figure 6.10.

	$\varepsilon_{\sigma_{xx}}$ (%)	$\varepsilon_{\sigma_{yy}}$ (%)	σ_{xy} (Mean)	σ_{yx} (Mean)
Object	28.89	46.82	-0.0059	-0.0068
Background	8.59	15.33	-	-

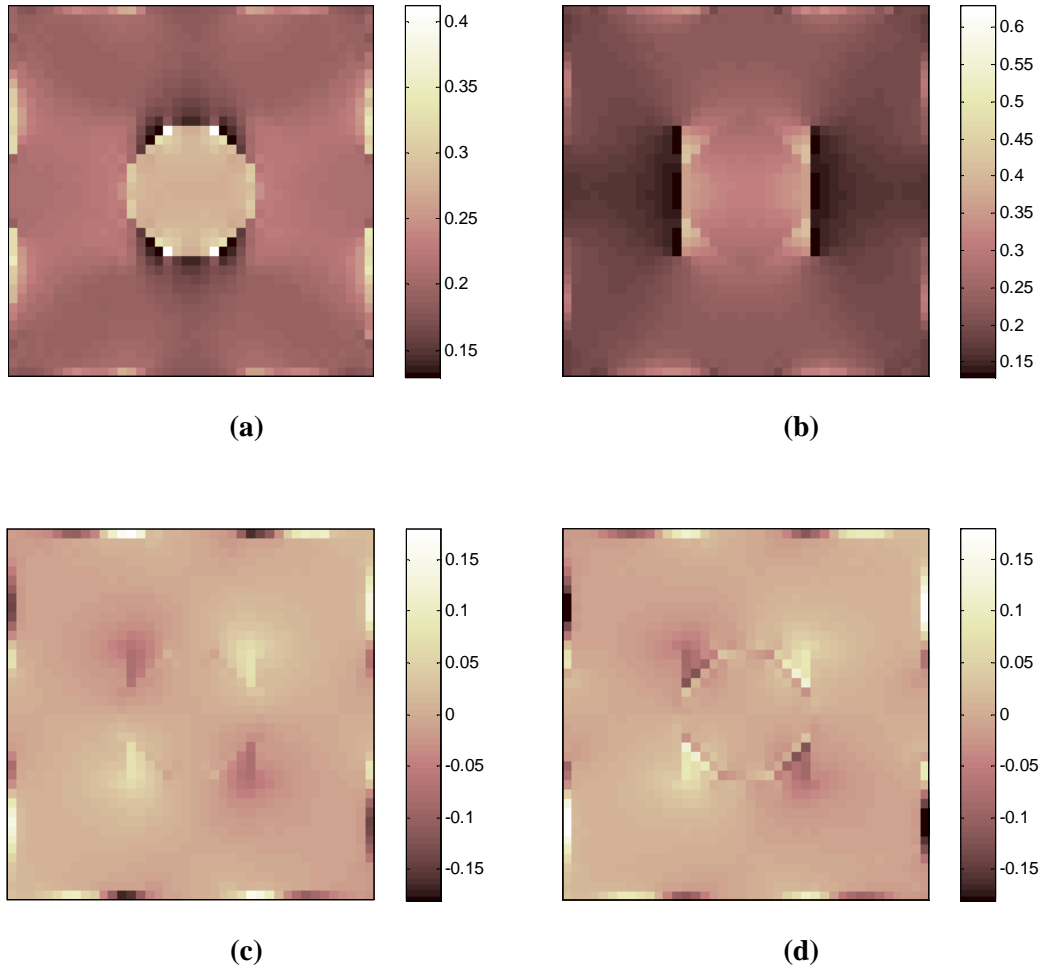


Figure 6.11: Reconstruction results for model 1 using anisotropic J-substitution algorithm (SNR = 30): (a) σ_{xx} , (b) σ_{yy} , (c) σ_{xy} and (d) σ_{yx} .

Table 6.10: Percentage errors of reconstructed images in Figure 6.11.

	$\varepsilon_{\sigma_{xx}}$ (%)	$\varepsilon_{\sigma_{yy}}$ (%)	σ_{xy} (Mean)	σ_{yx} (Mean)
Object	28.92	46.87	-0.0058	-0.0070
Background	8.61	15.34	-	-

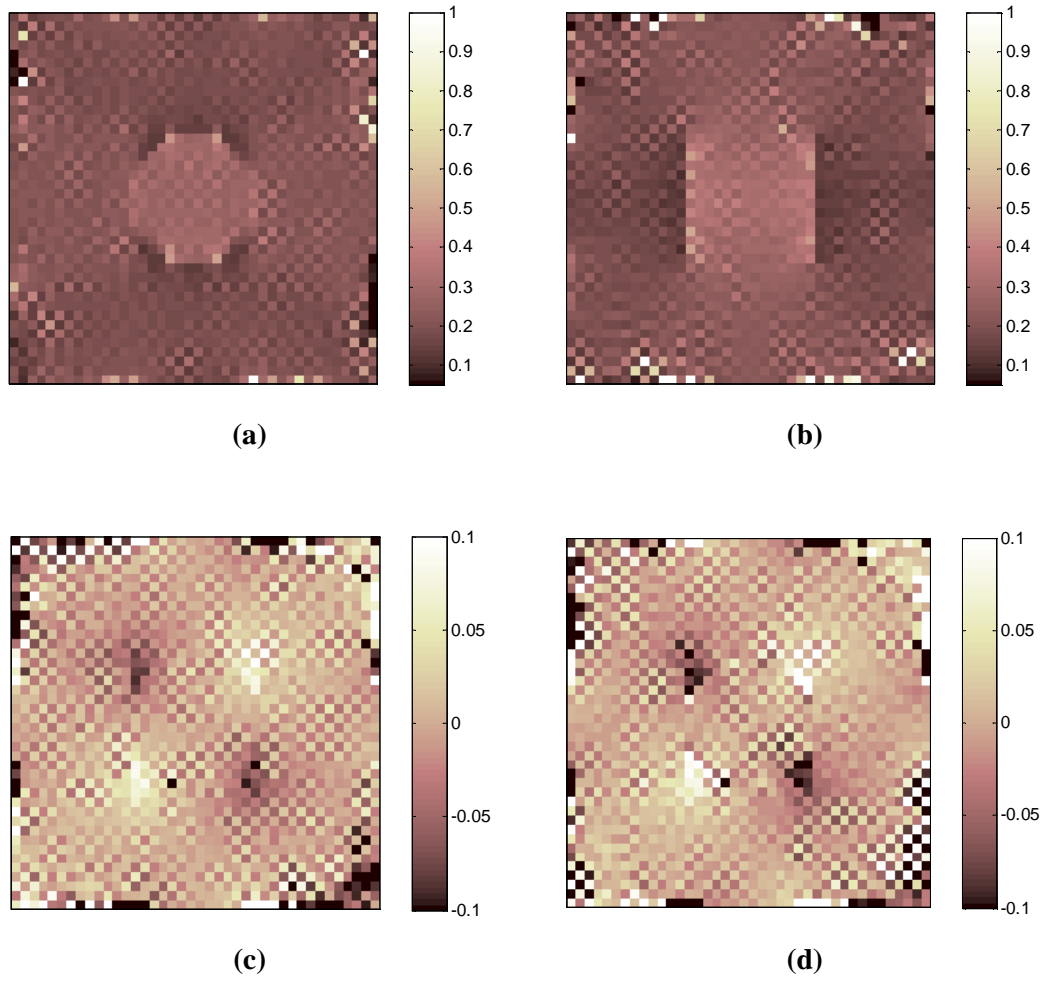


Figure 6.12: Reconstruction results for model 1 using anisotropic J-substitution algorithm (SNR = 13): (a) σ_{xx} , (b) σ_{yy} , (c) σ_{xy} and (d) σ_{yx} .

Table 6.11: Percentage errors of reconstructed images in Figure 6.12.

	$\mathcal{E}_{\sigma_{xx}}$ (%)	$\mathcal{E}_{\sigma_{yy}}$ (%)	σ_{xy} (Mean)	σ_{yx} (Mean)
Object	29.29	46.47	-0.042	0.038
Background	39.06	54.29	-	-

6.5.1.3 Reconstruction Using Anisotropic Hybrid J-Substitution Algorithm

In this part, reconstruction results of model 1 using anisotropic hybrid J-substitution algorithm will be given. Figure 6.13, 6.14 and 6.15 give the results for noise free, SNR=30 and SNR=13 cases, respectively and Table 6.12, 6.13 and 6.14 give corresponding errors.

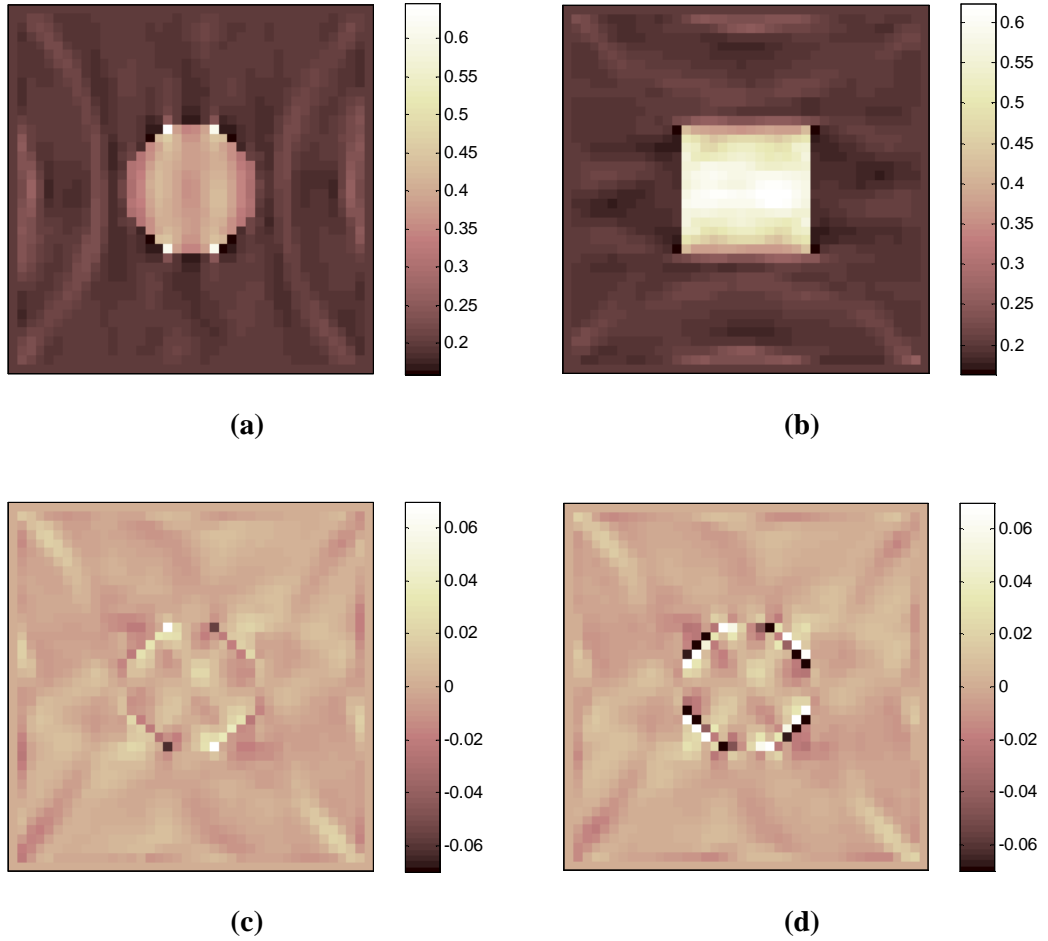


Figure 6.13: Reconstruction results for model 1 using anisotropic hybrid J-substitution algorithm (SNR = ∞): (a) σ_{xx} , (b) σ_{yy} , (c) σ_{xy} and (d) σ_{yx} .

Table 6.12: Percentage errors of reconstructed images in Figure 6.13.

	$\varepsilon_{\sigma_{xx}}$ (%)	$\varepsilon_{\sigma_{yy}}$ (%)	σ_{xy} (Mean)	σ_{yx} (Mean)
Object	10.15	17.43	0.0002	0.0002
Background	6.35	6.72	-	-

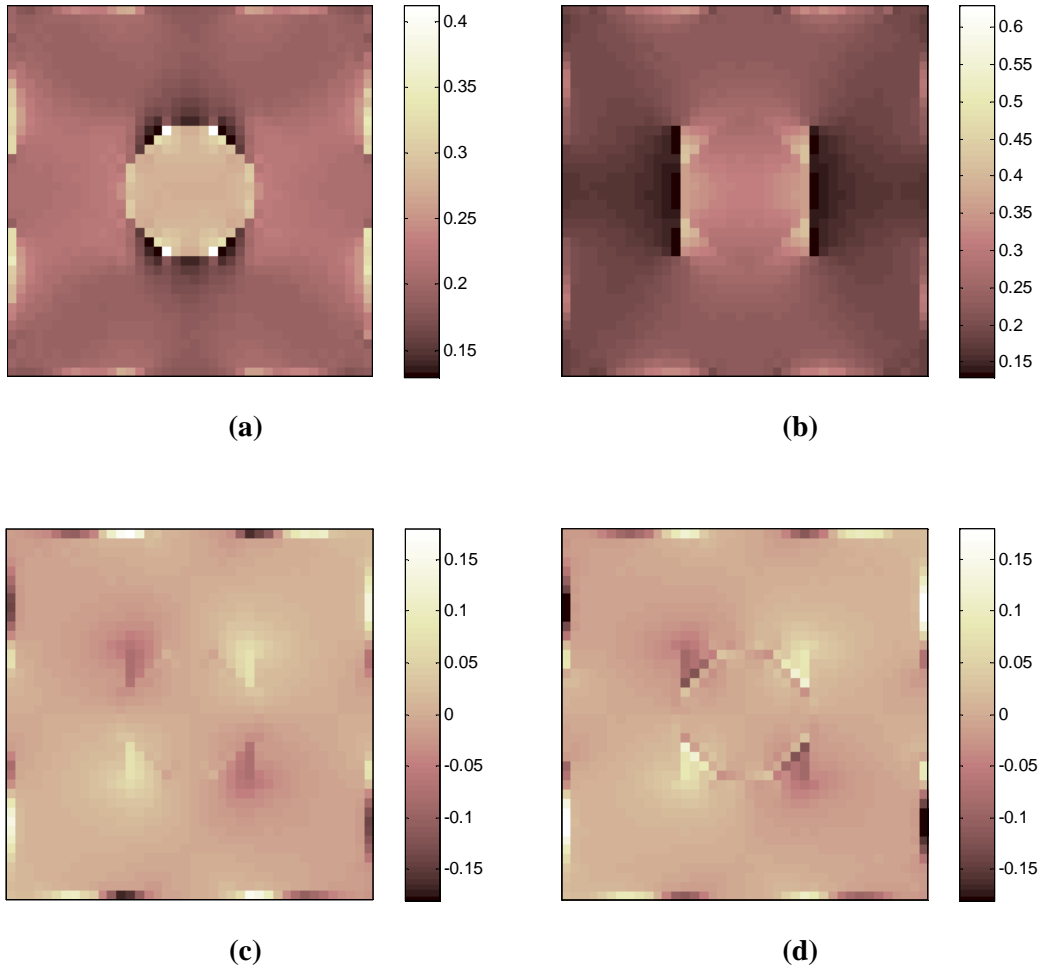


Figure 6.14: Reconstruction results for model 1 using anisotropic hybrid J-substitution algorithm (SNR = 30): (a) σ_{xx} , (b) σ_{yy} , (c) σ_{xy} and (d) σ_{yx} .

Table 6.13: Percentage errors of reconstructed images in Figure 6.14.

	$\mathcal{E}_{\sigma_{xx}}$ (%)	$\mathcal{E}_{\sigma_{yy}}$ (%)	σ_{xy} (Mean)	σ_{yx} (Mean)
Object	28.92	46.87	-0.0058	-0.0070
Background	8.61	15.34	-	-

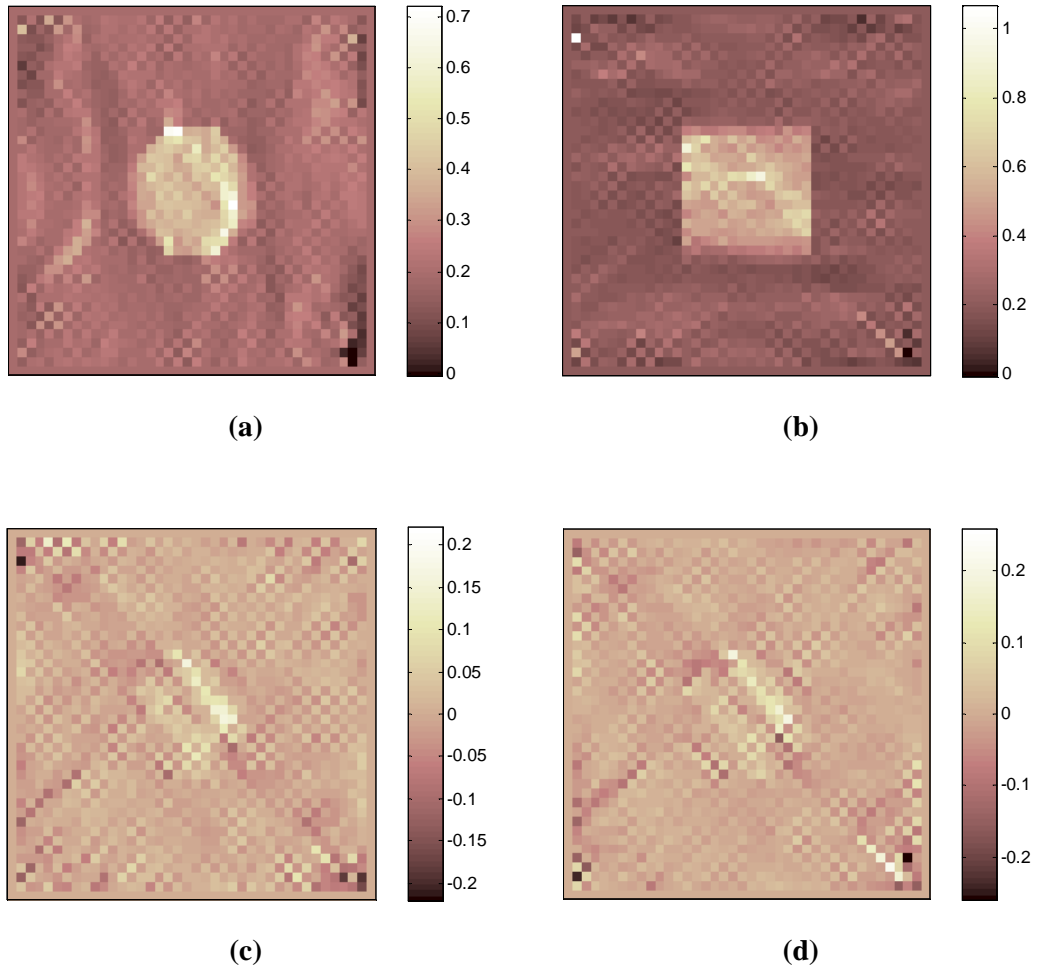


Figure 6.15: Reconstruction results for model 1 using anisotropic hybrid J-substitution algorithm (SNR = 13): (a) σ_{xx} , (b) σ_{yy} , (c) σ_{xy} and (d) σ_{yx} .

Table 6.14: Percentage errors of reconstructed images in Figure 6.15.

	$\varepsilon_{\sigma_{xx}}$ (%)	$\varepsilon_{\sigma_{yy}}$ (%)	σ_{xy} (Mean)	σ_{yx} (Mean)
Object	22.30	22.42	0.094	0.097
Background	22.66	26.84	-	-

6.5.1.4 Reconstruction Using Anisotropic Harmonic B_z Algorithm

In this part, reconstruction results of model 1 using anisotropic Harmonic B_z algorithm will be given. Figure 6.16, 6.17 and 6.18 give the results for noise free, SNR=30 and SNR=13 cases, respectively and Table 6.15, 6.16 and 6.17 give corresponding errors.

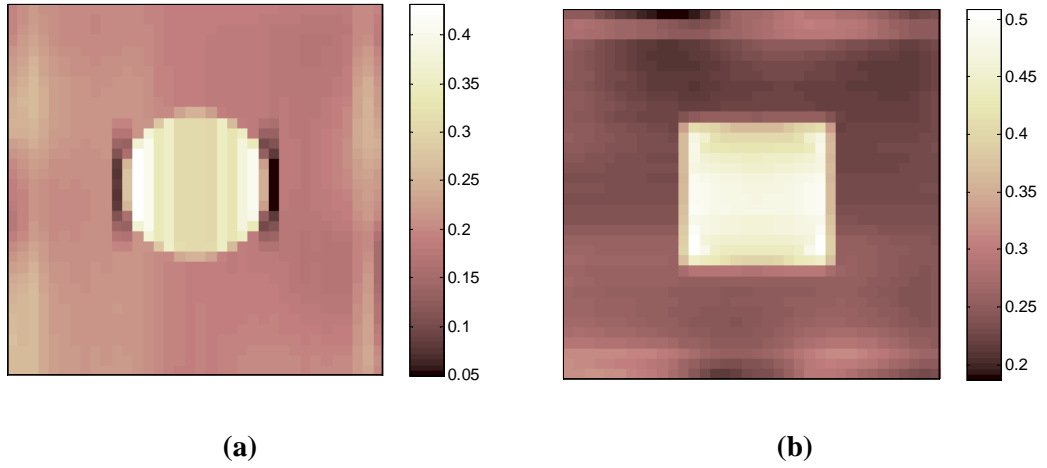


Figure 6.16: Reconstruction results for model 1 using anisotropic Harmonic B_z algorithm (SNR = ∞): (a) σ_{xx} , (b) σ_{yy} .

Table 6.15: Percentage errors of reconstructed images in Figure 6.16.

	$\mathcal{E}_{\sigma_{xx}}$ (%)	$\mathcal{E}_{\sigma_{yy}}$ (%)
Object	18.63	29.19
Background	15.77	27.87

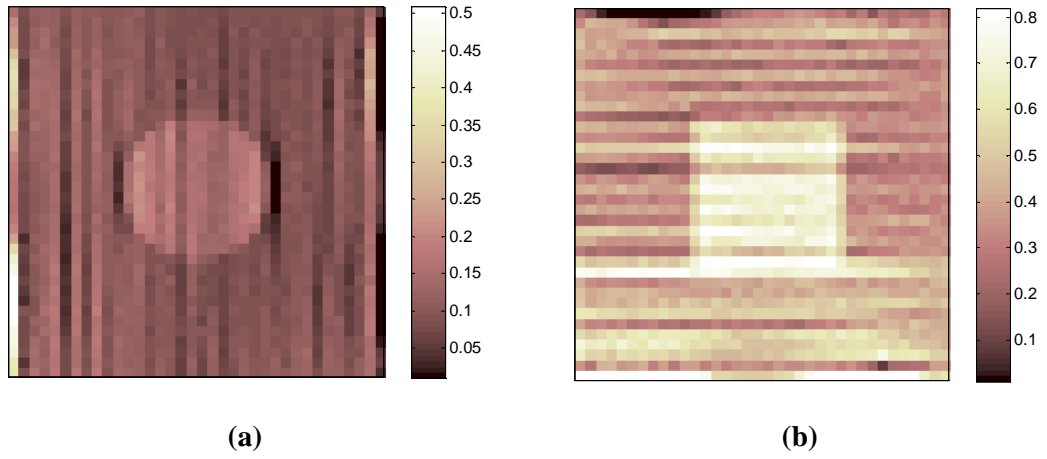


Figure 6.17: Reconstruction results for model 1 using anisotropic Harmonic B_z algorithm (SNR = 30): (a) σ_{xx} , (b) σ_{yy} .

Table 6.16: Percentage errors of reconstructed images in Figure 6.17.

	$\varepsilon_{\sigma_{xx}}$ (%)	$\varepsilon_{\sigma_{yy}}$ (%)
Object	52.03	40.83
Background	54.73	38.12

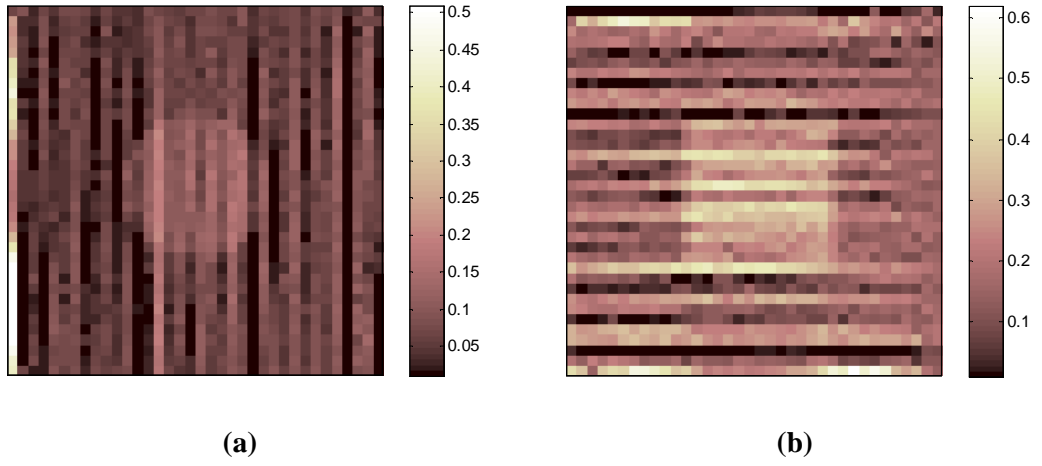


Figure 6.18: Reconstruction results for model 1 using anisotropic Harmonic B_z algorithm (SNR = 13): (a) σ_{xx} , (b) σ_{yy} .

Table 6.17: Percentage errors of reconstructed images in Figure 6.18.

	$\varepsilon_{\sigma_{xx}}$ (%)	$\varepsilon_{\sigma_{yy}}$ (%)
Object	71.51	61.78
Background	75.65	66.44

6.5.1.5 Reconstruction Using Anisotropic Sensitivity Algorithm

Finally, in this part, reconstruction results of model 1 using anisotropic Sensitivity algorithm will be given. Figure 6.19, 6.20 and 6.21 give the results for noise free, SNR=30 and SNR=13 cases, respectively and Table 6.18, 6.19 and 6.20 give corresponding errors.

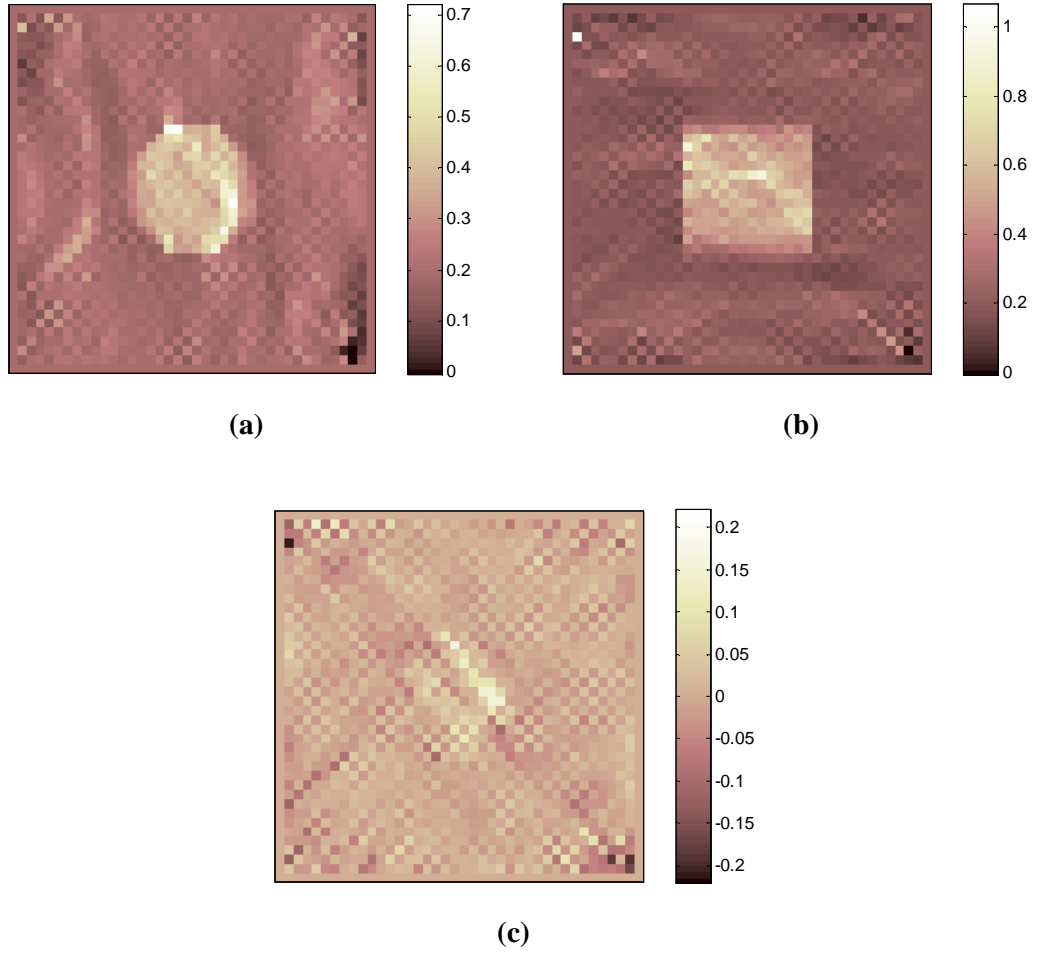


Figure 6.19: Reconstruction results for model 1 using anisotropic Sensitivity algorithm (SNR = ∞): (a) σ_{xx} , (b) σ_{yy} , (c) $\sigma_{xy} - \sigma_{yx}$.

Table 6.18: Percentage errors of reconstructed images in Figure 6.19.

	$\epsilon_{\sigma_{xx}}$ (%)	$\epsilon_{\sigma_{yy}}$ (%)	$\sigma_{xy} - \sigma_{yx}$ (Mean)
Object	22.62	34.84	0.0047
Background	9.82	10.69	-0.0003

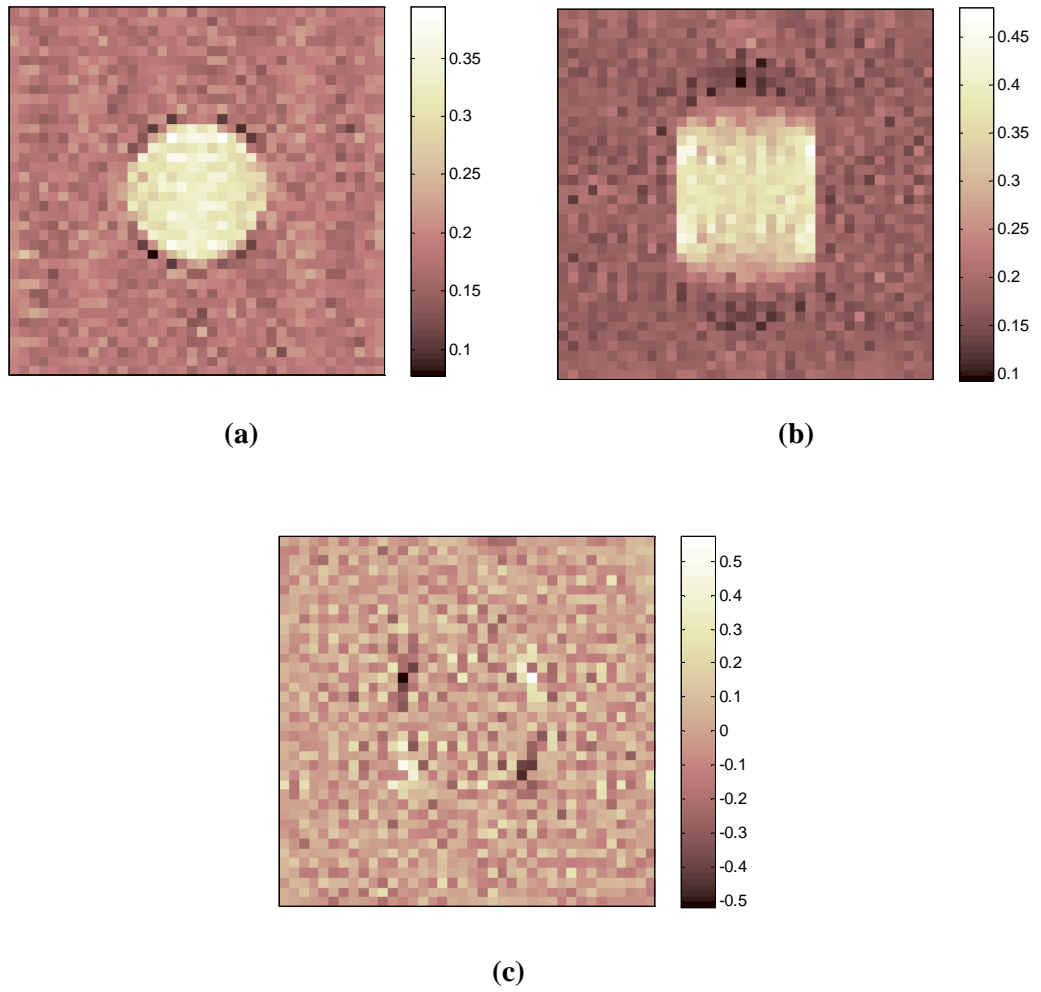


Figure 6.20: Reconstruction results for model 1 using anisotropic Sensitivity algorithm (SNR = 30): (a) σ_{xx} , (b) σ_{yy} , (c) $\sigma_{xy} - \sigma_{yx}$.

Table 6.19: Percentage errors of reconstructed images in Figure 6.20.

	$\varepsilon_{\sigma_{xx}}$ (%)	$\varepsilon_{\sigma_{yy}}$ (%)	$\sigma_{xy} - \sigma_{yx}$ (Mean)
Object	26.68	40.94	-0.0051
Background	13.26	15.81	-0.0009

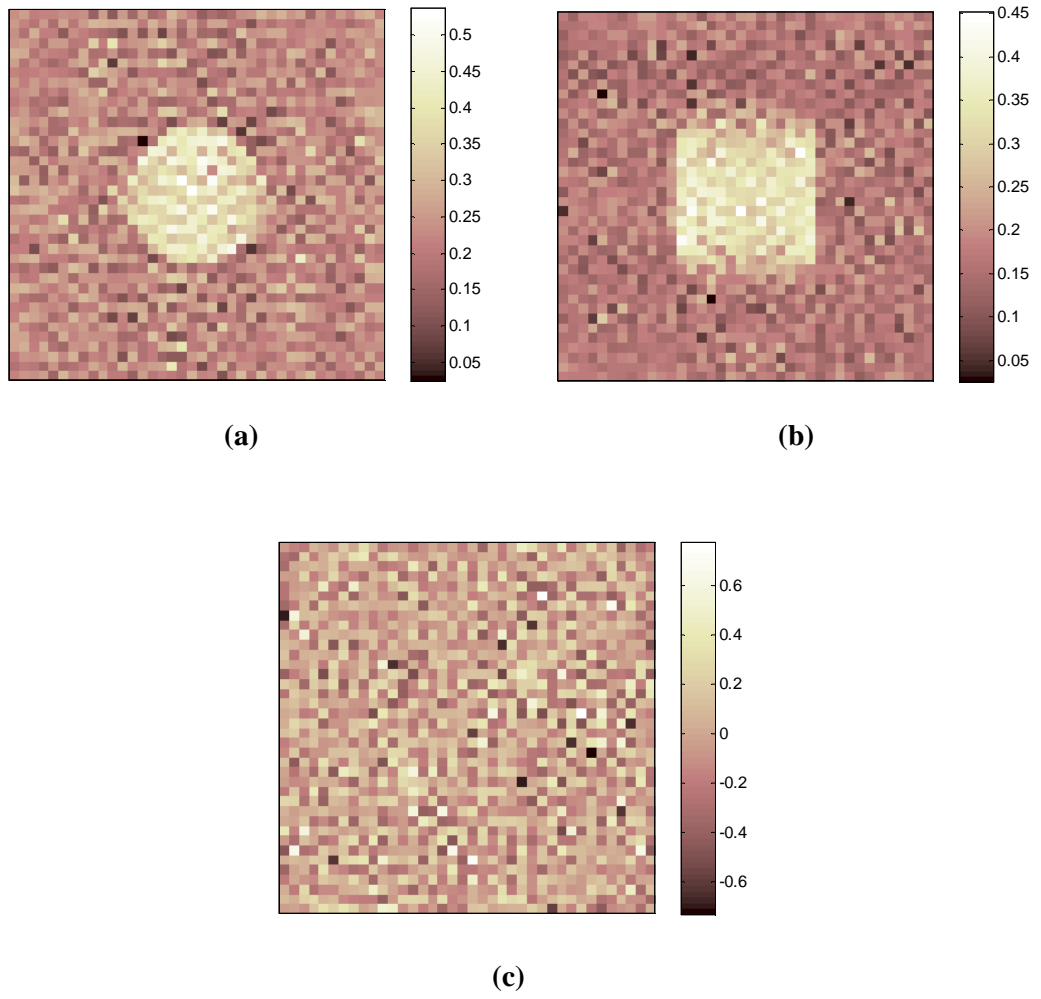


Figure 6.21: Reconstruction results for model 1 using anisotropic Sensitivity algorithm (SNR = 13): (a) σ_{xx} , (b) σ_{yy} , (c) $\sigma_{xy} - \sigma_{yx}$.

Table 6.20: Percentage errors of reconstructed images in Figure 6.21.

	$\varepsilon_{\sigma_{xx}}$ (%)	$\varepsilon_{\sigma_{yy}}$ (%)	$\sigma_{xy} - \sigma_{yx}$ (Mean)
Object	28.97	46.47	0.0373
Background	30.58	26.66	0.0409

6.5.1.6 Comparisons for Model 1

When the reconstruction algorithms are first evaluated for their reconstruction accuracies, it is seen that, all of the algorithms except anisotropic J-substitution algorithm show quite similar and good performances. But anisotropic J-substitution algorithm reconstructs object conductivities with less accuracy. Another drawback of the anisotropic J-substitution algorithm is its reconstruction time. One iteration of that algorithm takes about 5 minutes in an Intel Core 2 Duo E8400 CPU at 3 GHz and 4 GB of RAM. Therefore, it can be said that anisotropic J-substitution algorithm reconstructs conductivity images with poor accuracy and long time consumption. Long time consumption is also valid for anisotropic Harmonic B_z algorithm. It also takes about 5 minutes on the same computer.

When the noise performances of the algorithms are compared, it is seen that anisotropic J-substitution algorithm has again the poorest performance. Harmonic B_z algorithm is also weak against noisy data since, Harmonic B_z algorithm uses second derivative of noisy data. Other three algorithms show quite similar performances.

6.5.2 Results for Computer Model 2

In this part of the study, FWHM values of reconstructed impulsive objects in model 2 were calculated. Since the impulsive object has an impulsive conductivity in x direction and impulsive resistivity in y direction, two separate plots were prepared for these directions. Figure 6.25 and 6.26 give the FWHM plot for the impulsive conductor in x-direction for current density based and magnetic flux density based algorithms. Similarly, Figure 6.27 and 6.28 give the FWHM plot for the impulsive resistive in y direction. In Figure 6.17, since two impulsive conductor objects reconstructed using anisotropic EPP algorithm can not be distinguishable when the distance between objects is 2.25 mm, FWHM value for this case is not added to the figure. Reconstructed images, using anisotropic EPP algorithm when the distance between the objects is 2.25 mm, are given in Figure 6.22.

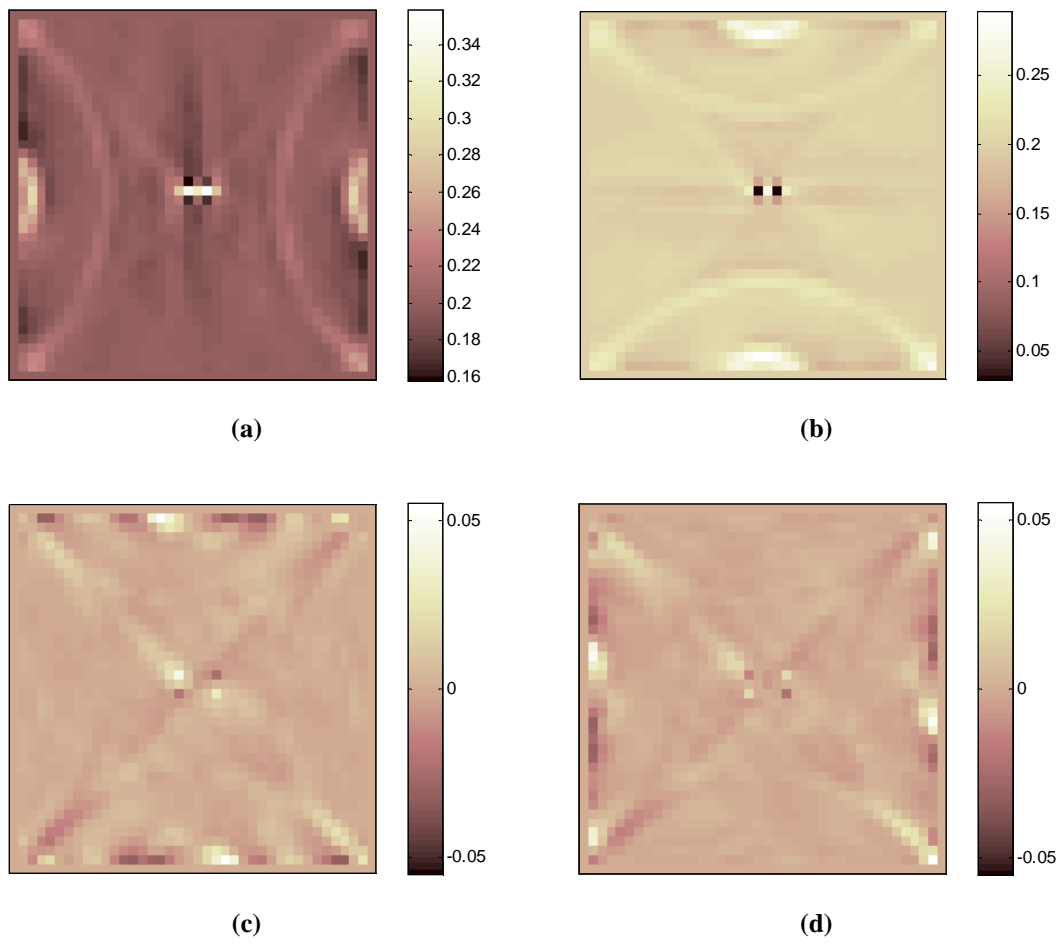


Figure 6.22: Reconstruction results for model 2 using anisotropic equipotential projection algorithm ($\text{SNR} = \infty$): (a) σ_{xx} , (b) σ_{yy} , (c) σ_{xy} and (d) σ_{yy} .

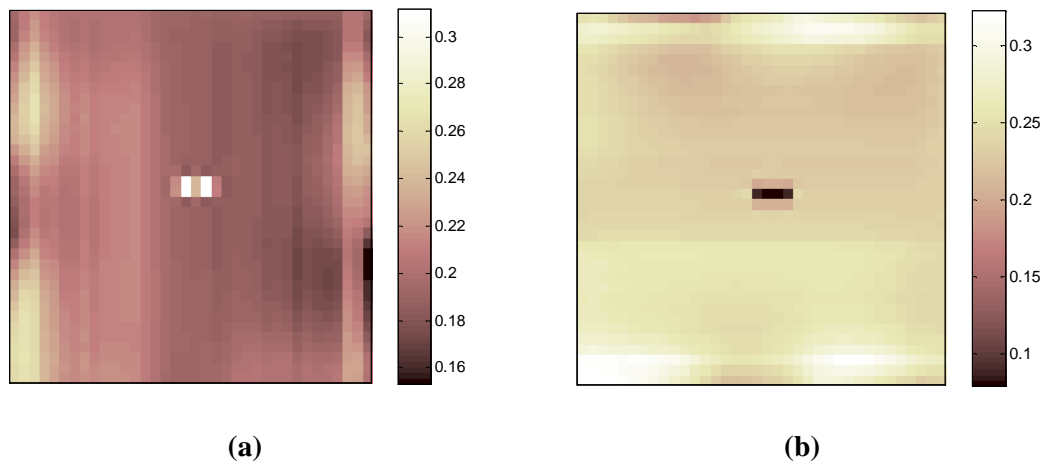


Figure 6.23: Reconstruction results for model 2 using anisotropic Harmonic B_z algorithm (SNR = ∞): (a) σ_{xx} , (b) σ_{yy} .

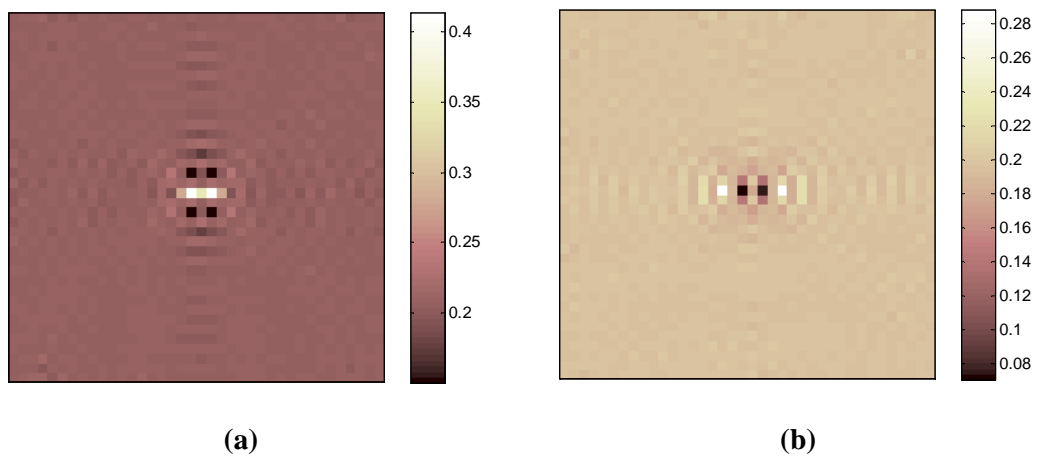


Figure 6.24: Reconstruction results for model 2 using anisotropic Sensitivity algorithm (SNR = ∞): (a) σ_{xx} , (b) σ_{yy} .

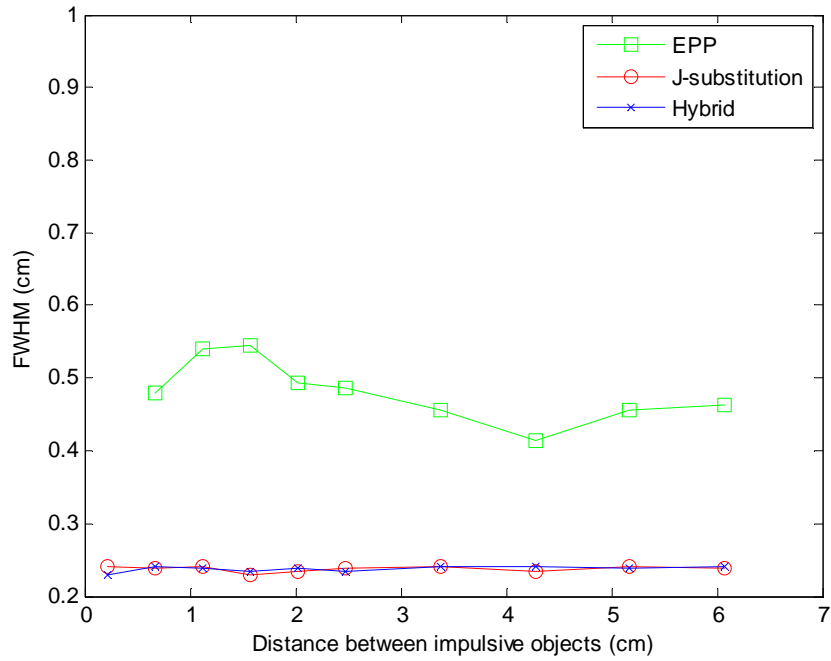


Figure 6.25: FWHM plot for the x-directed conductivity component of model 2 for current density based algorithms.

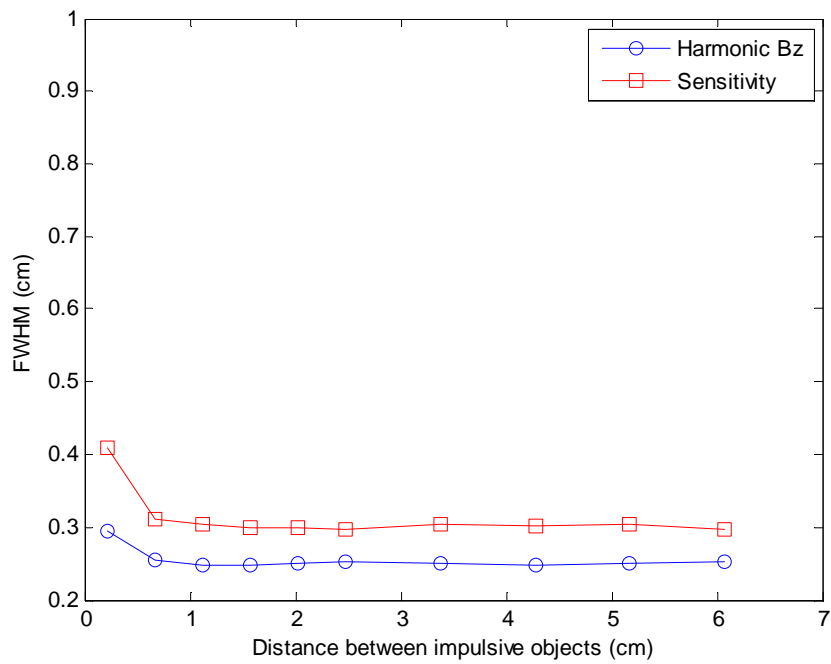


Figure 6.26: FWHM plot for the x-directed conductivity component of model 2 for magnetic flux density based algorithms.

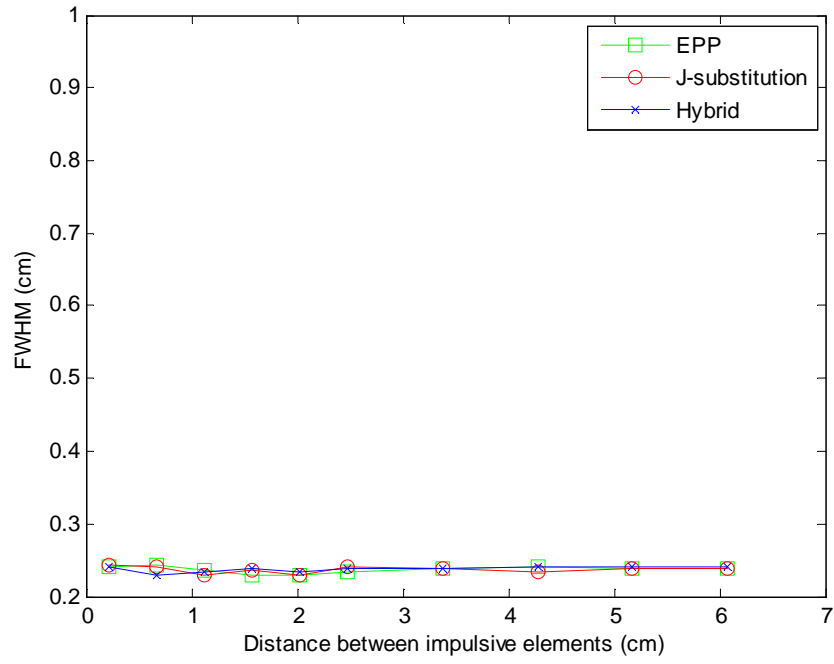


Figure 6.27: FWHM plot for the y-directed conductivity component of model 2 for current density based algorithms.

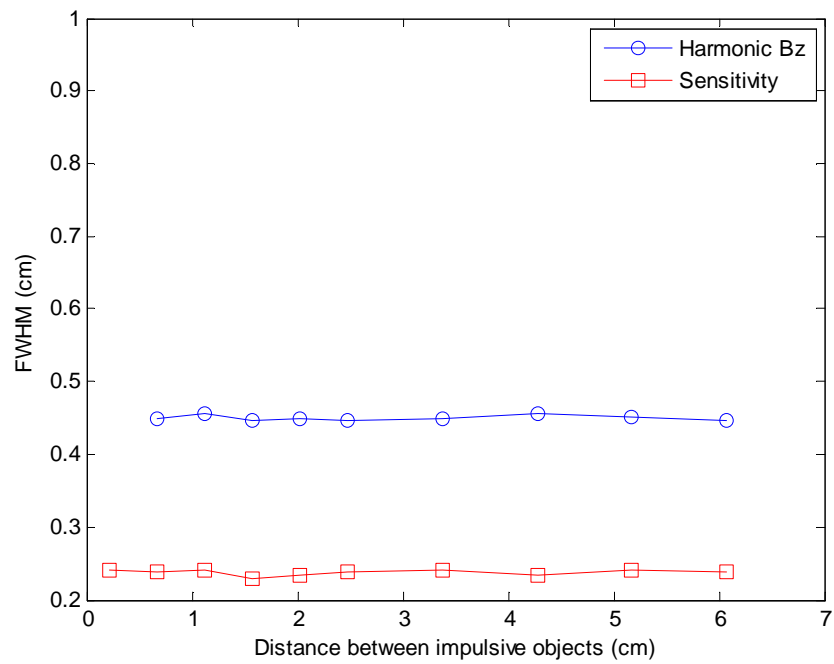


Figure 6.28: FWHM plot for the y-directed conductivity component of model 2 for magnetic flux density based algorithms.

6.5.2.1 Comparisons for Model 2

As seen from Figure 6.22, equipotential projection algorithm has a point spread function (PSF) which is about two times the theoretical value (pixel side length), at every point of the imaging slice in case of a high conductivity value in x-direction. This means that this algorithm can not distinguish the objects when the distance between them is less than one pixel side length of the imaging grid. But, this is not the case in y-direction. In that direction, EPP algorithm and the other algorithms have a FWHM value which is almost the same as the theoretical value. J-substitution and hybrid J-substitution algorithms have these value also in x-direction.

The reason behind this situation is probably that; when the conductivity in x direction is high and conductivity in y direction is low for an object, current flows in x direction inside this object. Therefore, equipotential lines are forced to be almost in y direction in the object and also very few equipotential lines pass from the left and the right sides of the object. Since anisotropic EPP algorithm constructs equipotential lines first in order to obtain potential field and sparse equipotential lines causes the potential field to be wrong, potential field at the left and right boundaries of this kind of object will be erroneous. Because of that, reconstructed conductivity values at that regions will be poor.

It is important to note that anisotropic Harmonic B_z algorithm could not distinguish the impulsive objects in y direction when the distance between them is 0.225 cm. Its behavior is similar to EPP algorithm's behavior in x direction.

6.5.3 Results for Computer Model 3

6.5.3.1 Reconstruction Using Anisotropic EPP Algorithm

This part covers the reconstruction results of anisotropic equipotential projection algorithm for model 3. Figure 6.29 shows the results for noise free simulations.

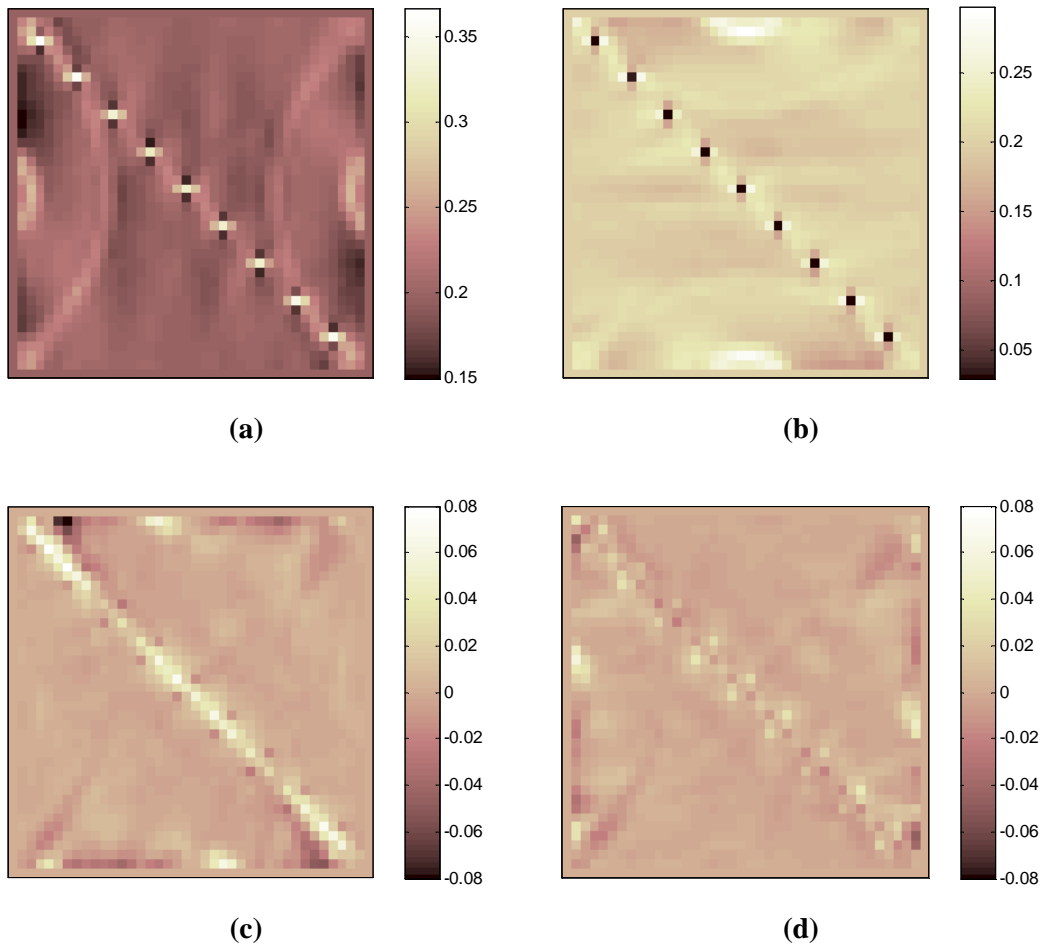


Figure 6.29: Reconstruction results for model 3 using anisotropic equipotential projection algorithm (SNR = ∞): (a) σ_{xx} , (b) σ_{yy} , (c) σ_{xy} and (d) σ_{yy} .

6.5.3.2 Reconstruction Using Anisotropic J-Substitution Algorithm

This part covers the reconstruction results of anisotropic J-substitution algorithm for model 3. Figure 6.30 shows the results for noise free simulations.

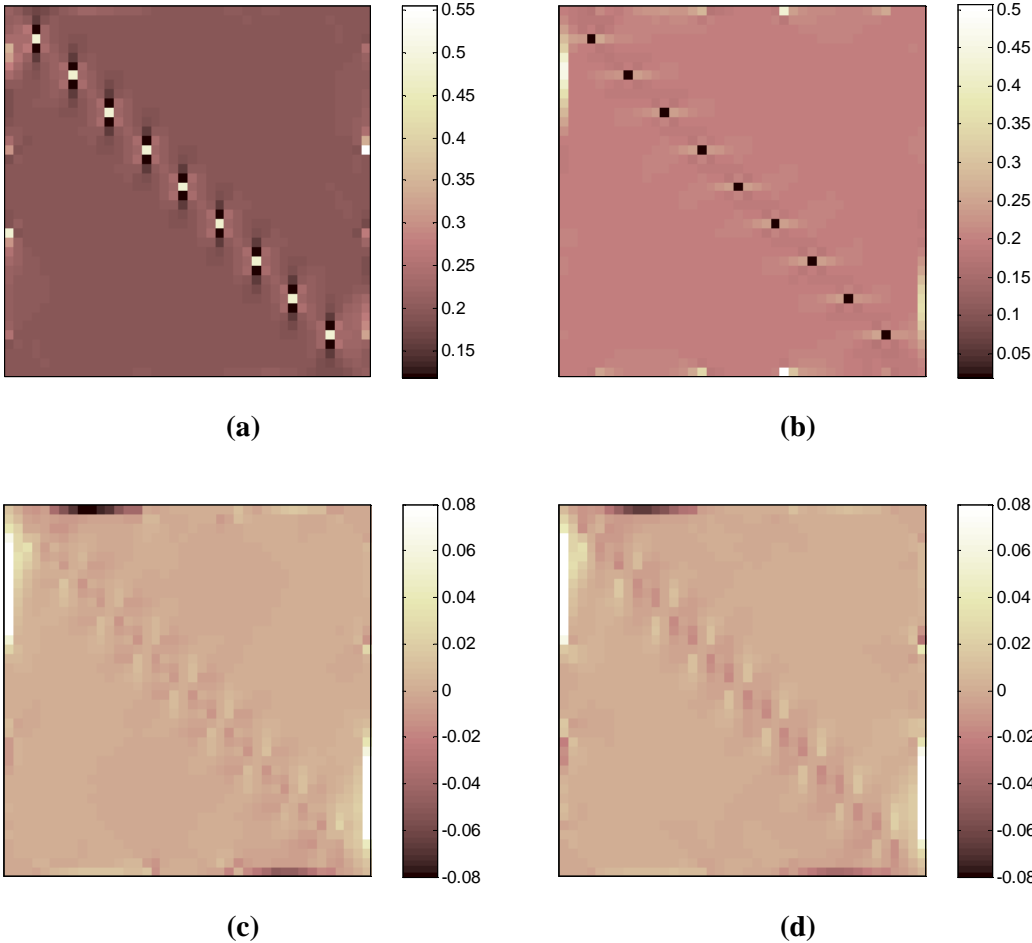


Figure 6.30: Reconstruction results for model 3 using anisotropic J-substitution algorithm ($\text{SNR} = \infty$): (a) σ_{xx} , (b) σ_{yy} , (c) σ_{xy} and (d) σ_{yy} .

6.5.3.3 Reconstruction Using Anisotropic Hybrid J-Substitution Algorithm

In this part, reconstruction results of anisotropic hybrid J-substitution algorithm for model 3 are given. Figure 6.31 shows the results for noise free simulations.

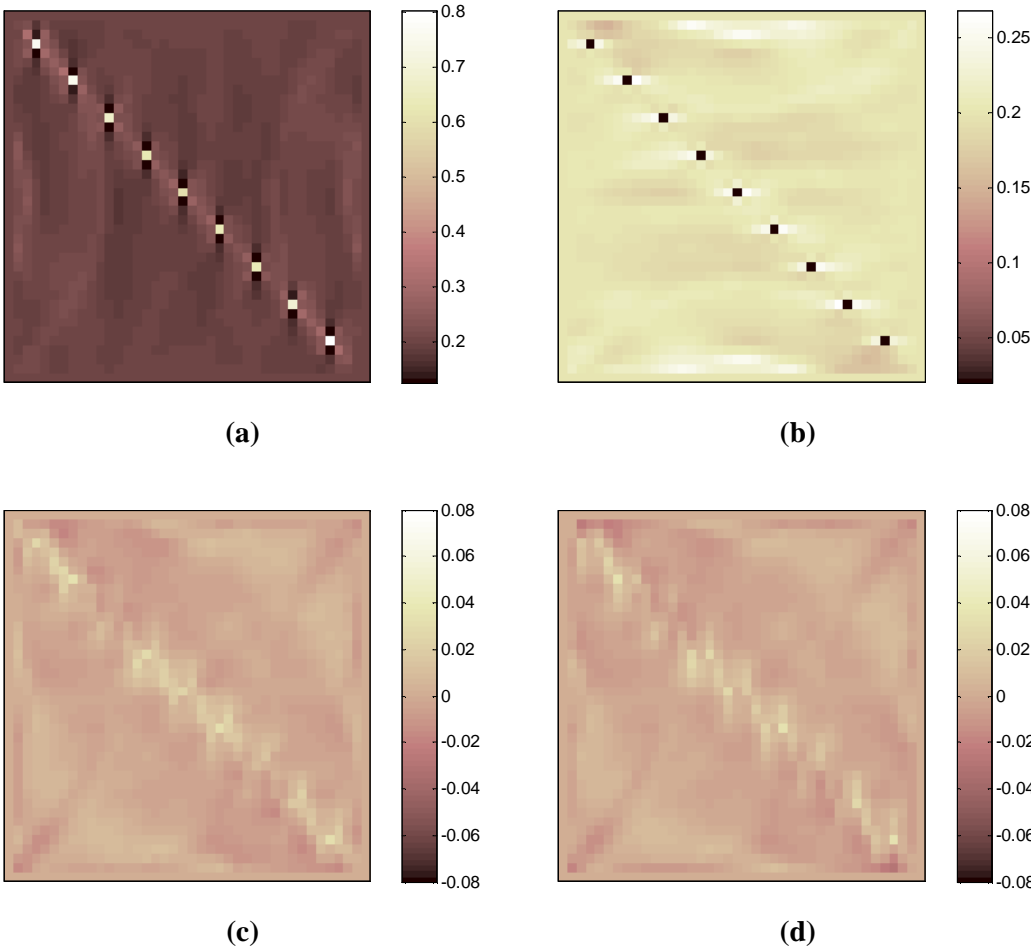


Figure 6.31: Reconstruction results for model 3 using anisotropic hybrid J-substitution algorithm ($\text{SNR} = \infty$): (a) σ_{xx} , (b) σ_{yy} , (c) σ_{xy} and (d) σ_{yy} .

6.5.3.4 Reconstruction Using Anisotropic Harmonic B_z Algorithm

In this part, reconstruction results of anisotropic Harmonic B_z algorithm for model 3 are given. Figure 6.32 shows the results for noise free simulations.

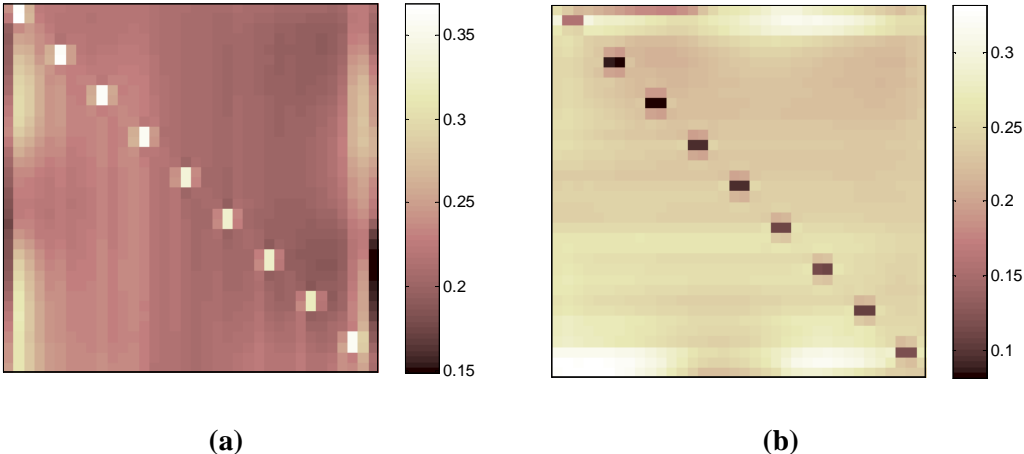


Figure 6.32: Reconstruction results for model 3 using anisotropic Harmonic B_z algorithm ($\text{SNR} = \infty$): (a) σ_{xx} , (b) σ_{yy} .

6.5.3.5 Reconstruction Using Anisotropic Sensitivity Algorithm

In this part, reconstruction results of anisotropic Sensitivity algorithm for model 3 are given. Figure 6.33 shows the results for noise free simulations.

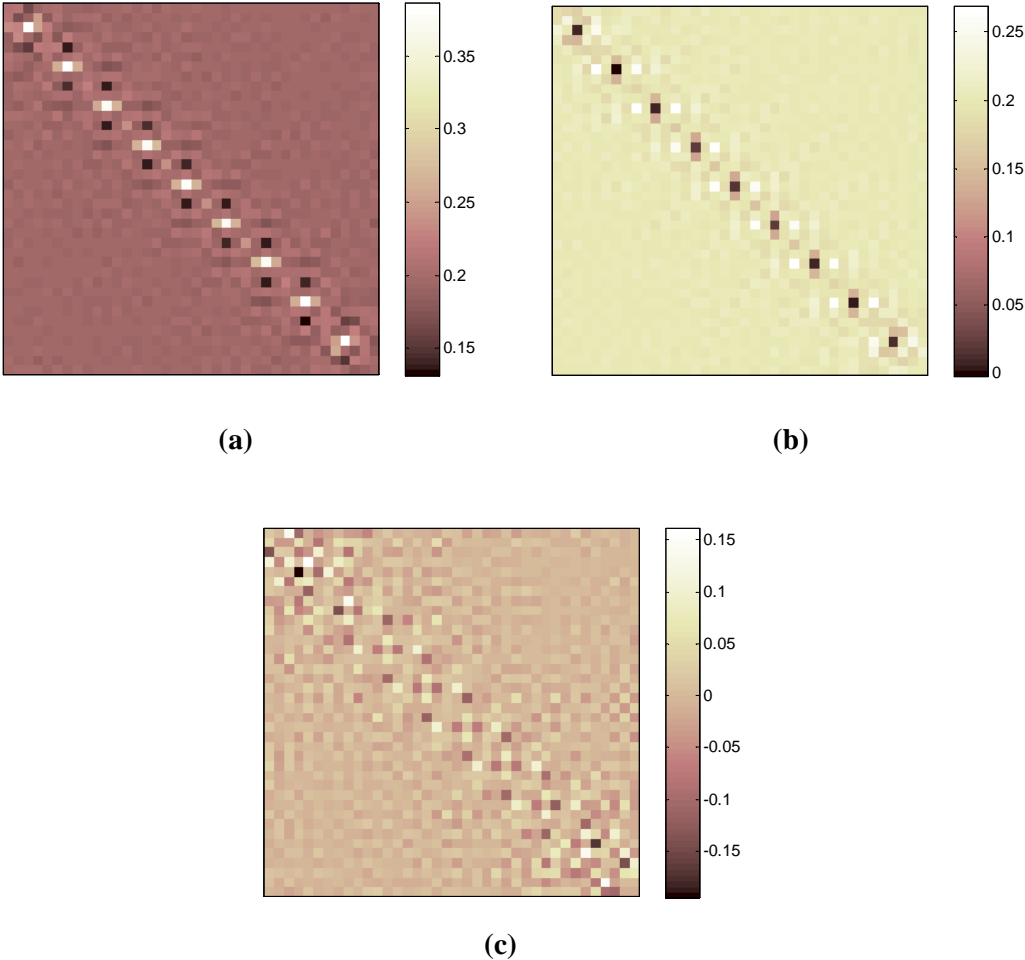


Figure 6.33: Reconstruction results for model 3 using anisotropic Sensitivity algorithm ($\text{SNR} = \infty$): (a) σ_{xx} , (b) σ_{yy} , (c) $\sigma_{xy} - \sigma_{yx}$.

6.5.3.6 Comparisons for Model 3

Model 3 was prepared to investigate the position dependent accuracy and spatial resolution properties of the algorithms. Therefore, nine impulsive objects whose x-directed and y-directed conductivities are respectively ten times more conductive and ten times less conductive than the background were placed in the model. When the reconstruction results given in figures are reviewed, it is seen that all five algorithms can reconstruct nine impulse object conductivities in both directions independent of position. Anisotropic EPP algorithm results again show a background artifact caused from equipotential lines as in the previous models. Hybrid J-substitution algorithm removes these artifacts to some extent and increases the background conductivity reconstruction accuracy. Furthermore, hybrid J-substitution algorithm increases the reconstruction accuracies of the impulsive elements' conductivities. In case of anisotropic Sensitivity algorithm, since the theory of the algorithm is constructed on small conductivity change assumption, nine impulsive objects cause some artifacts at their neighboring pixels. In case of spatial resolution, it can be said that all five algorithms have position independent spatial resolution.

6.5.4 Results for Computer Model 4

As explained previously, model 4 contains a square object having nineteen different anisotropic conductivities at nineteen different cases. Since the aim of this model is to explore the linearity properties of the algorithms, giving all reconstruction results for all cases will be unnecessary. Only one of them was selected to display, which is five times more conductive in x-direction case. The results of anisotropic EPP algorithm are given in Figure 6.34, anisotropic J-substitution algorithm in Figure 6.35 and anisotropic hybrid J-substitution algorithm in Figure 6.36. Results of magnetic flux density based algorithms are also given in Figure 6.37 and 6.38. Corresponding reconstruction errors are given in tables following every figure.

For the investigation of the linearity properties of the algorithms, two linearity plots, one is for more conductive cases and the other is for less conductive cases, were prepared. In these plots, ten different x-directed true conductivity values of the square object were marked first. Then corresponding reconstructed mean x-directed conductivity values of the square object were marked on the same plot for each algorithm separately and linearity behavior of the algorithms were produced. Linearity plot for more conductive case is given in Figure 6.39, and for less conductive case in Figure 6.40, respectively.

6.5.4.1 Reconstruction Using Anisotropic EPP Algorithm

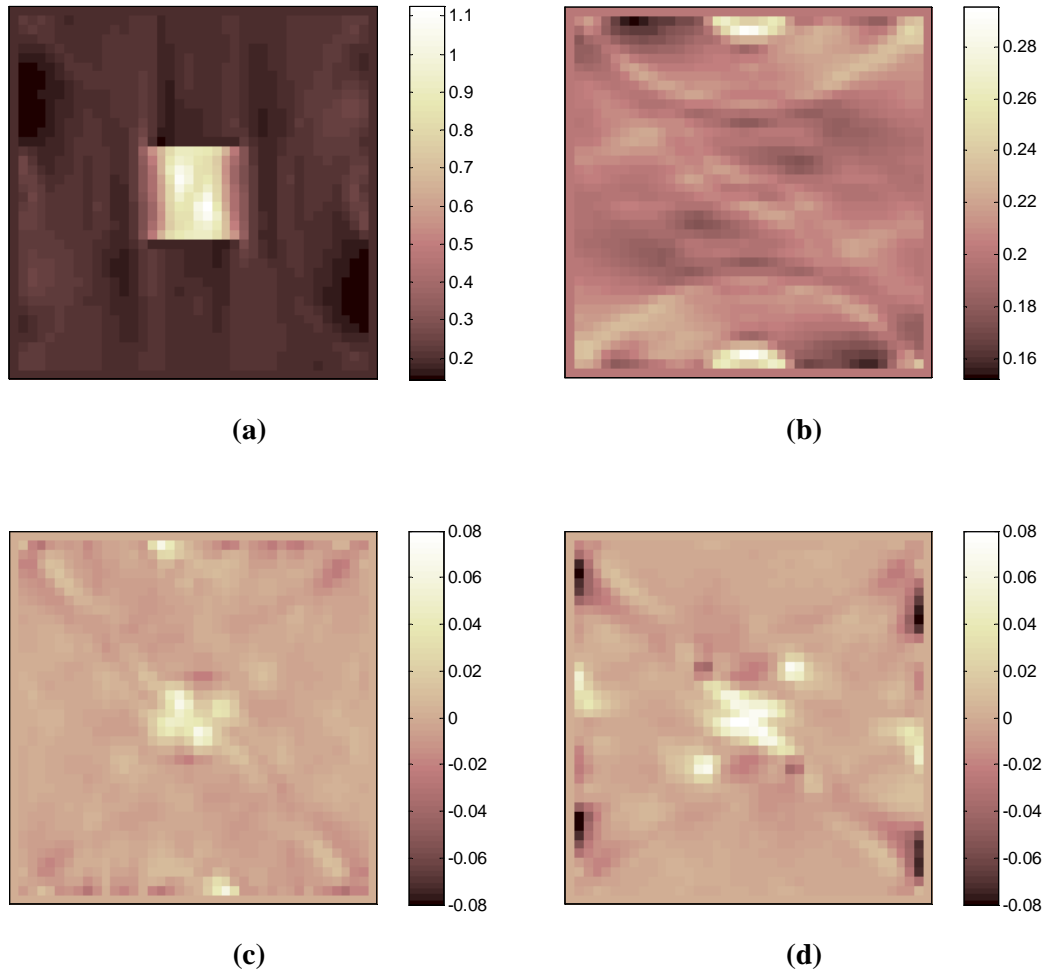


Figure 6.34: Reconstruction results of anisotropic EPP algorithm for model 4 with the object having five times more conductivity with respect to background in x-direction ($\text{SNR} = \infty$): (a) σ_{xx} , (b) σ_{yy} , (c) σ_{xy} and (d) σ_{yy} .

Table 6.21: Percentage errors of reconstructed images in Figure 6.34.

	$\varepsilon_{\sigma_{xx}}$ (%)	$\varepsilon_{\sigma_{yy}}$ (%)
Object	32.10	5.48
Background	11.42	7.78

6.5.4.2 Reconstruction Using Anisotropic J-Substitution Algorithm

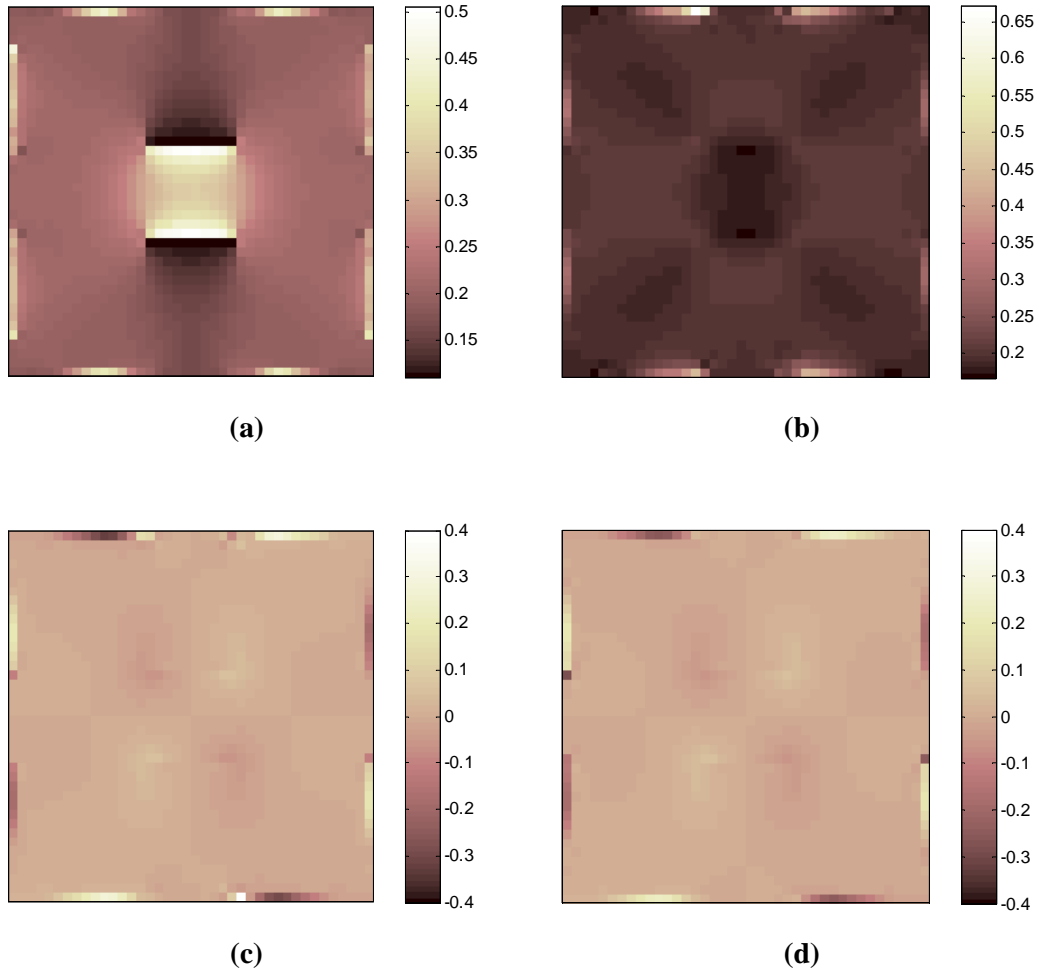


Figure 6.35: Reconstruction results of anisotropic J-substitution algorithm for model 4 with the object having five times more conductivity with respect to background in x-direction ($\text{SNR} = \infty$): (a) σ_{xx} , (b) σ_{yy} , (c) σ_{xy} and (d) σ_{yy} .

Table 6.22: Percentage errors of reconstructed images in Figure 6.35.

	$\mathcal{E}_{\sigma_{xx}}$ (%)	$\mathcal{E}_{\sigma_{yy}}$ (%)
Object	61.46	8.70
Background	14.33	4.70

6.5.4.3 Reconstruction Using Anisotropic Hybrid J-Substitution Algorithm

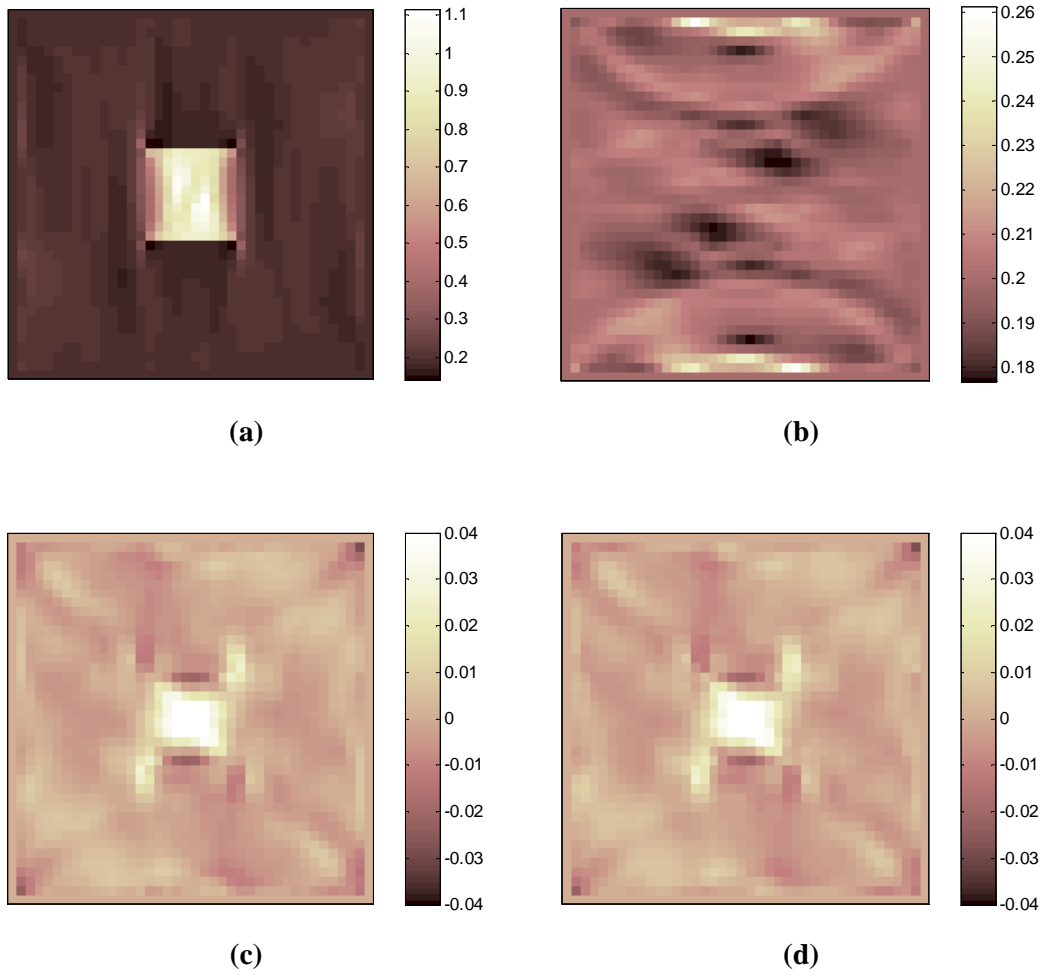


Figure 6.36: Reconstruction results of anisotropic hybrid J-substitution algorithm for model 4 with the object having five times more conductivity with respect to background in x-direction ($\text{SNR} = \infty$): (a) σ_{xx} , (b) σ_{yy} , (c) σ_{xy} and (d) σ_{yy} .

Table 6.23: Percentage errors of reconstructed images in Figure 6.36.

	$\mathcal{E}_{\sigma_{xx}}$ (%)	$\mathcal{E}_{\sigma_{yy}}$ (%)
Object	29.95	5.60
Background	10.07	4.93

6.5.4.4 Reconstruction Using Anisotropic Harmonic B_z Algorithm

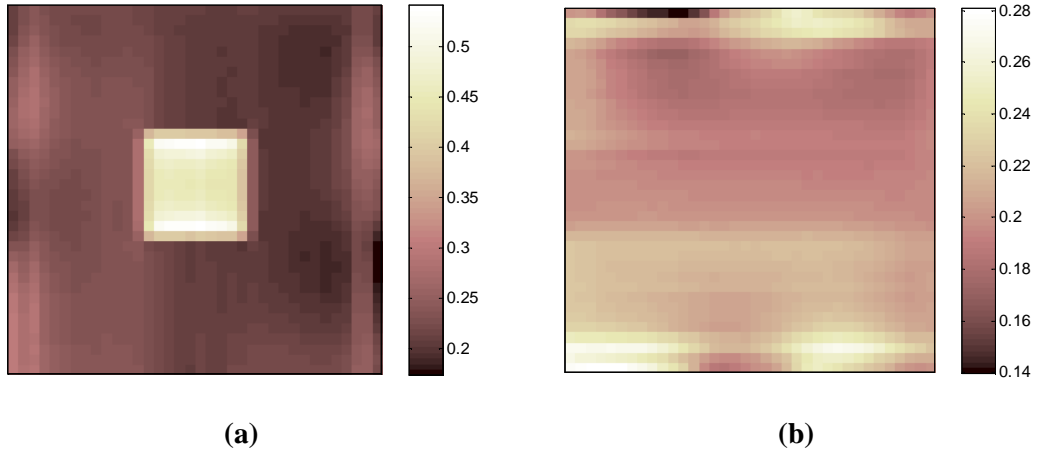


Figure 6.37: Reconstruction results of anisotropic Harmonic B_z algorithm for model 4 with the object having five times more conductivity with respect to background in x-direction ($\text{SNR} = \infty$): (a) σ_{xx} , (b) σ_{yy} .

Table 6.24: Percentage errors of reconstructed images in Figure 6.37.

	$\varepsilon_{\sigma_{xx}}$ (%)	$\varepsilon_{\sigma_{yy}}$ (%)
Object	54.41	5.79
Background	18.15	10.28

6.5.4.5 Reconstruction Using Anisotropic Sensitivity Algorithm

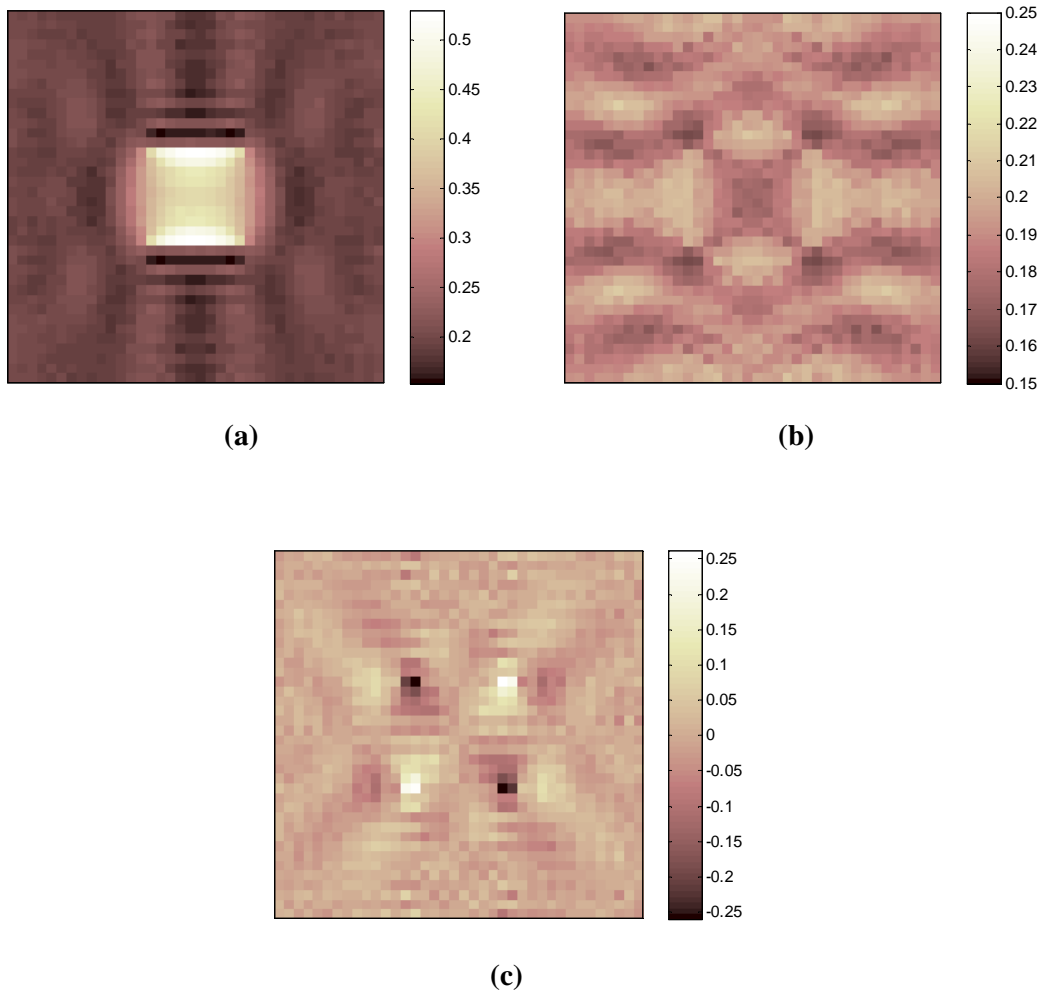


Figure 6.38: Reconstruction results of anisotropic Sensitivity algorithm for model 4 with the object having five times more conductivity with respect to background in x-direction ($\text{SNR} = \infty$): (a) σ_{xx} , (b) σ_{yy} , (c) $\sigma_{xy} - \sigma_{yx}$.

Table 6.25: Percentage errors of reconstructed images in Figure 6.38.

	$\mathcal{E}_{\sigma_{xx}}$ (%)	$\mathcal{E}_{\sigma_{yy}}$ (%)
Object	57.58	8.46
Background	10.55	7.17

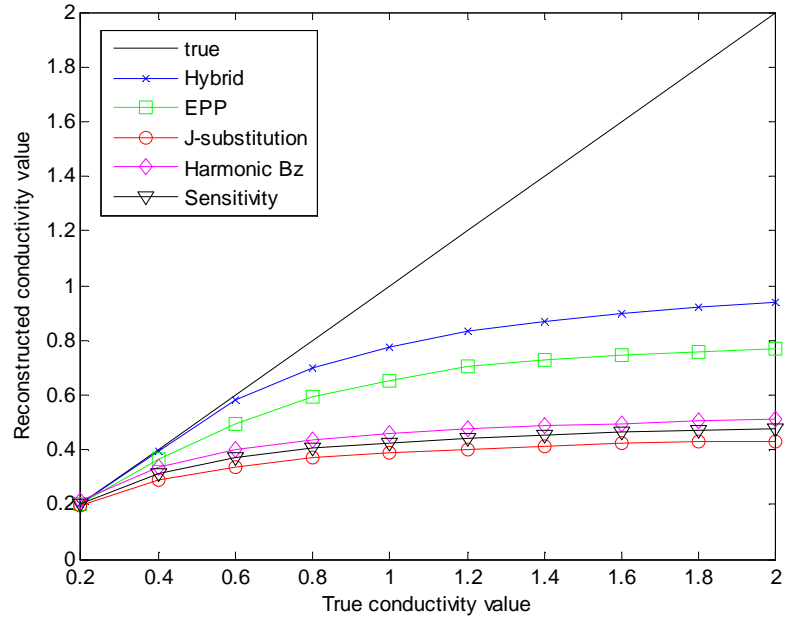


Figure 6.39: Linearity plot for the algorithms for more conductive x-directed conductivity with respect to background.

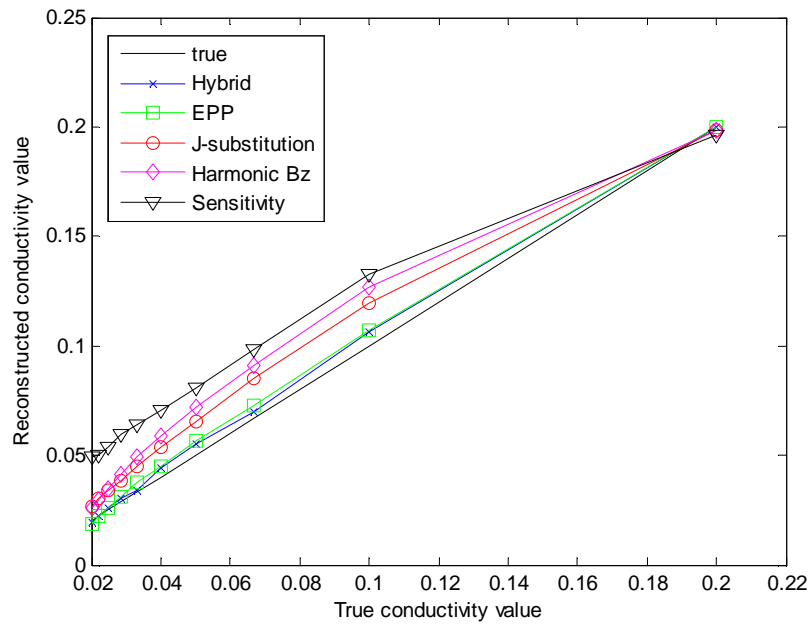


Figure 6.40: Linearity plot for the algorithms for less conductive x-directed conductivity with respect to background.

6.5.4.6 Comparisons for Model 4

As seen from the linearity plot for the more conductive case, all five algorithms confront a problem in reconstructing high contrasts. But, this is not the case when the conductivity becomes less conductive with respect to background. The reason for this situation could be that, when the conductivity value of a region is increased, the current passing through this region will increase. But, this increment in current will not be as many as the increment in conductivity since the total current is kept constant and some of the current will continue to pass through the background. Therefore, reconstruction algorithm will converge to a lower conductivity value than the true conductivity. But, when the conductivity value of a region decreased, the current passing through that region will also decrease almost at the same amount and the remaining of the current will pass through the background. In this case, conductivity value of that region could be calculated accurately.

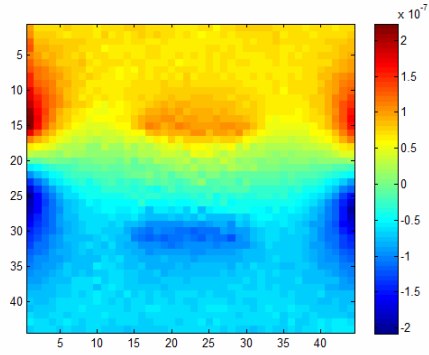
When the individual reconstruction accuracies of the algorithms are investigated for model 4, it is seen that anisotropic hybrid J-substitution algorithm gives the best results among others as in the previous cases. For more and less conductive cases with respect to background, anisotropic sensitivity algorithm shows quite poor results among other algorithms. This is because; underlying theory of that algorithm assumes small conductivity changes, therefore increasing the conductivity contrast causes more erroneous results.

6.5.5 Results for Experimental Models

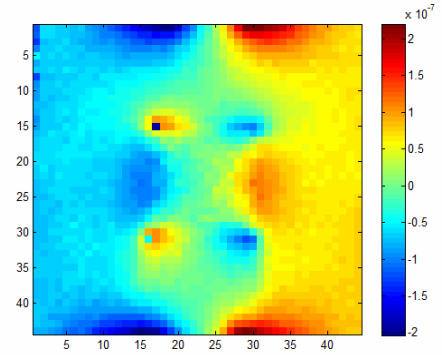
6.5.5.1 Experimental Model 1

Using the data acquisition protocol explained in section 2, magnetic field distributions inside the test phantom 1 in three directions were obtained. Magnetic field distributions in z direction for vertical, horizontal and four adjacent current injection profiles for this phantom are given in Figure 6.41, then using three components of magnetic field measurements, current density distribution inside the FOV can be calculated from Biot-Savart Law. Obtained current density distributions are given in Figure 6.42 for vertical and horizontal current drives.

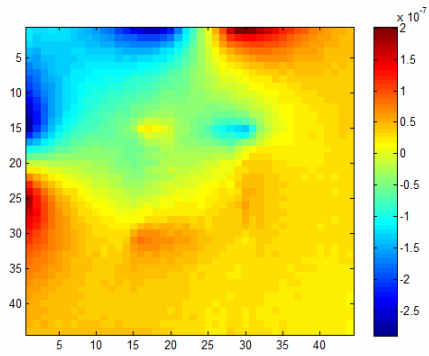
These experimental measurements were used to calculate anisotropic conductivity distribution using five anisotropic conductivity reconstruction algorithms proposed in this thesis. Current density based algorithm's, which are anisotropic EPP, J-Substitution and Hybrid algorithms' results are given in Figure 6.43, 6.44 and 6.45, respectively. Similarly, magnetic flux density based algorithm's, which are anisotropic Harmonic B_z and Sensitivity algorithms' results are given in Figure 6.46 and 6.47, respectively.



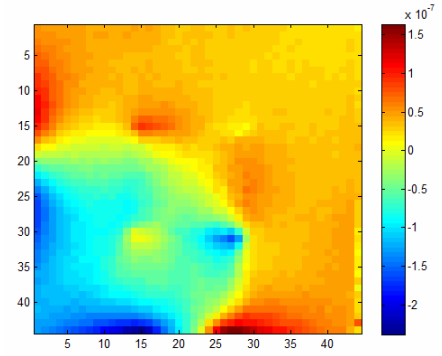
(a)



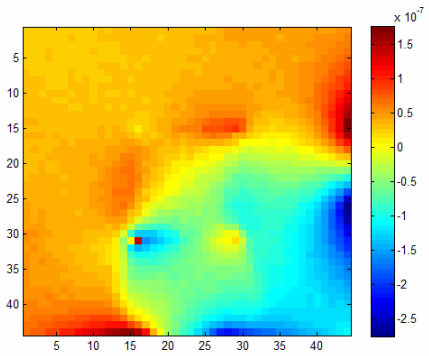
(b)



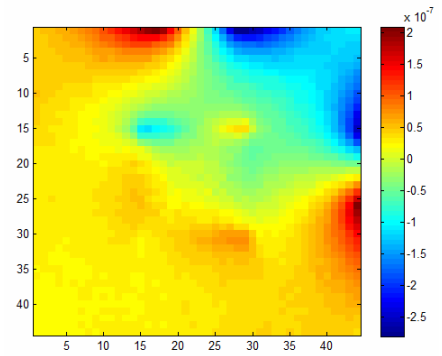
(c)



(d)

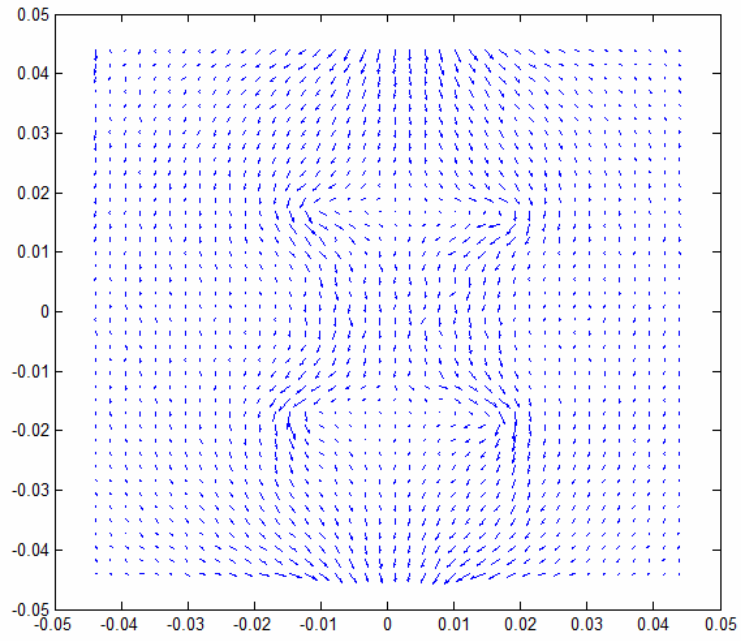


(e)

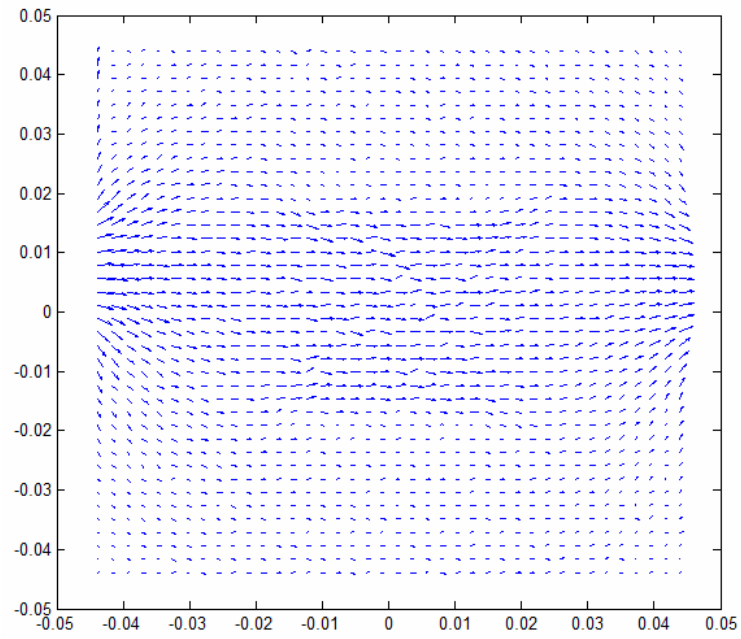


(f)

Figure 6.41: Measured magnetic fields in z direction for experimental model 1, (a) for vertical current injection, (b) for horizontal current injection, (c) for the first adjacent drive, (d) for the second adjacent drive, (e) for the third adjacent drive, (f) for the fourth adjacent drive.



(a)



(b)

Figure 6.42: Current density distributions for experimental model 1: (a) for vertical current injection, (b) for horizontal current injection.

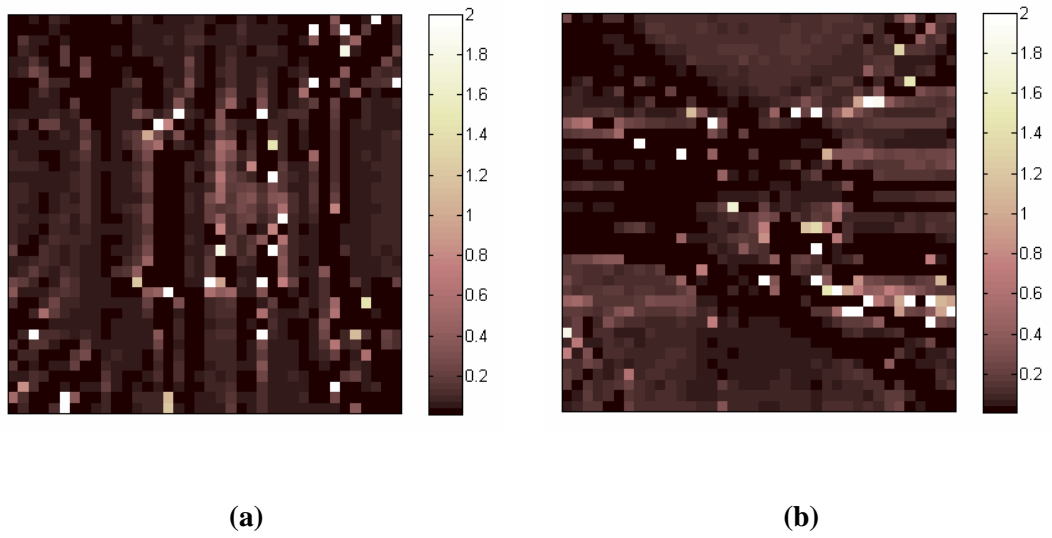


Figure 6.43: Reconstruction results for experimental model 1 using anisotropic EPP algorithm: (a) σ_{xx} , (b) σ_{yy} .

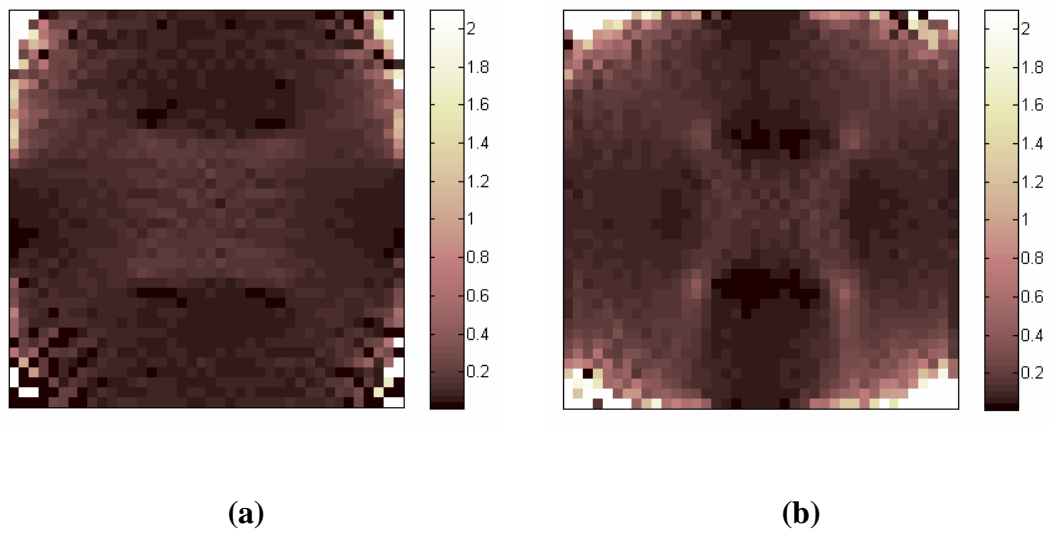
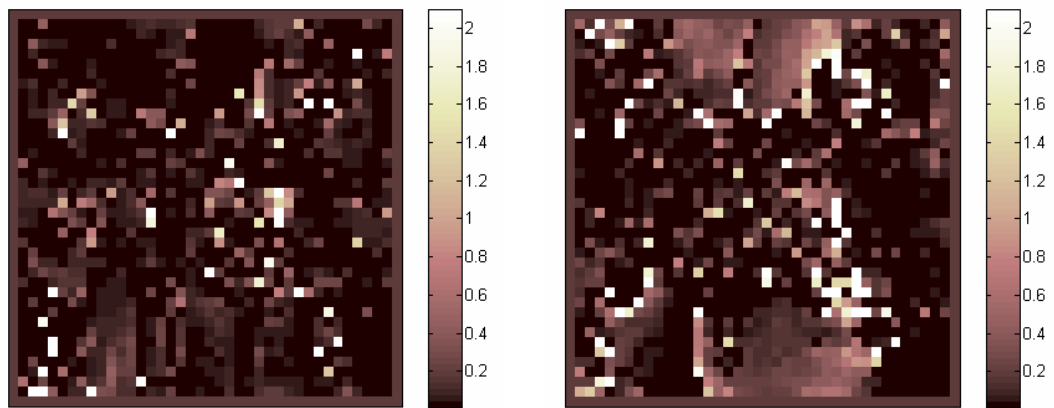


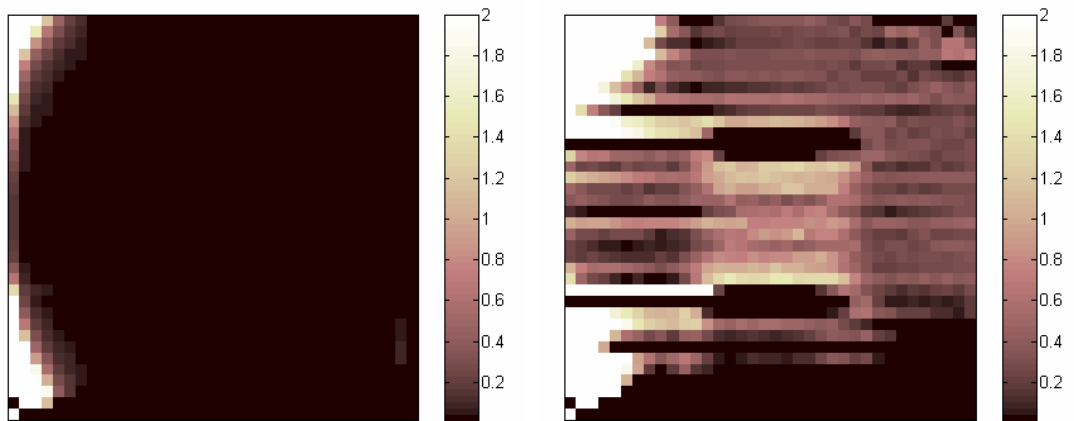
Figure 6.44: Reconstruction results for experimental model 1 using anisotropic J-substitution algorithm: (a) σ_{xx} , (b) σ_{yy} .



(a)

(b)

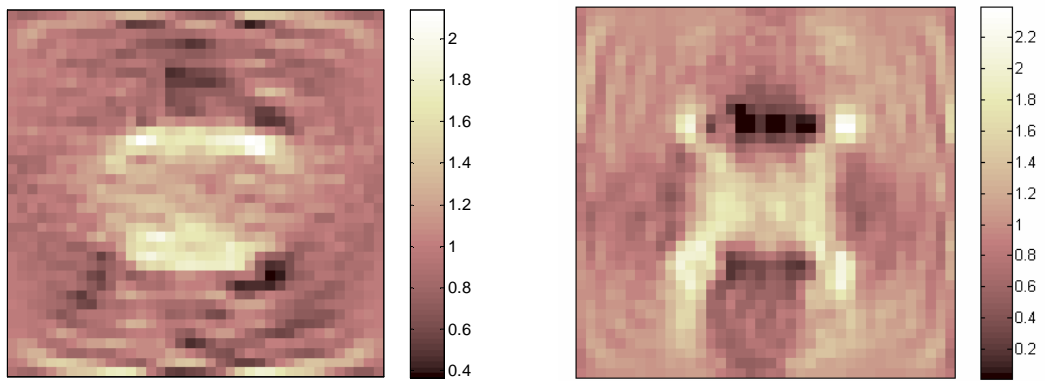
Figure 6.45: Reconstruction results for experimental model 1 using anisotropic Hybrid algorithm: (a) σ_{xx} , (b) σ_{yy} .



(a)

(b)

Figure 6.46: Reconstruction results for experimental model 1 using anisotropic Harmonic B_z algorithm: (a) σ_{xx} , (b) σ_{yy} .



(a)

(b)

Figure 6.47: Reconstruction results for experimental model 1 using anisotropic Sensitivity algorithm: (a) σ_{xx} , (b) σ_{yy} .

After giving these results it will be appropriate to define a conductivity ratio in terms of σ_{xx} and σ_{yy} in order to increase the comprehensibility and make the result more interpretable. Figure 6.48 shows $\arctan(\sigma_{yy} / \sigma_{xx})$ ratio in degree.

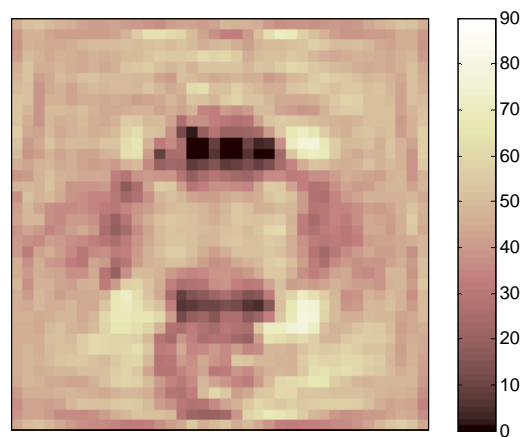


Figure 6.48: Reconstructed conductivity ratio: $\arctan(\sigma_{yy} / \sigma_{xx})$.

6.5.5.2 Experimental Model 2

Similar to the experimental model 1, magnetic field distributions in z direction for vertical, horizontal and four adjacent current injection profiles for the second phantom are given in Figure 6.49. Also, obtained current density distributions are given in Figure 6.50 for vertical and horizontal current drives.

Results of all proposed algorithms are given in Figure 6.51, 6.52, 6.53 6.54 and 6.55.

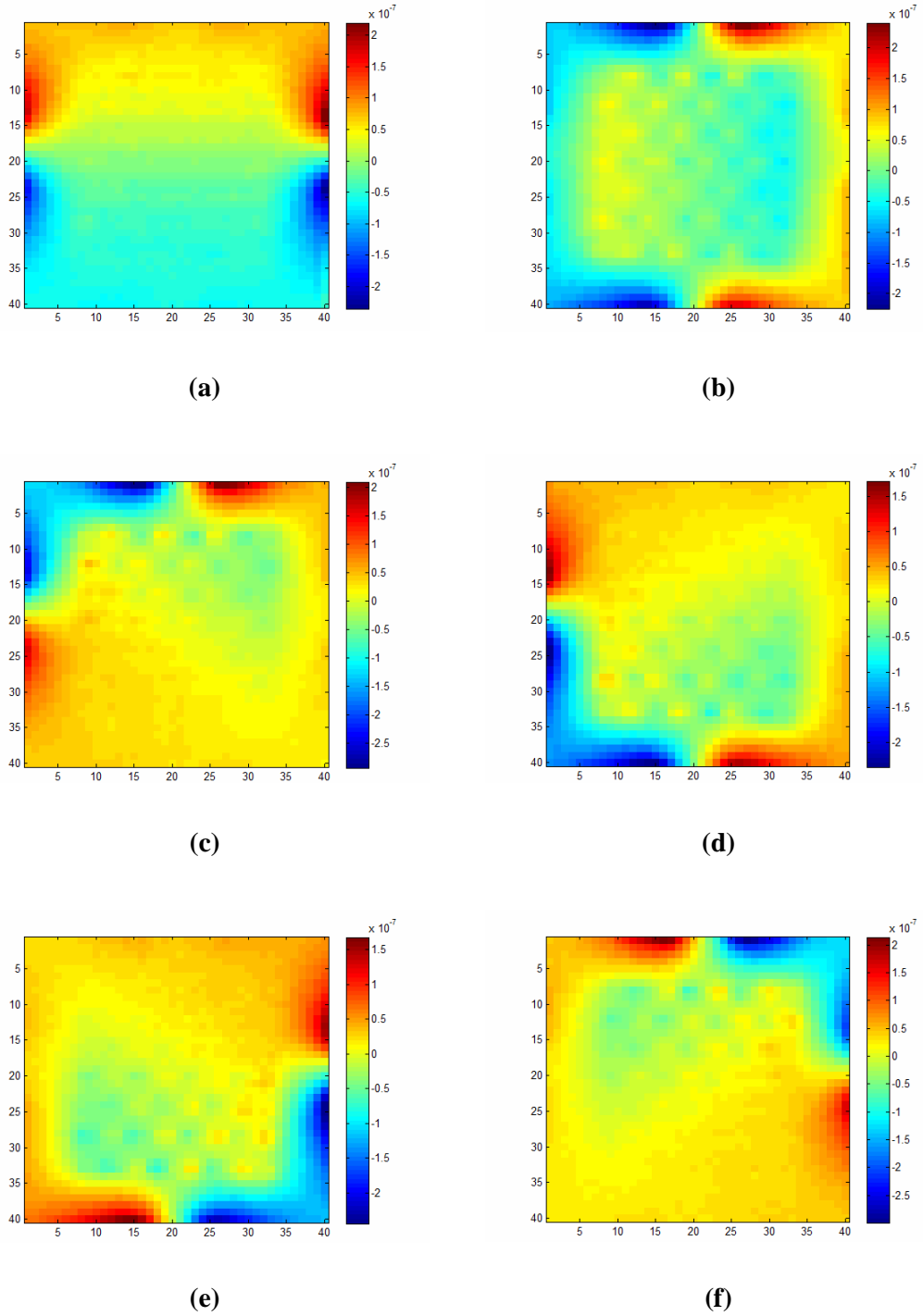
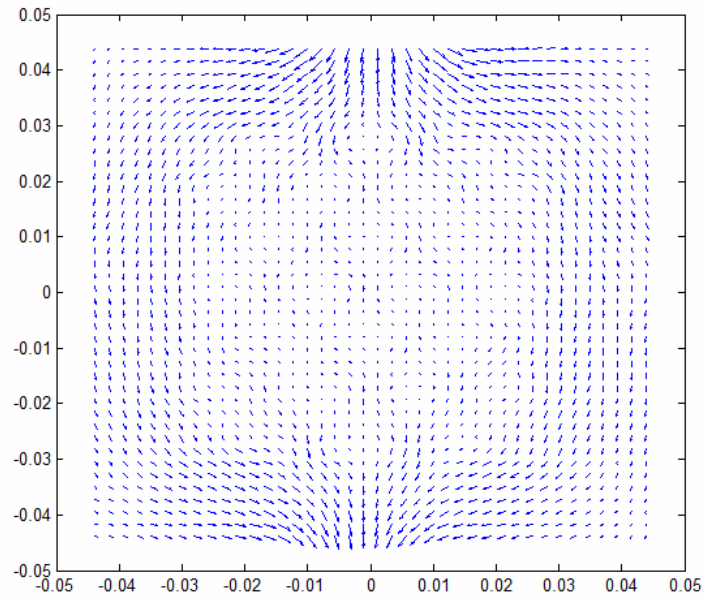
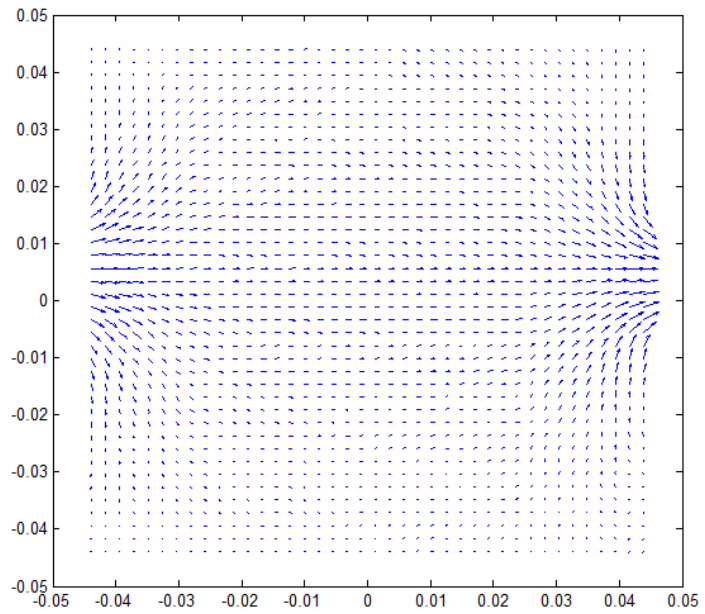


Figure 6.49: Measured magnetic fields in z direction for designed model 2, (a) for vertical current injection, (b) for horizontal current injection, (c) for the first adjacent drive, (d) for the second adjacent drive, (e) for the third adjacent drive, (f) for the fourth adjacent drive.

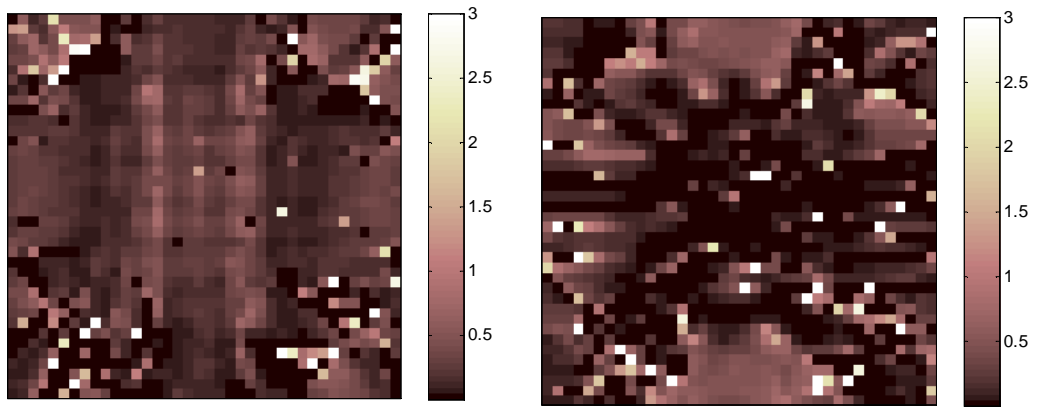


(a)



(b)

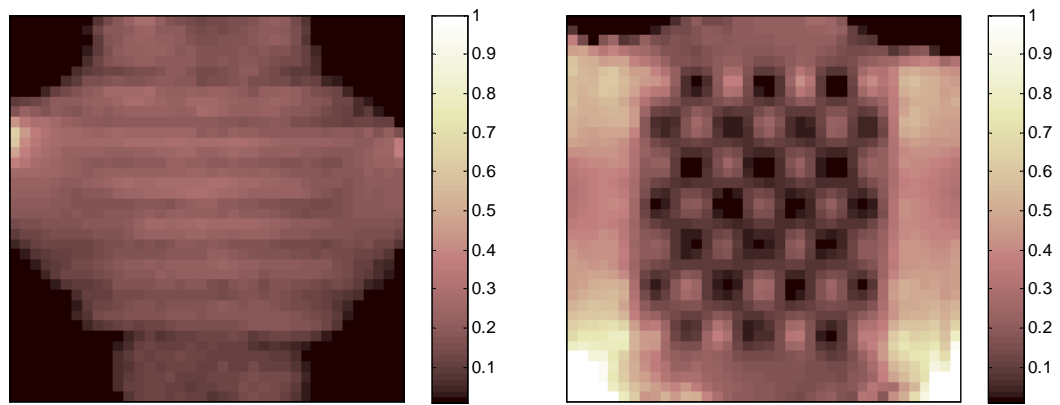
Figure 6.50: Current density distributions for experimental model 2: (a) for vertical current injection, (b) for horizontal current injection.



(a)

(b)

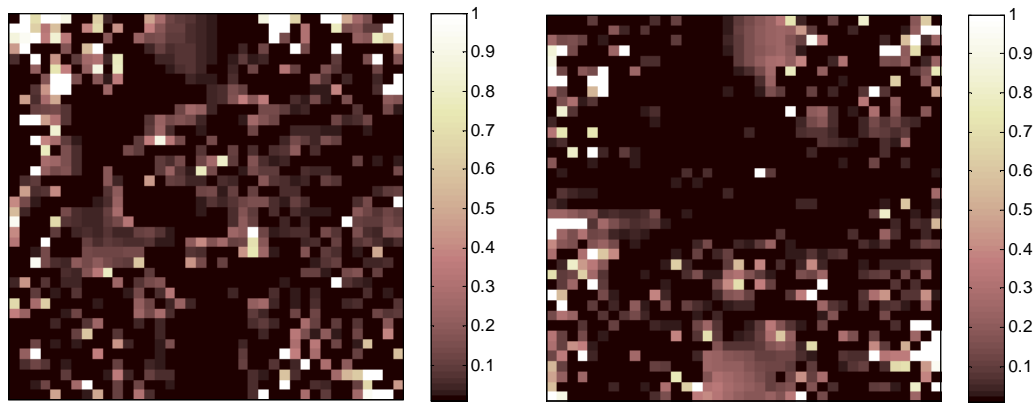
Figure 6.51: Reconstruction results for experimental model 2 using anisotropic EPP algorithm: (a) σ_{xx} , (b) σ_{yy} .



(a)

(b)

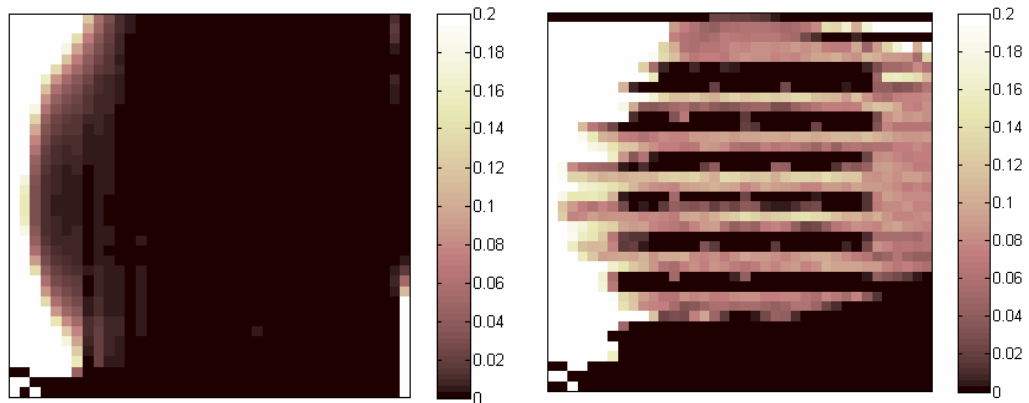
Figure 6.52: Reconstruction results for experimental model 2 using anisotropic J-Substitution algorithm: (a) σ_{xx} , (b) σ_{yy} .



(a)

(b)

Figure 6.53: Reconstruction results for experimental model 2 using anisotropic Hybrid algorithm: (a) σ_{xx} , (b) σ_{yy} .



(a)

(b)

Figure 6.54: Reconstruction results for experimental model 2 using anisotropic Harmonic B_z algorithm: (a) σ_{xx} , (b) σ_{yy} .

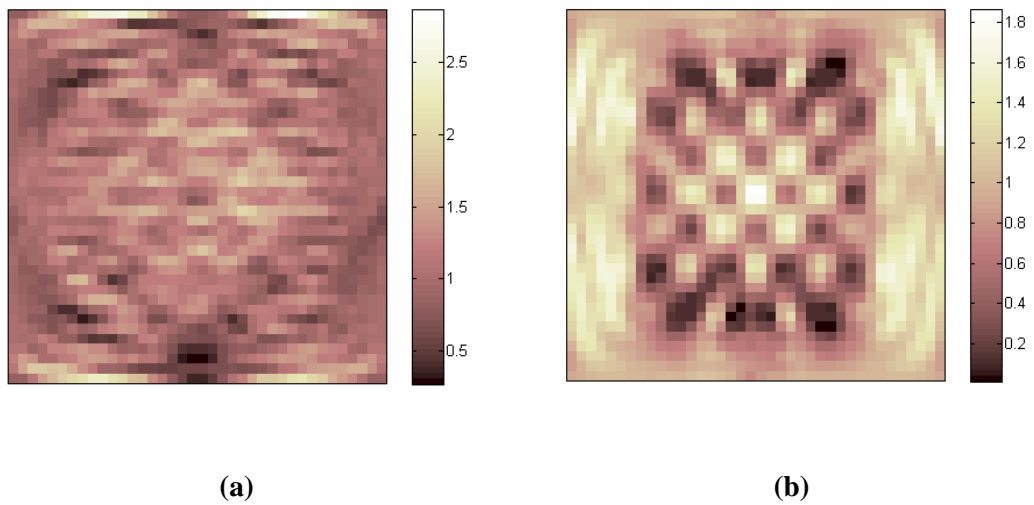


Figure 6.55: Reconstruction results for experimental model 1 using anisotropic Sensitivity algorithm: (a) σ_{xx} , (b) σ_{yy} .

Again, in order to increase the comprehensibility and make the result more interpretable, the same conductivity ratio is calculated and visualized as in experimental model 1. Figure 3.55 shows this $\arctan(\sigma_{yy} / \sigma_{xx})$ ratio in degree.

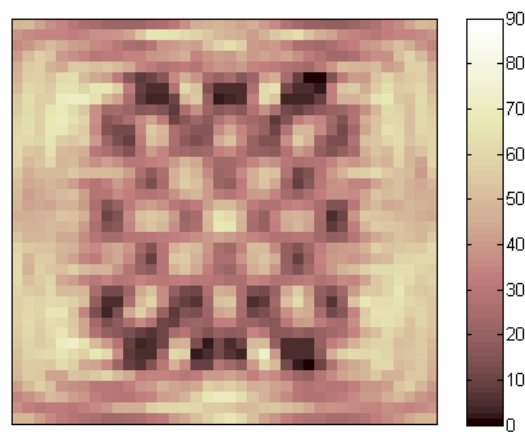


Figure 6.56: Reconstructed conductivity ratio: $\arctan(\sigma_{yy} / \sigma_{xx})$.

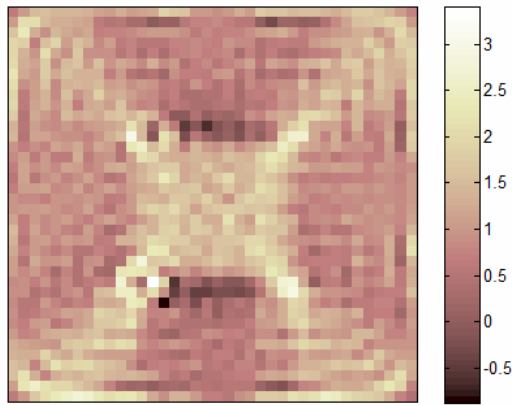
6.5.5.3 Comparisons for Experimental Models

As seen from the results, magnetic flux density based algorithms perform better than current density based algorithms. This is because, in order to find the current density distributions, it is necessary to take the derivatives of noisy magnetic flux density distributions and it is known that derivation of a noisy data increases noise level dramatically. Therefore, current density distributions obtained using Biot-Savart Law become noisier. Since, current density based algorithms use this data as input, their results become erroneous. When the individual results of these algorithms are compared, it is seen that anisotropic EPP algorithm gives the worst results among others because it constructs equipotential lines using current density vectors and this makes it more sensitive to the current density noise. Also current density vectors become noisier at the corners and some edges since the current flow is very little at these points. Therefore, equipotential lines starting from that points goes on the wrong way and projects surface potentials to the wrong regions. Since, anisotropic J-Substitution algorithm calculated the inner potential field using FEM, it is less sensitive to the current density noise. Actually, anisotropic hybrid algorithm is expected to show a similar performance to J-substitution algorithm but, since its initial conductivity comes from EPP algorithm and since those conductivities are very erroneous, hybrid algorithm reconstructed the conductivities like EPP algorithm.

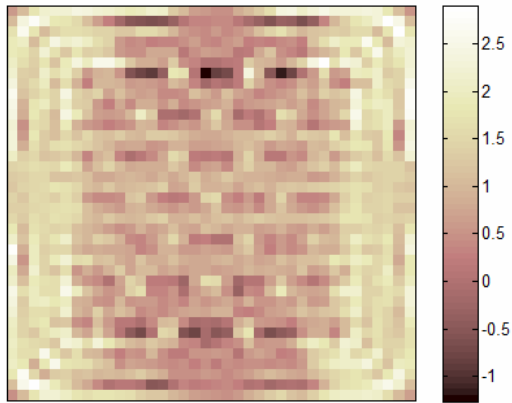
When the individual results of magnetic flux density based algorithms are compared, anisotropic Sensitivity algorithm shows better performance than anisotropic Harmonic B_z algorithm. The reason for this situation is that Harmonic B_z algorithm takes the derivative of magnetic flux density data twice and this derivative operation increases the noise level of the flux density data tremendously. Therefore, anisotropic Harmonic B_z algorithm results more erroneous results. Furthermore, anisotropic Sensitivity algorithm shows the best results among proposed five algorithms. This is because, magnetic flux density measurement can be made at every point in the FOV with equal sensitivity and this makes the algorithm more robust against measurement noise.

When the conductivity ratios in Figure 6.48 and 6.56 are investigated, it is seen that zero degree is found in the vicinity of insulator layers. This means that, there exist nonzero σ_{xx} conductivity component, but σ_{yy} component is equal to zero. This is as expected since insulator layer do not let conduction in y direction therefore, y directed conductivity component is zero. On the other regions, conductivity ratio is equal to about 45 degree which means isotropic conductivity.

As a final step on experimental study, magnetic flux density measurements for both phantoms are fed into the isotropic sensitivity algorithm. Since this algorithm assumes isotropic conductivity, only one conductivity distribution is obtained for every model. Figure 6.57 shows reconstructed conductivity distributions. As seen in the figures, reconstructed images look like y directed anisotropic conductivity component of each model. But images are much more corrupted with respect to the anisotropic reconstructions. It is also obvious that conductivity distribution inside the FOV can not be commented easily without having no idea about the x directed conductivity distribution.



(a)



(b)

Figure 6.57: Reconstructed conductivity image using isotropic Sensitivity algorithm, (a) for phantom 1, (b) for phantom 2.

6.6 Final Comparisons

In order to compare all of the algorithms easily by visualizing this comparison, a performance chart was prepared as seen in Figure 6.57. In this chart, every axis shows a comparison criteria and performance increases while going far from center on every axis. Eight different criteria were selected for comparison. These are, object error for SNR=13 and infinity, background error SNR=13 and infinity, memory usage, time consumption, simulation reconstruction quality, experimental reconstruction quality. Memory usage and time consumption parameters were

evaluated on the same computer (Intel Core 2 Duo E8400 CPU at 3 GHz and 4 GB of RAM) for all algorithms. Results of that study showed that anisotropic EPP algorithm reconstructs in about 5 minutes and using a little amount of RAM, whereas anisotropic J-substitution and Harmonic B_z algorithm requires about 20 minutes and a big amount of RAM. When the anisotropic hybrid J-substitution algorithm is used, it reconstructs in about 10 minutes including the EPP algorithm with an intermediate amount of RAM. Anisotropic Sensitivity algorithm also requires a big amount of RAM but it reconstructs in about 7 minutes. Its experimental reconstruction performance is also superior among others.

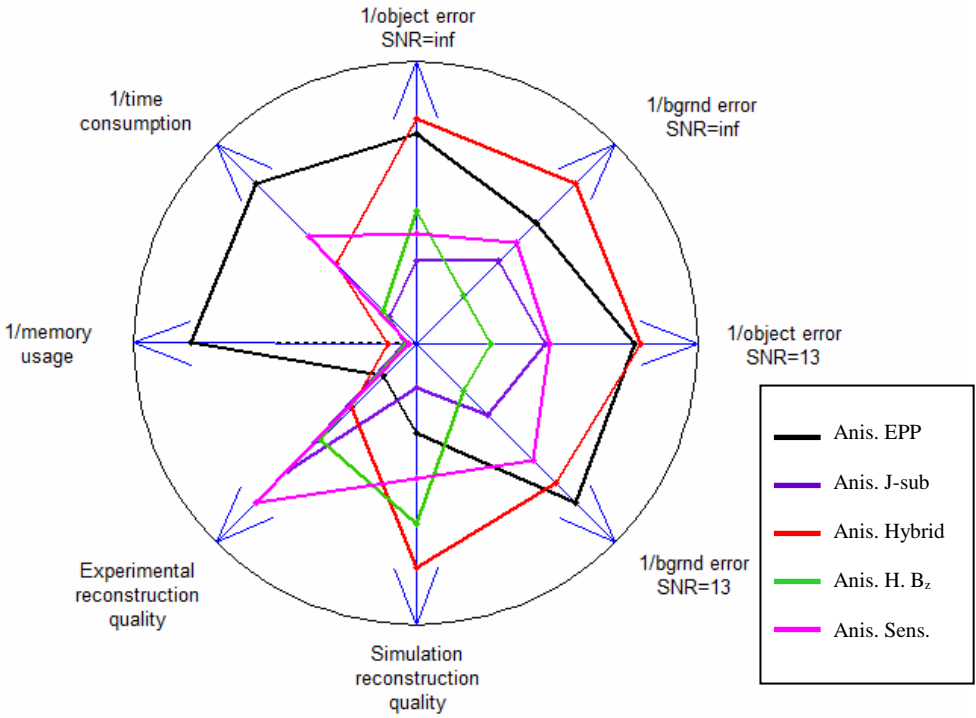


Figure 6.58: Performance chart for five algorithms.

CHAPTER 7

CONCLUSIONS

7.1 Summary of the Thesis Work

In this study, five novel MREIT reconstruction algorithms to image anisotropic conductivity were proposed. Three of the proposed techniques use the current density distribution data with one potential measurement as input and reconstructs anisotropic conductivity components iteratively. Inner potential distribution is required for these algorithms. Anisotropic equipotential projection algorithm calculates potential field using equipotential lines. Equipotential lines are perpendicular to the current lines in case of isotropic conductivity but, in case of anisotropic conductivity their crossing angle are determined by the conductivity anisotropy at the crossing point. Different from the anisotropic EPP technique, anisotropic J-substitution technique calculates potential field using FEM techniques. The third technique, called anisotropic hybrid J-substitution algorithm, combines both techniques. It first calculates the anisotropic conductivity using anisotropic EPP technique and then this conductivity distribution is given to the anisotropic J-substitution algorithm as initial conductivity. Other two algorithms use magnetic flux density data and one potential measurement as input and calculate the anisotropic conductivity distribution uniquely. Anisotropic Harmonic B_z algorithm takes the second derivative of measured flux density data and uses an iterative algorithm. On the other hand, anisotropic Sensitivity algorithm first calculates sensitivity matrix and obtains anisotropic conductivity directly. Sensitivity matrix is only depends on the outer geometry and boundary conditions, therefore it can be calculated once and stored.

In order to explore the reconstruction performances of the proposed algorithms, 4 different computer models were prepared. These models were designed to cover all critical aspects in reconstruction phenomena, such as reconstruction accuracy, noise performance, spatial resolution, point spread function (PSF), linearity, position dependency, etc.

Algorithms were also evaluated with experimental measurements in this thesis study. Measurements were performed in METU EEE 0.15T MR System using designed and manufactured test phantoms.

7.2 Conclusions

MREIT is an emerging imaging modality in the field of tomographic imaging. Various studies exist in literature. Almost all of the MREIT reconstruction algorithms assume isotropic conductivity in order to simplify the underlying background. But it is known that most of the biological tissues have anisotropic conductivity values. The most important contribution of this study to the MREIT literature is five novel anisotropic conductivity reconstruction algorithms. By this contribution, anisotropic conductivity reconstruction deficiency in the MREIT literature has been overcome to some extent.

Anisotropic MREIT algorithms proposed prior to this thesis have been tested with different computer models. Therefore, an accurate cross comparison between them did not exist. In this thesis, four different computer models were designed to test all the algorithms. During the design process of these models, many aspects were taken into account for anisotropic conductivity reconstruction phenomena such as reconstruction accuracy, noise performance, spatial resolution, point spread function (PSF), linearity, position.

Experimental measurements were also made in this study which is avoided most of the studies because of difficulties. A current source was designed and manufactured

for these measurements. This current source was placed inside the Faraday cage timing signals were required to transport from computer to the source. For this purpose, fiber optic cables were used and penetration of the RF noises inside the Faraday cage over the timing cables was eliminated. Another important issue about the current source is the power supply unit of it. First, AC/DC converter was used to supply the source but this led to decreasing SNR ratio and even loss of MR signal because of the switching noise of the AC/DC converters. Because of this, DC batteries were used and the problem of signal loss was solved.

When the results of all algorithms with simulation and experimental data are investigated altogether, anisotropic sensitivity algorithm shows a magnificent performance among others. This algorithm does not also require rotation of the object in the MRI scanner which is very difficult to achieve in application. Furthermore, anisotropic sensitivity algorithm calculates the sensitivity matrix once for given current injection drives and boundary conditions, and calculates the anisotropic conductivity faster than almost all other algorithms. The only drawback of that algorithm is its high memory usage but, in today's rapidly developing computer era, this is actually not a critical problem.

Another important study during this thesis was the preparation of the test phantoms. In order to remove the ion diffusion between the layers, a solidifying material was used. Actually, this material itself is sufficient to obtain a solid material when added to water. But, it is necessary to add CuSO_4 to water to decrease the T_1 time during measurements, and when the solidifying material is mixed with CuSO_4 solution, it loses its solidifying property and the mixture became a gelled material instead of a solid material. Therefore, in order to make the material solid, agar is used in the mixture and a solid material with very low ion diffusion is obtained.

All these experimental studies are a very important part of this thesis study. Up to date, none of the anisotropic conductivity reconstruction algorithms are tested with experimental data. In order to incorporate MREIT technique into the diagnostic imaging techniques, experimental realization of it must be completed. With this

study, five anisotropic conductivity reconstruction algorithms and experimental realization of the technique are added to the MREIT literature. But, before application of the technique to the humans, applied current must be decreased under the safety limit. Using the optimized current injection strategies for MREIT in literature [51], current could be decreased under the safety limit. Future studies must certainly be in this direction. If it is succeeded, MREIT would have a chance of being a diagnostic imaging technique and the algorithms proposed in this thesis would be used to reconstruct anisotropic conductivity distributions of tissues.

REFERENCES

- [1] Boone K., Barber D. and Brown B., "Imaging with electricity: Report of the European concerted action on impedance tomography", *Journal of Medical Engineering and Technology*, 21, no 6, 201-232, 1997.
- [2] Morucci J. P. and Rigaud B., "Bioelectrical impedance techniques in medicine part III; Impedance imaging, medical applications", *Critical Reviews in Biomedical Engineering*, 655-677, 1996.
- [3] Gonçalves S., De Munck J. C., Heethaar R. M., Lopes da Silva F. H. and Van Dijk B. W., "The application of electrical impedance tomography to reduce systematic errors in the eeg inverse problem – a simulation study", *Physiol. Meas.*, 21, 379-393, 2000.
- [4] Van Burik M. J. and Peters P. J., "Estimation of the electric conductivity from scalp measurements: Feasibility and application to source localization", *Clin. Neurophysiol*, 111, 1514-1521, 2000.
- [5] B. Murat Eyüboğlu, "Electrical Impedance Imaging: Injected Current Electrical Impedance Imaging," *WILEY Encyclopedia of Biomedical Engineering (Metin Akay, ed.)*, Vol.2, 1195-1205, 2006.
- [6] Nevzat G. Gencer, "Induced Current Electrical Impedance Tomography", *Wiley Encyclopedia of Biomedical Engineering (Metin Akay, ed.)*, 2006.
- [7] Scott G. C., Joy M. L. G., Armstrong R. L. and Hankelman R. M., "Measurement of non-uniform current density by magnetic resonance", *IEEE Transactions on Medical Imaging*, 10, no 3, 362-374, 1991.
- [8] Scott G. C., Joy M. L. G., Armstrong R. L. and Hankelman R. M., "RF current density imaging in inhomogeneous media", *Magnetic Resonance in Medicine*, 28, 186-201, 1992.
- [9] Scott G. C., Joy M. L. G., Armstrong R. L. and Hankelman R. M., "Electromagnetic considerations for RF current density imaging", *IEEE Transactions on Medical Imaging*, 14, 515-524, September 1995.
- [10] Müftüler L. T., "Measurement of magnetic field generated by non-uniform AC current density using magnetic resonance", *PhD Thesis*, Middle East Technical University, Ankara, Turkey, 1996.
- [11] İder Y. Z. and Müftüler L. T., "Measurement of AC magnetic field distribution using magnetic resonance imaging", *IEEE Transactions on Medical Imaging*, 16, 617-622, September 1997.
- [12] Gamba H. R. and Delpy D. T., "Artefacts in MR images of electrical current distribution", *Phys. Med. Biol.*, 42, 2481-2491, 1997.

- [13] Sersa I., Beravs K., Dodd N. J. F., Zhao S., Miklavcic D. and Demsar F., “Electric current density imaging of mice tumors”, *Magnetic Resonance in Medicine*, 37, 404-409, 1997.
- [14] Beravs K., White D., Sersa I. and Demsar F., “Electric current density imaging of bone by MRI”, *Magnetic Resonance Imaging*, 15, no 8, 909-915, 1997.
- [15] Joy M. L. G., Lebedev V. P. and Gati J. S., “Imaging of current density and current pathways in rabbit brain during transcranial electrostimulation”, 1999.
- [16] Bodurka J., Jesnaowicz A., Hyde J. S., Xu H., Estkowski L. And Li J. S., “Current-induced magnetic resonance phase imaging”, *Journal of Magnetic Resonance*, 137, 265-271, 1999.
- [17] Mikac U., Demsar F., Beravs K. And Sersa I., “Magnetic resonance imaging of alternating electric currents”, *Magnetic Resonance Imaging*, 19, 845-856, 2001.
- [18] Zhang N., “Electrical impedance tomography based on current density imaging”, *Master Thesis*, University of Toronto, Dept. of Electrical and Electronics Eng., Toronto, Canada, 1992.
- [19] Woo E. J., Lee S. and Mun C. W., “Impedance tomography using internal current density distribution measured by nuclear magnetic resonance”, *SPIE*, 2299, 377-385, 1994.
- [20] Birgül Ö. and İder Y. Z., “Use of magnetic field generated by the internal distribution of injected currents for electrical impedance tomography”, *Proceedings of the IXth Int. Conf. on Bio-Impedance*, 418-419, 1995.
- [21] İder Y. Z. and Birgül Ö., “Use of magnetic field generated by the internal distribution of injected currents for electrical impedance tomography (MR-EIT)”, *Electric Turkish J. of Elec. Eng. and Comp. Sci.*, 6, no 3, 215-225, 1998.
- [22] Birgül Ö., Eyüboğlu B. M. and İder Y. Z., “Current constrained voltage scaled reconstruction (CCVSR) algorithm for magnetic resonance-electrical impedance tomography and performance with different probing current patterns”, *Physics in Medicine and Biology*, 48, 653-671, 2003.
- [23] Eyüboğlu B. M., Reddy R. and Leigh J. S., “Magnetic resonance-electrical impedance tomography”, *patent no: US6,397,095 B1, provisional patent application on Mar. 1, 1999*, May 2002.
- [24] Özdemir M. S. and Eyüboğlu B. M., “Novel fast reconstruction algorithm for magnetic resonance electrical impedance tomography”, *Proceedings of Biyomut 8th Annual Conference, Istanbul, Turkey*, 129-134, 2002.
- [25] Özdemir M. S., Eyüboğlu B. M. and Özbek O., “Equipotential projection-based magnetic resonance electrical impedance tomography and experimental realization”, *Physics in Medicine and Biology*, 49, 4765-4783, 2004.
- [26] Kwon O., Lee J. Y. and Yoon J. R., “Equipotential line method for magnetic resonance electrical impedance tomography”, *Inverse Problems*, 18, 1089-1100, 2002.

- [27] Kwon O., Woo E. J., Yoon J. R. and Seo J. K., "Magnetic resonance electrical impedance tomography (MREIT): Simulation study of j-substitution algorithm", *IEEE Transactions on Biomedical Engineering*, 49, 160-167, February 2002.
- [28] Khang H. S., Lee B. I., Oh S. H., Woo E. J., Lee S. Y., Cho M. H., Kwon O., Yoon J. R. and Seo J. K., "J-substitution algorithm in magnetic resonance electrical impedance tomography (MREIT): Phantom experiments for static resistivity images", *IEEE Transactions on Medical Imaging*, 21, 695-702, June 2002.
- [29] Lee B. I., Oh S. H., Woo E. J., Lee S. Y., Cho M. H., Kwon O., Seo J. K. And Baek W. S., "Static resistivity image of a cubic saline phantom in magnetic resonance electrical impedance tomography (MREIT)", *Physiol. Meas.*, 24, 579-589, 2003.
- [30] Boyacıoğlu R., Eyüboğlu B. M., "J-substitution and filtered Equipotential projection based hybrid MREIT reconstruction algorithm", *Proc. of Med. Physics and Biomed. Eng. World Congress*, 2009.
- [31] Seo J. K., Yoon J. R., Woo E. J. and Kwon O., "Reconstruction of conductivity and current density images using only one component of magnetic field measurements", *IEEE Trans. On Biomedical Engineering*, 50, 1121-1124, 2003.
- [32] Oh S. H., Lee B. I., Woo E. J., Lee S. Y., Cho M. H., Kwon O. and Seo J. K., "Conductivity and current density image reconstruction using Harmonic B_z algorithm in magnetic resonance electrical impedance tomography", *Phys. Med. Biol.*, 48, 3101-3116, 2003.
- [33] Oh S. H., Lee B. I., Park T. S., Lee S. Y., Woo E. J. and Cho M. H., "Magnetic resonance electrical impedance tomography at 3 Tesla field strength", *Mag. Reson. Med.*, 51, 1292-1296, 2004.
- [34] Park C., Kwon O., Woo E. J. and Seo J. K., "Electrical conductivity imaging using gradient B_z decomposition algorithm in magnetic resonance electrical impedance tomography (MREIT)", *IEEE Trans. On Medical Imaging*, 23, 388-394, 2004.
- [35] Oh S. H., Lee B. I., Woo E. J., Lee S. Y., Kim T. S., Kwon O. and Seo J. K., "Electrical conductivity images of biological tissue phantoms in MREIT", *Physiol. Meas.*, 26, 279-288, 2005.
- [36] İder Y. Z., Onart S. and Lionheart W. R. B., "Uniqueness and reconstruction in magnetic resonance electrical impedance tomography (MR-EIT)", *Physiol. Meas.*, 24, 591-604, 2003.
- [37] İder Y. Z., Onart S., "Algebraic reconstruction for 3D magnetic resonance–electrical impedance tomography (MREIT) using one component of magnetic flux density", *Physiol. Meas.*, 25, 281-294, 2004.
- [38] Lee B. I., Oh S. H., Kim T. S., Woo E. J., Lee S. Y., Kwon O., and Seo J. K., "Basic setup for breast conductivity imaging using magnetic resonance electrical impedance tomography", *Phys. Med. Biol.*, 51, 443-455, 2006.

- [39] Sadleir R., Grant S., Zhang S. U., Oh S. H., Lee B. I., and Woo E. J., “High field MREIT: setup and tissue phantom imaging at 11 T”, *Physiol. Meas.*, 27, 261-270, 2006.
- [40] Kim H. J., Lee B. I., Cho Y., Kim Y. T., Kang B. T., Park H. M., Lee S. Y., Seo J. K., and Woo E. J., “Conductivity imaging of canine brain using a 3T MREIT system: postmortem experiments”, *Physiol. Meas.*, 28, 1341-1353, 2007.
- [41] Kim H. J., Oh T. I., Kim Y. T., Lee B. I., Woo E. J., Seo J. K., Lee S. Y., Kwon O., Park C., Kang B. T., Park H. M., “In vivo electrical conductivity imaging of a canine brain using a 3 T MREIT system”, *Physiol. Meas.*, 29, 1145-1155, 2008.
- [42] Breckon W., “The problem of anisotropy in electrical impedance tomography”, *Proc. of IEEE EMBS Conf.*, 14, 1734-1735, 1992.
- [43] Seo J. K., Pyo H. C., Park C., Kwon O. and Woo E. J., “Image reconstruction of anisotropic conductivity tensor distribution in MREIT: computer simulation study”, *Phys. Med. Biol.*, 49, 4371-4382, 2004.
- [44] Değirmenci E., Eyüboğlu B. M., “Anisotropic conductivity imaging with MREIT using equipotential projection algorithm”, *Phys. Med. Biol.*, 52, 7229-7242, 2007.
- [45] Değirmenci E., Eyüboğlu B. M., “Anisotropic conductivity imaging with MREIT using J-substitution and hybrid J-substitution algorithms”, *Proc. of Med. Physics and Biomed. Eng. World Congress*, 2009.
- [46] Birgül Ö., “Development of reconstruction algorithms for magnetic resonance electrical impedance tomography and experimental realization”, *PhD. Thesis, METU*, 2002.
- [47] Eyüboğlu B. M., Reddy R, and Leigh J. S., “Imaging electrical current density using nuclear magnetic resonance”, *Elektrik Turkish J. of Elec. Eng. and Comp. Sci.*, 6, 201-214, 1998.
- [48] Liang Z. P., “A model based method for phase unwrapping”, *IEEE Trans. Med. Imag.*, 15,893-897, 1996.
- [49] Oilcenter, “TX150, TX151”, <http://www.oilcenter.com/international/industry.asp?industry=Other>, 11.05.2010.
- [50] Mikrobiyoloji, “Agar-agar” <http://www.mikrobiyoloji.org/genelpdf/920020280.pdf>, 11.05.2010.
- [51] H. Altunel, B.M. Eyüboğlu, A. Köksal, “Current injection optimization for Magnetic Resonance Electrical Impedance Tomography (MREIT)”, *Proc. of 13th Conference on Electrical Bioimpedance and 8th Conference on Electrical Impedance Tomography, Graz – Austria, IFMBE Proceedings*, vol. 17, DVD-ROM Springer-Verlag ISBN 3-540-73840-4, pp.504-7, 2007.

APPENDIX A

EXTENSION OF THE TECHNIQUE PROPOSED BY IDER *ET AL* FOR THE RECONSTRUCTION OF ANISOTROPIC CONDUCTIVITY

In this part of the study, MREIT algorithm proposed by Ider *et al* in 2003 [36] for isotropic conductivity imaging is tried to be extended for the reconstruction of anisotropic conductivity. But because of some problems encountered during the study, this study could not be completed with the reconstruction of anisotropic conductivity. In the following section, proposed algorithm will be explained in detail with the problems encountered and simulation results will be given.

A.1 Algorithm

Let Ω be a connected and bounded domain in R^3 , with boundary Γ . Inside this

domain, we define a positive definite conductivity tensor $\sigma = \begin{bmatrix} \sigma_{xx} & \sigma_{xy} & \sigma_{xz} \\ \sigma_{yx} & \sigma_{yy} & \sigma_{yz} \\ \sigma_{zx} & \sigma_{zy} & \sigma_{zz} \end{bmatrix}$.

The resistivity, $\rho = 1/\sigma = \begin{bmatrix} \rho_{xx} & \rho_{xy} & \rho_{xz} \\ \rho_{yx} & \rho_{yy} & \rho_{yz} \\ \rho_{zx} & \rho_{zy} & \rho_{zz} \end{bmatrix}$, is also assumed to be positive definite

in Ω . Γ is divided into two parts as current application parts and other parts such that

$$\sigma \frac{\partial \varphi}{\partial n} = \begin{cases} J_{app} & \text{on } \Gamma_2 \\ 0 & \text{on } \Gamma_1 \end{cases} \quad (\text{A.1})$$

where J_{app} is the boundary injected current density and φ is the potential field in Ω . 2D illustration of the injected current profile can be visualized as follows:

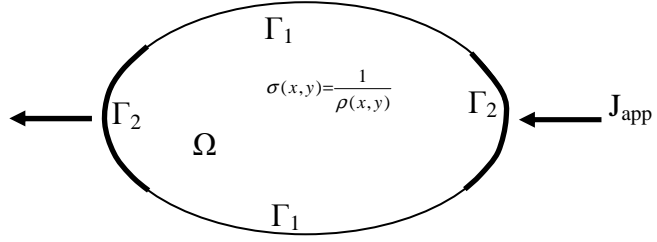


Figure A.1: Illustration of injected current profile for a 2D resistive object.

Since static conditions are assumed;

$$\nabla \times \mathbf{E} = 0 \text{ in } \Omega \quad (\text{A.2})$$

where \mathbf{E} is the electric field in Ω . Since $\mathbf{E} = \rho \mathbf{J}$

$$\nabla \times \rho \mathbf{J} = 0 \quad (\text{A.3})$$

For simplification, let's ρ be a diagonal matrix, that is;

$$\rho = \begin{bmatrix} \rho_{xx} & 0 & 0 \\ 0 & \rho_{yy} & 0 \\ 0 & 0 & \rho_{zz} \end{bmatrix} \quad (\text{A.4})$$

Then,

$$\rho \mathbf{J} = \begin{bmatrix} \rho_{xx} & 0 & 0 \\ 0 & \rho_{yy} & 0 \\ 0 & 0 & \rho_{zz} \end{bmatrix} \cdot \begin{bmatrix} J_x \\ J_y \\ J_z \end{bmatrix} = \begin{bmatrix} \rho_{xx} J_x \\ \rho_{yy} J_y \\ \rho_{zz} J_z \end{bmatrix} \quad (\text{A.5})$$

is obtained. Finally we have,

$$\begin{aligned} \nabla \times \rho \mathbf{J} = \hat{a}_x \left[\frac{\partial}{\partial y} (\rho_{zz} J_z) - \frac{\partial}{\partial z} (\rho_{yy} J_y) \right] + \hat{a}_y \left[\frac{\partial}{\partial z} (\rho_{xx} J_x) - \frac{\partial}{\partial x} (\rho_{zz} J_z) \right] \\ + \hat{a}_z \left[\frac{\partial}{\partial x} (\rho_{yy} J_y) - \frac{\partial}{\partial y} (\rho_{xx} J_x) \right] = 0 \end{aligned} \quad (\text{A.6})$$

Only the z-component of the equation (A.6) can be written as,

$$\left[\left(\frac{\partial}{\partial x} \rho_{yy} \right) \cdot J_y + \left(\frac{\partial}{\partial x} J_y \right) \cdot \rho_{yy} - \left(\frac{\partial}{\partial y} \rho_{xx} \right) \cdot J_x - \left(\frac{\partial}{\partial y} J_x \right) \cdot \rho_{xx} \right] = 0 \quad (\text{A.7})$$

In order to discretize equation (A.7), following discrete model is used in the imaging domain and equation (A.8) is obtained.

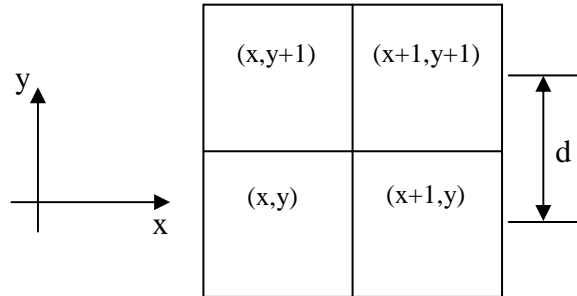


Figure A.2: Discrete illustration of the imaging area.

$$\begin{aligned} & \left[\frac{\rho_{yy}(x+1, y) - \rho_{yy}(x, y)}{d} \right] \cdot J_y(x, y) + \left[\frac{\partial}{\partial x} J_y(x, y) \right] \cdot \rho_{yy}(x, y) \\ & - \left[\frac{\rho_{xx}(x, y+1) - \rho_{xx}(x, y)}{d} \right] \cdot J_x(x, y) - \left[\frac{\partial}{\partial y} J_x(x, y) \right] \cdot \rho_{xx}(x, y) = 0 \end{aligned} \quad (\text{A.8})$$

Finally we have,

$$\begin{aligned} & \rho_{xx}(x, y) \left[J_x(x, y) - \frac{\partial}{\partial y} J_x(x, y) \cdot d \right] - \rho_{yy}(x, y) \left[J_y(x, y) - \frac{\partial}{\partial x} J_y(x, y) \cdot d \right] \\ & - \rho_{xx}(x, y+1) \cdot J_x(x, y) + \rho_{yy}(x+1, y) \cdot J_y(x, y) = 0 \end{aligned} \quad (\text{A.9})$$

As seen, we have an equation which is equal to zero. Therefore, the vector matrix equation obtained from this equation without using any a-priori ρ information will be in the form of

$$A \cdot \rho = 0 \quad (\text{A.10})$$

where A is an $(m \times n \times 2)$ by $(m \times n \times 2)$ coefficient matrix and ρ is an $(m \times n \times 2)$ by 1 resistivity vector which is written as $[\rho_{xx}(1,1) \ \rho_{yy}(1,1) \ \rho_{xx}(1,2) \ \rho_{yy}(1,2) \ \dots \dots \rho_{xx}(m,n) \ \rho_{yy}(m,n)]^T$.

To solve this problem, let's assume that the first row and the last column resistivities of the object seen in Figure A.3 are known. Then, equation (A.9) is rearranged for the second row and the $(n-1)^{\text{th}}$ column resistivities as

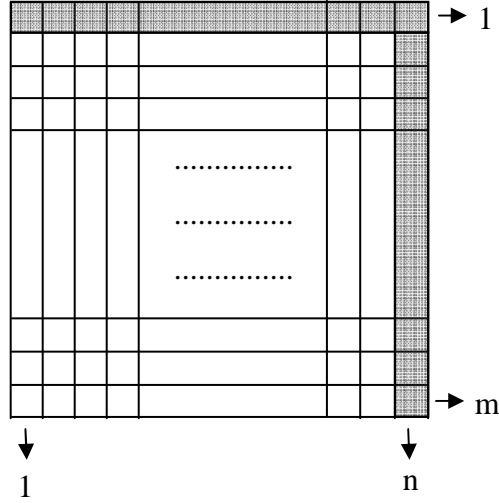


Figure A.3: Discrete illustration of the imaging area in which the first row and the last column resistivities are known

$$\rho_{xx}(x, y) \left[J_x(x, y) - \frac{\partial}{\partial y} J_x(x, y) \cdot d \right] - \rho_{yy}(x, y) \left[J_y(x, y) - \frac{\partial}{\partial x} J_y(x, y) \cdot d \right] + \rho_{yy}(x+1, y) \cdot J_y(x, y) = \rho_{xx}(x, y+1) \cdot J_x(x, y) \quad (\text{A.11})$$

$$\rho_{xx}(x, y) \left[J_x(x, y) - \frac{\partial}{\partial y} J_x(x, y) \cdot d \right] - \rho_{yy}(x, y) \left[J_y(x, y) - \frac{\partial}{\partial x} J_y(x, y) \cdot d \right] - \rho_{xx}(x, y+1) \cdot J_x(x, y) = -\rho_{yy}(x+1, y) \cdot J_y(x, y) \quad (\text{A.12})$$

respectively. Then, we can obtain a vector-matrix equation in the form of

$$A \cdot \rho = b \quad (\text{A.13})$$

in which ρ is written as $[\rho_{xx}(2,1) \ \rho_{yy}(2,1) \ \dots \ \rho_{xx}(2,n-1) \ \rho_{yy}(2,n-1) \ \rho_{xx}(3,n-1) \ \rho_{yy}(3,n-1) \ \dots \ \rho_{xx}(m,n-1) \ \rho_{yy}(m,n-1)]^T$, A is a coefficient matrix and b is nonzero right hand side. SVD based pseudo inverse technique without any truncation is used to calculate the inverse of A for the solution of ρ . A matrix has full column rank, and therefore it is guaranteed that ρ is not in the null space of A . After finding the second row and the $(n-1)^{\text{th}}$ column resistivities, equations (A.1.11) and (A.1.12) are used to obtain third

row and the $(n-2)^{\text{nd}}$ column resistivities and this procedure is continued till reaching to the last row. Since we have 2 unknowns in every equation, we must use at least two different current injection patterns.

Here, it is important to note that, $\left[\frac{\partial}{\partial x} J_y(x, y) \right]$ and $\left[\frac{\partial}{\partial y} J_x(x, y) \right]$ derivative operations can be performed using different methods. In the following parts some of these methods will be implemented and effects on the reconstruction will be evaluated. Following resistivity distribution was used for the simulations.

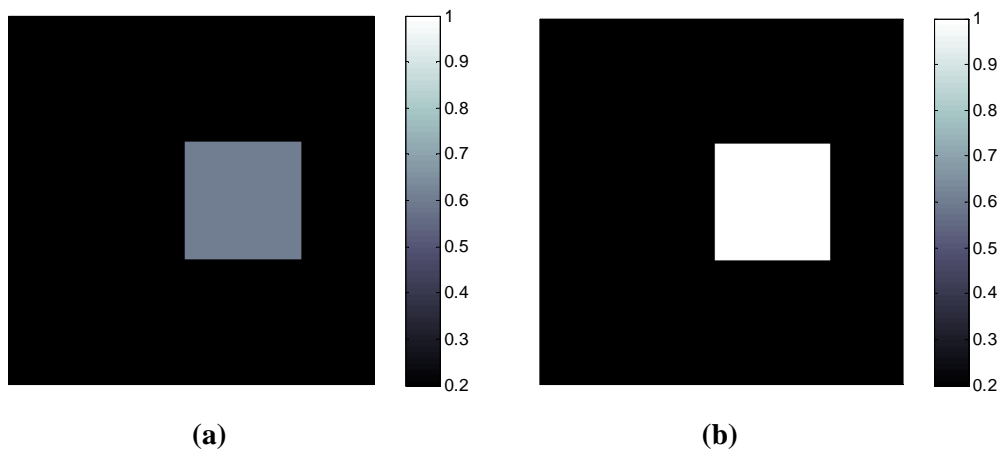


Figure A.4: Conductivity distributions used for simulations: (a) σ_{xx} , (b) σ_{yy} . Values are in S/m.

A.1.1 Derivation Using Sobel Operator

In this case, derivative operations were performed using 3-by-3 Sobel operators given by equations in (A.14).

$$\frac{\partial}{\partial x} J_y(x, y) = \frac{1}{8\Delta x} \begin{vmatrix} 1 & 0 & -1 \\ 2 & 0 & -2 \\ 1 & 0 & -1 \end{vmatrix} ** J_y(x, y)$$

(A.14)

$$\frac{\partial}{\partial y} J_x(x, y) = \frac{1}{8\Delta y} \begin{vmatrix} -1 & -2 & -1 \\ 0 & 0 & 0 \\ 1 & 2 & 1 \end{vmatrix} ** J_x(x, y)$$

For demonstration, y-component of the current density distribution and the x-directed derivative of this distribution using Sobel operator are shown in Figure 3-c and 3-d, respectively. Obtained resistivity images using equations (A.11) and (A.12) are given in Figure A.5a and A.5-b.

As seen from the reconstructed images, reconstruction errors and even negative resistivities start at the borders of the inner object and continue until the boundary of the imaging area because of the recursive behavior of the algorithm. When we investigate the reason of this reconstruction error at the border of the inner object, we see that this error comes from the calculated derivative values. To explain this with more detail, let's first look at the Figures A.5-a and A.5-b. Because of the smoothing effect of the 3-by-3 Sobel operators, we see a 2 point gradient at the right and left borders of the inner object (25. – 26. columns and 40. and 41. columns.) in the x gradient of the J_y image as in Figure 5-d. But J_y image in Figure A.5-c has in fact one point gradients between the 25. and 26. columns and between 40. and 41. columns. Therefore wrong gradient value dominates the coefficient of the ρ_{yy} in equations (A.11) and (A.12) and this causes the error to start at the rapid gradient change. As mentioned earlier, because of the recursive behavior of the algorithm, this error projected until the end of the imaging area. Same explanation is also valid

for ρ_{xx} , but in that case, since y gradients are used, changes in vertical directions are important and error projects in that direction.

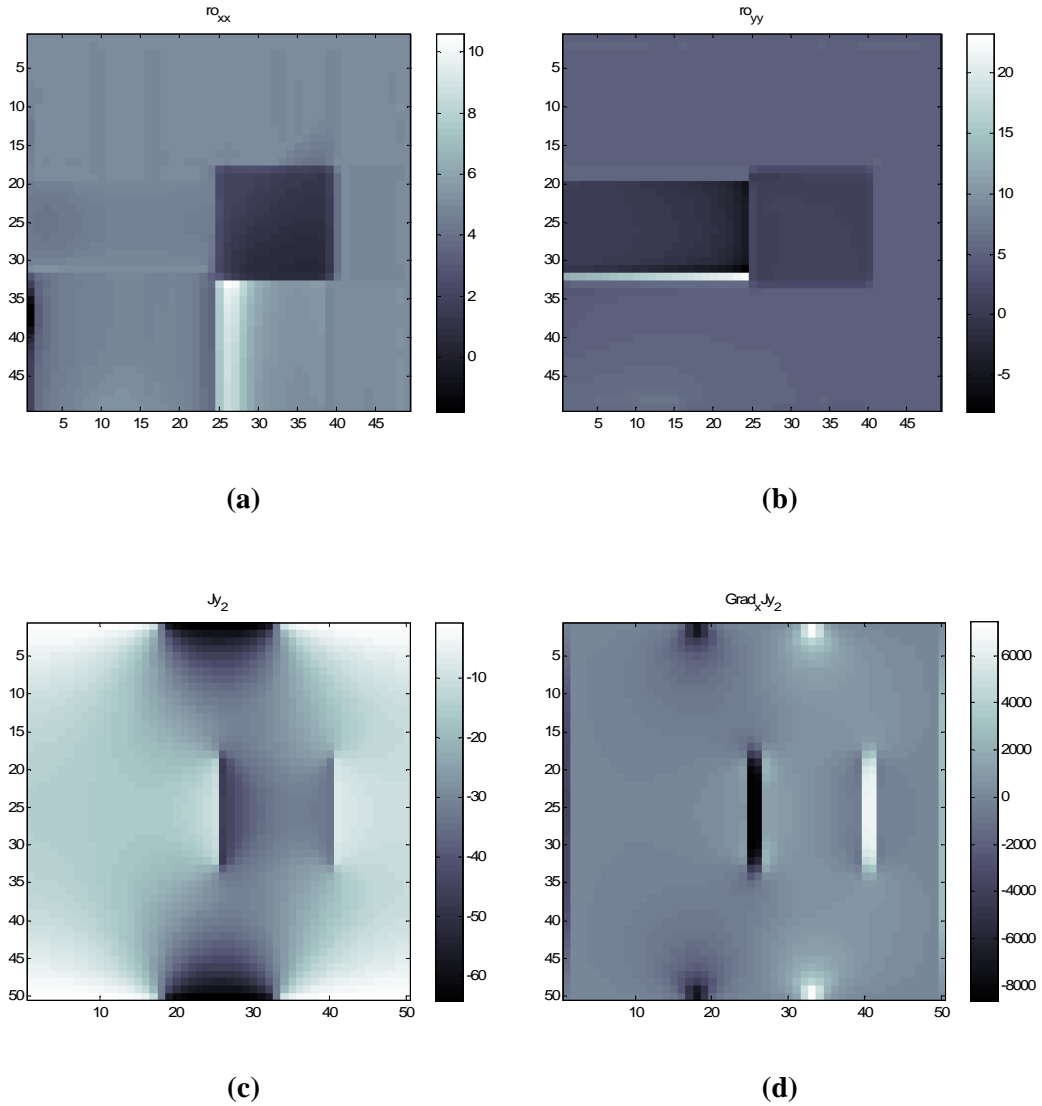


Figure A.5: (a) x component of the reconstructed resistivity image, (b) y component of the reconstructed resistivity image, (c) y component of the current density distribution for one current drive and (d) x directed gradient of the distribution shown in (c).

A.1.2 Derivation Using FFT Algorithm Based Differentiation

For this part, assume that the given complex image has N_x and N_y pixels along the x and y directions with pixel size $\Delta x = 1$ and $\Delta y = 1$, respectively. It is easy to see that

$$\frac{\partial \bar{\varphi}(m,n)}{\partial x} = \sum_{p=N_x/2}^{N_x/2-1} \frac{i2\pi p}{N_x^2} F_x \bar{\varphi}(p,n) e^{i2\pi m p / N_x} \quad (\text{A.15})$$

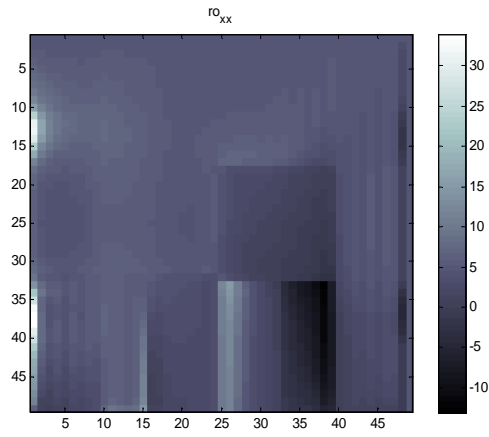
where $F_x \bar{\varphi}(p,n)$ is the discrete Fourier transform of $\bar{\varphi}(m,n)$ along the x direction given by

$$F_x \bar{\varphi}(p,n) = \sum_{m=-N_x/2}^{N_x/2-1} \bar{\varphi}(m,n) e^{-i2\pi m p / N_x} \quad (\text{A.16})$$

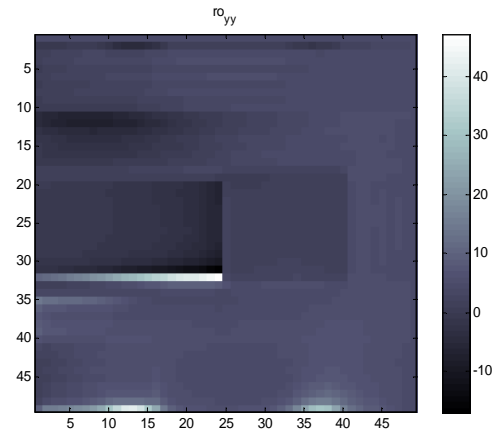
Similarly, $\partial \bar{\varphi}(m,n) / \partial y$ can be evaluated using FFT-based method.

Using this formulation, gradients of current density distribution components were calculated first and resistivity images were then calculated using equations (A.11) and (A.12) and the algorithm just after it. In Figure A.6, y -component of the current density distribution, the x -directed derivative of this distribution and reconstructed resistivity images are shown.

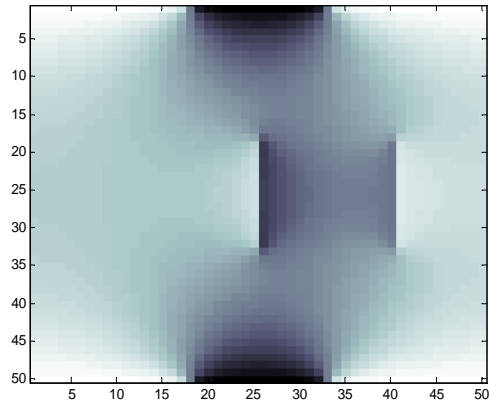
Similar to the previous case, derivative figure has again two point gradient at the object borders. Therefore similar negative resistivity reconstructions are seen in the reconstructed resistivity images.



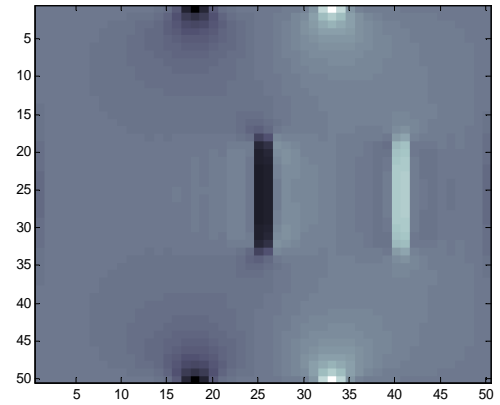
(a)



(b)



(c)



(d)

Figure A.6: (a) x component of the reconstructed resistivity image, (b) y component of the reconstructed resistivity image, (c) y component of the current density distribution for one current drive and (d) x directed gradient of the distribution shown in (c).

A.1.3 Derivation Using Forward Difference Based Differentiation

A forward difference is an expression of the form

$$\Delta_h[f](x) = f(x+h) - f(x) \quad (\text{A.17})$$

The derivative of a function f at a point x is defined by the limit

$$f'(x) = \lim_{h \rightarrow 0} \frac{f(x+h) - f(x)}{h} \quad (\text{A.18})$$

If h has a fixed (nonzero) value, instead of approaching zero, then the right-hand side is

$$\frac{f(x+h) - f(x)}{h} = \frac{\Delta_h[f](x)}{h} \quad (\text{A.19})$$

Using this differentiation formulation, x and y directed gradients were calculated, resistivity images were reconstructed. Y-component of the current density distribution, the x-directed derivative of this distribution and reconstructed resistivity images are shown in Figure A.7.

As seen from the gradient figure in Figure A.7-d, one point gradient is obtained in this case. But since the gradient between $(n+1)^{\text{th}}$ and n^{th} columns are written to the n^{th} column, one pixel shift to the left appears. More clearly, the gradient between 25. and 26. columns (26. column is the left boundary of the inner object) is written to the 25. column. Therefore, this causes again to use wrong gradient value at 25. column and reconstructed conductivity becomes erroneous. The rest also goes erroneous because of the recurrence.

In order to overcome this problem, we thought to remove one column from the middle part of the inner object in the gradient figure and shift the left hand side of that column right. A similar operation is also performed for rows, one row is

removed from the middle part of the inner object and remaining rows under it is shifted up. So, gradients and the object boundaries are coincided. Obtained reconstructed results are shown in Figure A.8.

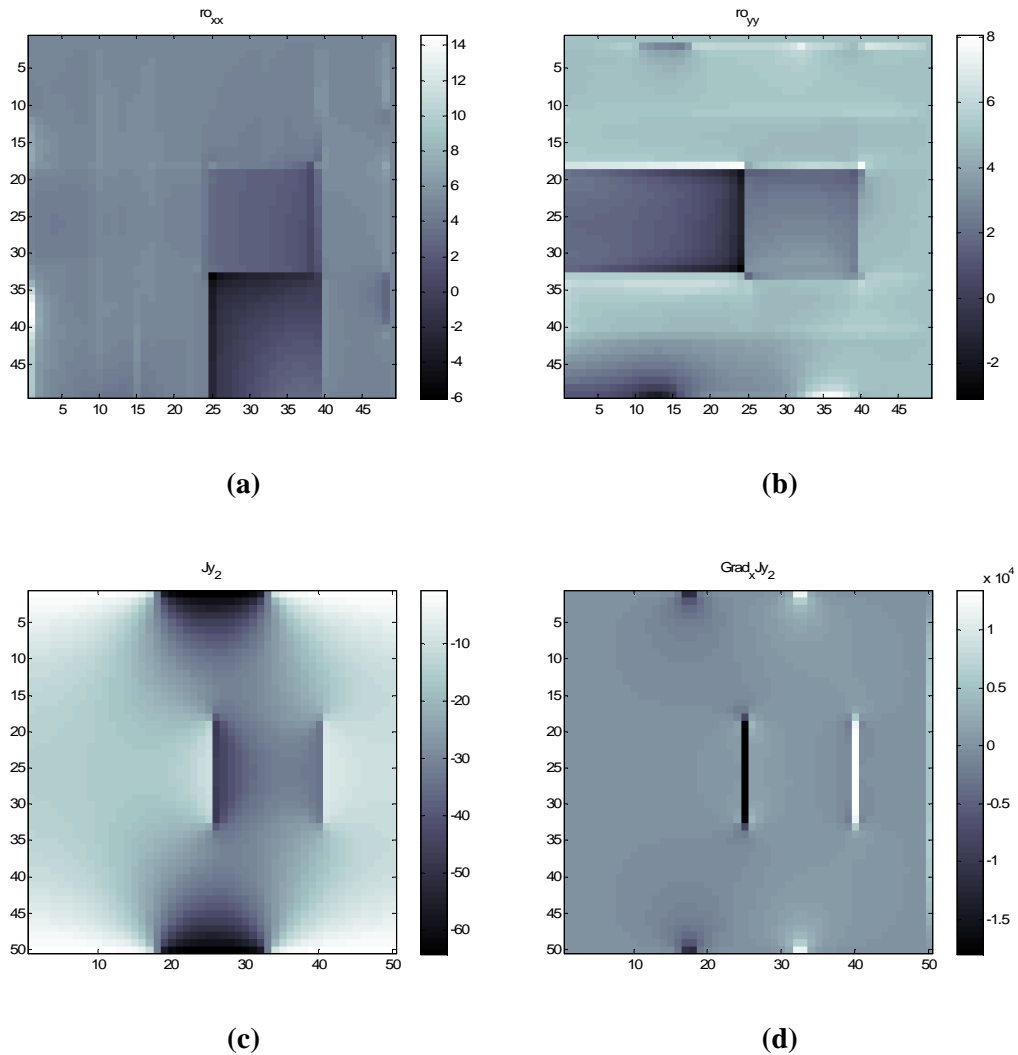


Figure A.7: (a) x component of the reconstructed resistivity image, (b) y component of the reconstructed resistivity image, (c) y component of the current density distribution for one current drive and (d) x directed gradient of the distribution shown in (c).

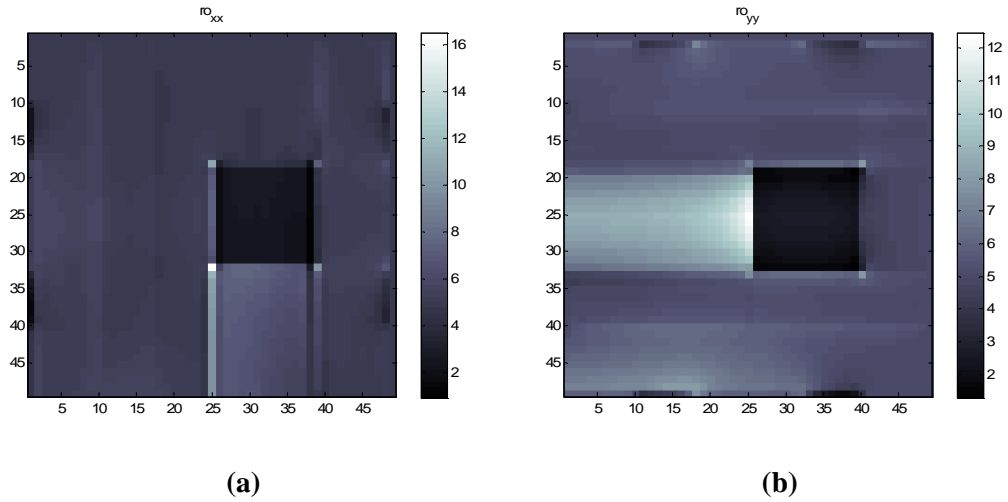


Figure A.8: (a) x component of the reconstructed resistivity image, (b) y component of the reconstructed resistivity image

As seen from the results, negative resistivity values are disappeared. But it is obvious that finding the point where to remove one column is very difficult and even impossible for more complex image distributions. So a more feasible way should be found.

A.1.4 Derivation Using Forward Difference Based Differentiation with Up-sampling

In this part, we calculated the derivatives using forward difference formula as in the previous case. But before this calculation, first we up-sampled current density components by 2 and obtained J 's as shown in the Figure A.9. Then using these values, we calculated derivatives at points where J 's exist. Therefore, we could calculate the derivatives at exact points with current density components. Figure A.10 shows the y-component of the current density distribution, the x-directed derivative of this distribution and reconstructed resistivity images.

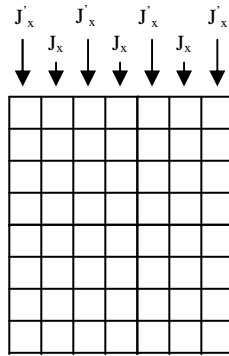


Figure A.9: Illustration of up-sampling. Prime coordinates show the points generated by up-sampling.

As seen from the results, a similar ρ_{yy} image is obtained with Figure A.8-b without removing any column or row. But this is not the case for ρ_{xx} image. This is because, up sampling the current density image by 2 and selecting odd numbered columns and rows for the calculation of gradients and even numbered ones for current density data respond different manner to the even and odd numbered columns and rows. More clearly, if the boundary of an object is on the even numbered column or row, after up sampling and calculation of the gradient, gradient data and the current density data at the boundary of the object coincide. But, if the boundary of an object is on the odd numbered column or row, they do not coincide. In Figure A.10-b, since the left boundary of the object is on the even numbered column, after reconstruction we didn't obtain negative resistivity values at this boundary. But since the bottom boundary is on the odd numbered row, reconstruction becomes poor because of the above reason. Therefore, this method for differentiation is not also a feasible way but among all, we thought that this method is the most feasible one.

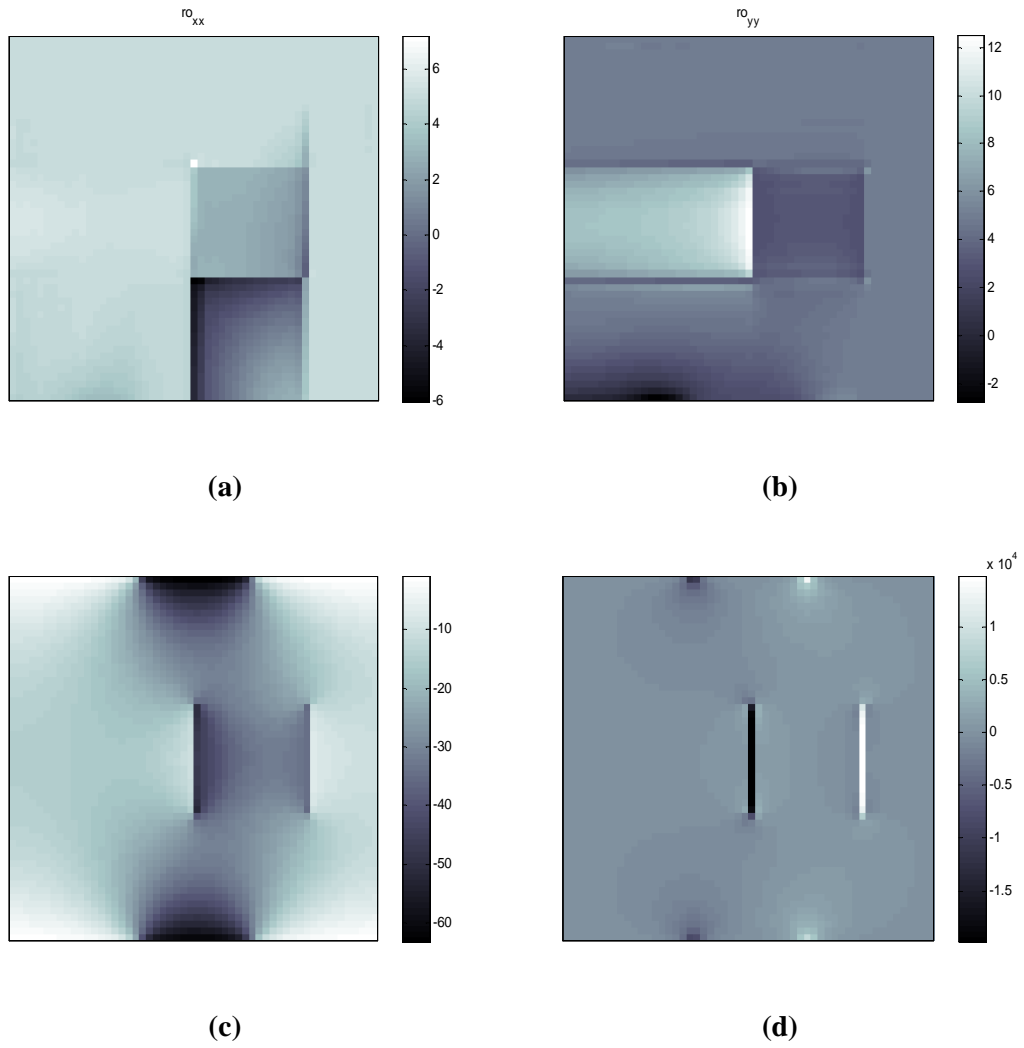


Figure A.10: (a) x component of the reconstructed resistivity image, (b) y component of the reconstructed resistivity image, (c) y component of the current density distribution for one current drive and (d) x directed gradient of the distribution shown in (c).

After explaining all these methods, it is tried to reconstruct more complex and round shaped objects with taking the derivative using the method explained in A.1.4. Model figure used for reconstruction is shown in Figure A.11. Obtained reconstruction results are in Figure A.12.

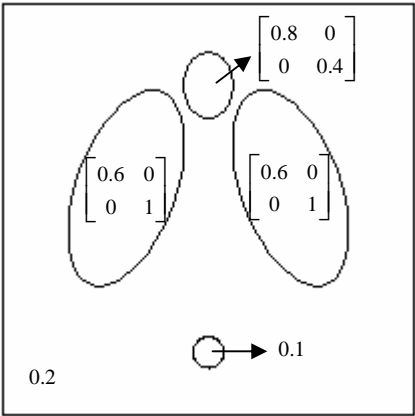


Figure A.11: Model figure used for reconstruction. The values on the figure indicate conductivity values in S/m.

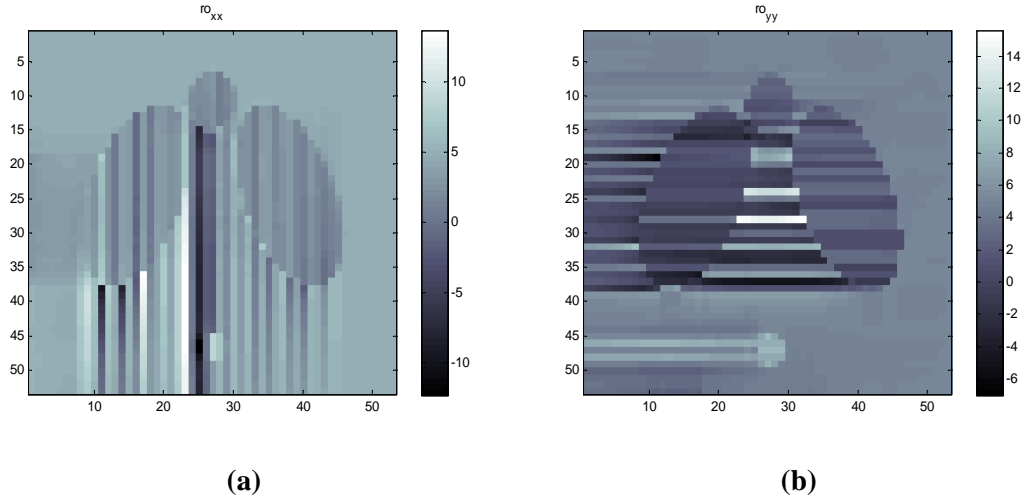


Figure A.12: Obtained reconstruction results for the distribution shown in Figure A.11. (a) x component of resistivity, (b) y component of resistivity.

As seen from the results in Figure A.12, reconstructed images have sharp lines starting from the object boundaries. The final evaluation on this topic is to use a low pass filter to the reconstructed images and trying to remove the sharp lines. For this purpose, following filter is designed for ρ_{yy} image since sharp edges are mainly in y direction.

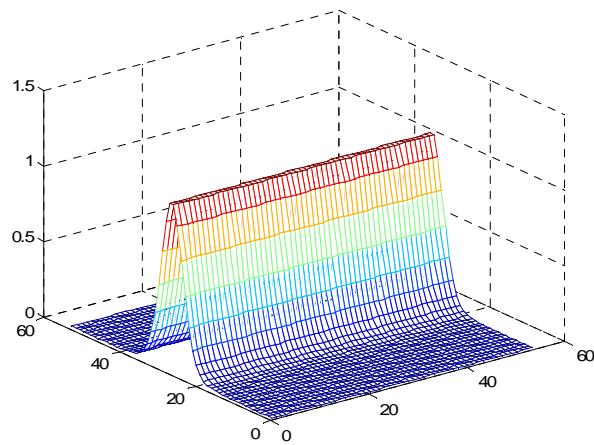


Figure A.13: Designed low pass filter.

This filter is applied to the Fourier Transform of the ρ_{yy} image which can be seen in Figure A.14.

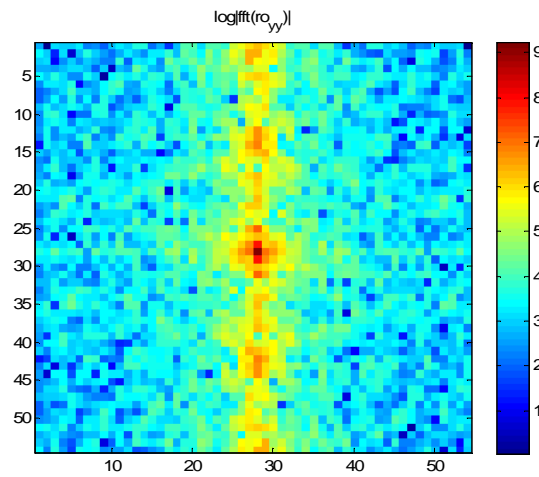


Figure A.14: Fourier Transform of the image in Figure A.12-b.

Then the inverse Fourier transform operation is applied to the filtered FFT image and the following figure is obtained.

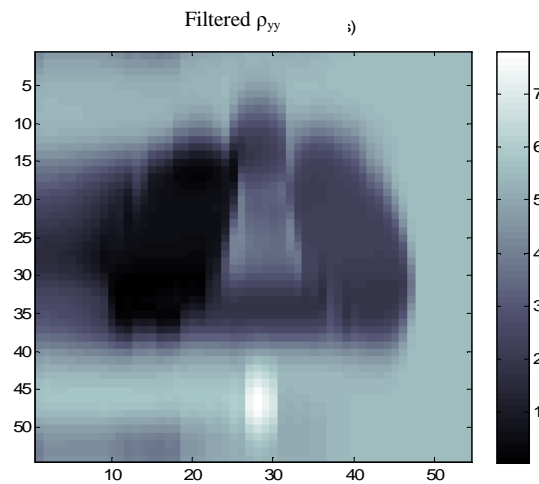


Figure A.15: Low pass filtered ρ_{yy} image in Figure A.12-b.

As seen from the figure, sharp lines in Figure A.12-b are weakened but the image is blurred as expected. At this point, it is thought that, all possible studies on this work are completed and it is decided to stop working on this algorithm.

VITA

CIRRUCULUM VITAE

PERSONAL INFORMATION

Surname, Name : Değirmenci, Evren
Nationality : Turkish (T.C.)
Date and Place of Birth : 12 September 1980, Antalya
Marital Status : Single
Phone : 0 532 7942218
e-mail : evren@eee.metu.edu.tr

EDUCATION

Degree	Institution	Year of Graduation
Ph.D. on B.Sc.	METU	2010
B.Sc.	Gazi University	2002
High School	Antalya High School, Antalya	1997

WORK EXPERIENCE

Year	Place	Enrollment
2004-Present	METU Dept. of EE Eng.	Research Assistant

FOREIGN LANGUAGES

Advanced English, Basic German

PUBLICATIONS DURING Ph.D. STUDY

International Peer-Reviewed Journal Papers

E. Değirmenci, B.M. Eyüboğlu, "Anisotropic conductivity imaging with MREIT using equipotential projection algorithm", *Physics in Medicine and Biology*, Vol.52, No.24, pp.7229-7242, 2007.

International Conference Papers

E. Değirmenci, B.M. Eyüboğlu, "Anisotropic Conductivity Imaging with MREIT Using J-substitution and Hybrid J-substitution Algorithms", *World Congress on Medical Physics and Biomedical Engineering, Munich – Germany, IFMBE Proceedings vol.25/II*, p. 315 ff., DVD-ROM Springer-Verlag ISBN 978-3-642-03897-6, 2009.

E. Değirmenci, B.M. Eyüboğlu, "Magnetic resonance electrical impedance tomography for anisotropic conductivity imaging", *4th European Conference of the International Federation for Medical and Biological Engineering, Antwerp, Belgium, CD-ROM, Vol.22, Springer*, pp.728-31, 2008.

B.M. Eyüboğlu, **E. Değirmenci**, "Equipotential projection based MREIT reconstruction without potential measurements", *Proc. of 13th Conference on Electrical Bioimpedance and 8th Conference on Electrical Impedance Tomography, Graz – Austria, IFMBE Proceedings vol. 17, DVD-ROM Springer-Verlag ISBN 3-540-73840-4*, pp.516-9, 2007.

E. Değirmenci, B.M. Eyüboğlu, "Anisotropic conductivity imaging with MREIT using equipotential projection algorithm," *Proc. of 13th Conference on Electrical Bioimpedance and 8th Conference on Electrical Impedance Tomography, Graz – Austria, IFMBE Proceedings vol. 17, DVD-ROM Springer-Verlag ISBN 3-540-73840-4*, pp.496-9, 2007.

E. Değirmenci and B. M. Eyübođlu, "Performance analysis of two magnetic resonance - electrical impedance tomography (MR-EIT) reconstruction algorithms to image anisotropic conductivity," 11th. International Biomedical Science and Technology Days, Ankara - Turkey, p.23, 2004.

National Conference Papers

E. Değirmenci, B.M. Eyübođlu, "MREIT tekniđinde J-yerine koyma algoritması kullanarak yön bađımlı iletkenlik görüntülemesi", 14. Biyomedikal Mühendisliđi Ulusal Toplantısı, İzmir, CD-ROM, 3B2, 4pages, 2009.

E. Değirmenci, B.M. Eyübođlu, "Manyetik rezonans elektriksel empedans tomografisinde eşgerilim yansıtması algoritması ile yön bađımlı iletkenlik görüntüleme", 13. Biyomedikal Mühendisliđi Ulusal Toplantısı, Ankara, CD-ROM, 2008.

E. Değirmenci, B.M. Eyübođlu, "Biyolojik dokuların elektriksel iletkenliđindeki yön bađımlılıđın MREIT gericiatımında önemi ve görüntülenmesi", 3. Türk Manyetik Rezonans Derneđi Kongresi Bildiri Kitabı, Ankara -TR, pp.31, 2008.

E. Değirmenci and B. M. Eyübođlu, "Manyetik rezonans – elektriksel empedans tomografisi ile yön bađımlı iletkenlik görüntülenebilmesi için geliştirilmiş eşpotansiyel yansıtması tabanlı özgün bir görüntüleme tekniđi", Proc. of URSI-TÜRKiYE 2006 3rd National Congress, Ankara - TR, pp.219-21, 2006.

E. Değirmenci and B. M. Eyübođlu, "MR-EIT İcin Geliştirilen Görüntüleme Algoritmasının Performansının Yön Bađımlı İletkenlik Durumu İcin İncelenmesi", Proceedings of URSI-TÜRKiYE'2004 2nd National Congress, Ankara - Turkey, pp.230-2, 2004.